

FLORIDA STATE UNIVERSITY
COLLEGE OF ARTS AND SCIENCES

CLIMATE FEEDBACK ANALYSIS OF THE GFDL IPCC AR4 GLOBAL WARMING
SIMULATION

By
CHRISTELLE CASTET

A Dissertation submitted to the
Department of Meteorology
in partial fulfillment of the
requirements for the degree of
Doctor of Philosophy

Degree Awarded:
Fall Semester, 2009

The members of the committee approve the dissertation of Christelle Castet on July 23rd 2009.

Ming Cai
Professor Directing Dissertation

William Dewar
Outside Committee Member

Xiaolei Zou
Committee Member

Paul Ruscher
Committee Member

Mark Bourassa
Committee Member

Approved:

Robert Ellingson, Chair, Department of Meteorology

Joseph Travis, Dean, College of Arts and Sciences

The Graduate School has verified and approved the above named committee members.

ACKNOWLEDGEMENTS

I would like to express my deep appreciation to my major professor Dr Cai, who made this work possible and gave me endless support, drive, and guidance throughout my research. I am thankful to my committee members, Dr Dewar, Dr Ruscher, Dr Bourassa, and Dr Zou, for the time and feedbacks they offered.

I am grateful to my Florida support network starting with my French connection Morgan and Sophie, my roommate Tzvetalina, with whom I've shared the ups and downs of grad school, and lots of activities and adventures, and Parisa for always being there for me. I acknowledge everyone in my lab, past and present, Dr Lim, Chul Su, and especially Dr Lu for his valuable and courteous assistance with my research and for sharing his knowledge on climate feedbacks. I would also like to give a special thank you to my fellow meteorologists, Gauher for being a wise friend and great listener since the beginning of our studies, Scott and Amin and countless others for providing great company, discussion, and fun in the department.

I most importantly want to express all my gratitude to my parents for their precious encouragements and continuous support throughout the years. I especially thank my sister Carine for always being there for me, distracting me and also pushing me in the right direction when I needed it. I dedicate my work to them.

TABLE OF CONTENTS

List of Tables	vi
List of Figures	vii
Abstract.....	xi
CHAPTER 1 INTRODUCTION	1
1.1 Objectives	7
1.2 Approach.....	7
1.3 Organization of the Dissertation	9
CHAPTER 2 BACKGROUND ON CLIMATE FEEDBACKS	10
2.1 Concept of Sensitivity, Forcing, Feedback, and, Uncertainty	10
2.2 Methods to Study Climate Forcing and Feedbacks	15
2.2.1 Methods Based on energy balance at the TOA.....	17
2.2.2 Climate Feedback-Response Analysis Method (CFRAM).....	20
2.2.3 Special Cases PRP Versus CFRAM at the TOA	22
2.3 Major Findings on Climate Forcing and Feedbacks	24
CHAPTER 3 DATA	30
CHAPTER 4 METHODOLOGY	32
4.1 Radiation Transfer Model.....	32
4.2 Implementation of CFRAM.....	35
4.3 Method Validation	41
CHAPTER 5 EVALUATION OF MODEL CLIMATOLOGY	48
5.1 Global energy and water mass balance	49
5.2 Solar and infrared radiations.....	50
5.3 Surface turbulent heat fluxes	51
5.4 Temperature	52
5.5 Tropospheric Specific Humidity.....	56
CHAPTER 6 ENERGY FLUX PERTURBATIONS AT THE TOP OF THE ATMOSPHERE.....	59
6.1 Radiative forcing due to the doubling of CO ₂	59
6.2 Water vapor feedback	63
6.3 Surface albedo feedback	66
6.4 Inferred change in cloud forcing and dynamics.....	67
6.5 Discussion	76

CHAPTER 7 RESULTS OF CFRAM ANALYSIS ON THE GFDL_CM2.0 GLOBAL WARMING SIMULATION.....	78
7.1 External radiative forcing and its induced temperature changes	79
7.2 Water vapor feedback and its induced temperature changes	83
7.3 Surface albedo feedback and its induced temperature changes	87
7.4 Surface turbulent heat flux feedback and its induced temperature change.....	91
7.5 Change in cloud forcing at surface and its induced temperature changes	95
7.6 Sum of cloud forcing change and large scale dynamics, and associated temperature change	99
7.7 Discussion	103
CHAPTER 8 CONCLUSIONS	109
APPENDIX A GFDM_CM2.0 MODEL CHARACTERISTICS	113
APPENDIX B DATA MANIPULATION AND QUALITY CONTROL	115
REFERENCES	117
BIOGRAPHICAL SKETCH	125

LIST OF TABLES

Table 3.1: GFDL_CM2.0 model characteristics.....	31
Table 4.1: Globally averaged longwave (LW) and shortwave (SW) radiation flux at the surface and the TOA (unit: W m ²).....	33
Table 6.1: Average of the external forcing and each feedback as view from the TOA over high latitudes (± 90 ; ± 60) and low latitudes (-60;60). (Units W m ⁻²).	77
Table 7.1: Globally averaged partial temperature changes at the surface (units: Kelvin).	104

LIST OF FIGURES

Figure 1.1: Global mean surface temperature anomalies relative to the 1901-1950 average, every 10 years from 1096 to 2005. Observations (black curve), and approximate ranges covering the middle 90% of simulations of the climate of the 20 th century (pink and blue band). (Hegerl et. al 2007).....	3
Figure 1.2: Zonal means of changes in atmospheric (top) and oceanic (bottom) temperatures (°C). Multi-model mean during three time periods (a-c). Meehl, et al 2007.....	4
Figure 1.3: Same as Figure 1.2 but for surface temperature change projections. Meehl, et al 2007.....	4
Figure 1.4: Zonal and time average of the surface warming from 10 IPCC AR4 climate models, 2 × CO ₂ minus control slab ocean climate simulations (units: Kelvin).....	6
Figure 1.5: Zonal and time mean of: a) the atmospheric and b) the surface warming from the GFDL_CM2.0 climate model, 2 × CO ₂ minus control slab ocean climate simulations (units: Kelvin).....	8
Figure 2.1: Diagram showing the relation between climate forcing, feedback and response.....	12
Figure 2.2: Feedback parameters comparison (WV-water vapor, C-cloud, A-albedo, LR-lapse rate) in different studies by Colman (2003), Soden and Held (2006), Winton (2006).....	14
Figure 2.3: Globally averaged energy budget. Units are W m ⁻²	16
Figure 2.4: Strength of radiative forcing from human activity and natural processes in 2005 relative to year 1750. (Forster et al, 2007).....	25
Figure 4.1: Diagram of the radiative energy flux convergence between levels l and l+1 and at the surface.	35
Figure 4.2: Example of the Planck feedback matrix. Each column represents the cooling rate change from the top layer to the surface layer due to a 1 K temperature increase from the equilibrium temperature profile.	40
Figure 4.3: Change in cloud forcing at the surface, a) LHS of (4. 21) or RHS of (4.22), b) RHS of (4. 21) (unit W m ⁻²).....	44

Figure 4.4: Change in cloud forcing at the surface using GFDL_CM2.0 clear sky surface radiation data for the terms in RHS of (4. 21) (unit W m^{-2})	45
Figure 4.5: $\Delta(\text{S-R})$ color shadings and sum of the RHS of (4. 23) contours. a) Zonal and time mean in the atmosphere, and b) time mean at the surface. (Units: W m^{-2}).....	47
Figure 5.1: Time mean of the surface temperature difference between GFDL_CM2.0 model and NCEP-NCAR reanalysis (degree C). Zero degree line for NCEP-NCAR (blue) and GFDL_CM2.0 (red).....	54
Figure 5.2: Modeled (red) and observed (blue) zonal and time mean of the atmospheric temperature (degree Celsius)	56
Figure 5.3: Modeled (red) and observed (blue) zonal and time mean of the atmospheric specific humidity. (Units g kg^{-1})	58
Figure 6.1: Time average of the external radiative forcing calculated at the TOA (unit: W m^{-2}).	62
Figure 6.2: Vertically integrated specific humidity in the control simulation (color shadings), and its change in $2 \times \text{CO}_2$ simulation (contours) (unit: g/kg).....	62
Figure 6.3: Time average of the water vapor feedback calculated at the TOA (unit: W m^{-2}).	65
Figure 6.4: Time mean of the surface temperature in the control simulation (units: Kelvin).	65
Figure 6.5: Time average of the surface albedo feedback calculated at the TOA (unit: W m^{-2}).	67
Figure 6.6: Time average of the sum of the changes in cloud forcing at TOA and in column integrated convergence of atmospheric energy transport inferred from the change of the net clear-sky radiation fluxes at the TOA (unit: W m^{-2}).	69
Figure 6.7: Total heat transport (contours) and change in total heat transport (color shadings) inferred from the net total sky radiation fluxes at the TOA (unit W m^{-2}). 71	71
Figure 6.8: Change in cloud forcing inferred from the difference between Figure 6.6 and 6.7 (unit W m^{-2}).	74
Figure 6.9: a) Cloud area fraction in the entire atmospheric column as seen from the TOA (%), and b) amount of atmospheric cloud condensed water (in both liquid and ice phases) (g m^{-2}). Control climate (color shadings), and change in the $2 \times \text{CO}_2$ climate simulation (contours).	75

Figure 7.1: Radiative energy flux perturbation (unit: W m^{-2}), and associated partial temperature change (unit: K) due to external forcing: zonal and time mean of the vertical profile a) and b), and time mean at the surface c) and d).....	82
Figure 7.2: Radiative energy flux perturbation (unit: W m^{-2}), and associated partial temperature change (unit: K) due to the water vapor feedback: zonal and time mean of the vertical profile a) and b), and time mean at the surface c) and d).	86
Figure 7.3: Zonal mean of the vertical profile of specific humidity (color shadings), and change in specific humidity in the $2 \times \text{CO}_2$ climate simulation (contours), (unit: kg/kg).	87
Figure 7.4: Radiative energy flux perturbation (unit: W m^{-2}), and associated partial temperature change (unit: K) due to the surface albedo feedback: zonal and time mean of the vertical profile a) and b), and time mean at the surface c) and d).....	90
Figure 7.5: Surface albedo (contours), and change in surface albedo in the $2 \times \text{CO}_2$ climate simulation (color shadings).	91
Figure 7.6: (a, c, e) Energy flux perturbations (units W m^{-2}), and (b, d, f) temperature changes (units: Kelvin) at the surface due to surface heat fluxes. Sensible heat flux SH (a-b), latent heat LH (c-d), and sum of both SH+LH (e-f).	94
Figure 7.7: (a, c, e) Energy flux perturbation (unit: W m^{-2}), and (b, d, f) temperature change (unit: K) at the surface due to the change in surface CRF (a-b), errors in radiation calculations (c-d), and errors due to missing terms (e-f).	98
Figure 7.8: Zonal and time mean of energy flux perturbation (a) (unit: W m^{-2}), and associated temperature change (b) (unit: K) due to the sum of the changes in cloud forcing and large-scale dynamics at the surface and atmospheric column. Time mean of the surface temperature change due to the sum of the changes in cloud forcing and large-scale dynamics in the atmosphere only.....	102
Figure 7.9: Zonal and time mean of the total temperature change from the GFDL_CM2.0 model simulation, and the sum of the partial temperature changes: a) in the atmospheric column and b) at the surface. Color shadings and black line represent the GFDL_CM2.0 temperature change, black contours and red dotted line represent the sum of the partial temperature changes (units: Kelvin).	106
Figure 7.10: Zonal and time mean in the atmospheric column (a-b) and at the surface (c-d). Left panels: sum of the partial temperature changes due to clear-sky radiative flux perturbations (radiative forcing, water vapor feedback, surface albedo feedback). Right panels: partial temperature change due to the sum of dynamical energy perturbations (surface turbulent heat flux feedback, large scale dynamics and	

convection), and change in CRF in the atmospheric column and at the surface (units: Kelvin). 107

Figure 7. 11: Zonal and time mean of the surface partial temperature changes due to a) radiative forcing, b-d) water vapor , surface albedo, and surface turbulent heat flux feedback, and e) sum of the large scale dynamics, convection and change in CRF. f) sum of (a-e) (red dash line), and GFDL_CM2.0 temperature change (black line). (Units: Kelvin). 108

ABSTRACT

Both observed and modeled global warming pattern shows a large surface polar warming and a large upper atmospheric warming in the tropics. This pattern leads to an amplification (reduction) of the temperature gradient at upper levels (surface). Physical processes behind this temperature change are the external radiative forcing, and subsequent feedback processes that may amplify or dampen the climate response. This unique warming pattern suggests that high latitudes are very sensitive to climate change and also the area where the largest warming projection uncertainties occur. The objective of this study is to apply a new coupled atmosphere-surface climate feedback-response analysis method to quantify the contributions of the external forcing alone (doubling of carbon dioxide), and subsequent feedback processes to the 3-D global warming pattern in the GFDL_CM2.0 model. The feedbacks under consideration include the water vapor feedback, surface albedo feedback, surface turbulent heat flux feedback, and the sum of the change in cloud radiative forcing (CRF), vertical convective, and large-scale scale dynamical feedback. The partial temperature changes due to the external forcing and due to individual feedbacks are additive and their sum converges toward the temperature change produced by the original GFDL_CM2.0 global warming simulations. Therefore, our attributions of the global warming pattern to individual thermodynamic and dynamical processes are mathematically robust and physically meaningful.

The partial temperature change due to the water vapor feedback is found to be the largest contributor to the globally averaged surface warming. It is twice as large as the warming due to the external radiative forcing alone. The surface albedo feedback and change in surface cloud radiative forcing increase the surface temperature by a smaller amount. In addition, the changes in atmospheric cloud forcing and large-scale dynamics, as well as the surface turbulent heat flux feedback, contribute to an overall damping the surface warming.

In terms of spatial pattern of global warming, the external forcing alone would cause a large surface warming in the extratropics. The water vapor feedback strengthens the tropical warming substantially and the ice/snow albedo feedback contributes to polar

warming amplification. The atmospheric dynamical feedbacks associated with the enhancement of vertical convection in the tropics acts to amplify the warming in the upper troposphere at the expense of reducing the warming in the lower troposphere and at the surface in the tropics. The dynamical feedbacks due to the strengthening of the poleward energy transport contribute to a warming in the entire troposphere and the surface in high latitudes. At the surface and in the lower troposphere, the additional warming brought by the change in circulations strengthens the warming due to thermodynamical forcings (e.g., external forcing, water vapor feedback, and ice albedo feedback). In the upper troposphere, the warming brought by the change in circulations dominates the cooling due to thermodynamical forcings. As a result, the entire troposphere becomes warmer. The stratospheric cooling is entirely due to the external radiative forcing.

CHAPTER 1

INTRODUCTION

Climate change has been observed over the past century, and temperature changes are an obvious metric that we can relate it to. Surface temperatures averaged globally over the time period from 1901 to 1997 have warmed by 0.62°C (Jones et al., 1999). It is also reported that the global mean surface temperature has increased since the beginning of the 20th century by 0.78°C (National Research Council (NRC), 2008). Between 1979 and 1998, it is estimated that on average, over the globe, surface temperature has increased by 0.25 to 0.4 °C (NRC, 2000). The rate of annual warming for global land areas over the 1901-2000 time period is estimated to be 0.07°C per decade (Jones and Moberg, 2003) or 0.2°C/decade past 30 years (Hansen, 2006). The surface warming pattern displays some apparent regional characteristics. The high latitude temperature increases at a faster rate than the rest of the Earth (Moritz, et al., 2002; Comiso and Parkinson, 2004; Trenberth, 2007). Furthermore, a larger warming is observed over land than ocean (Hansen et al., 2006; Jones and Moberg, 2003; Karl et al., 2006). Warming trends also show seasonal contrasts with a more pronounced increase in temperature during winter and spring over Polar Regions (Johannessen et al., 2004; Rigor et al., 2000; Chapman and Walsh, 1993). In addition, temperature amplification is found over the Arctic in the atmosphere well above the surface throughout the year (Graversen et al., 2008), and in the tropical upper troposphere (Allen and Sherwood, 2008). Understanding the processes responsible for the current warming pattern is of prime importance, as very vulnerable areas such as the Arctic and other regions of the Earth cryosphere are largely affected (Lemke et al., 2007), which has strong consequences on ecosystems and biodiversity (Hare, 2003). It was also documented by Serreze et al. (2000) that changes such as plant growth, increase in precipitation, and decrease in sea-ice extent were taking place over the northern high latitudes. Other observed changes related to the increase in surface air temperature have been put into light, for example a 7% increase in river

discharge to the Arctic Ocean from 1936 to 1999 (Peterson et al., 2002). The International Polar Year (2007-2008) provided a wide-range of findings described in State of Polar Research, and determined that the minimum extent of Arctic perennial sea ice decreased by approximately one million km² during summer between 2007 and 2008 (Allison et al., 2009). A continuation of the current warming trend will have global implications for society (e.g. water availability, hydropower, marine transportation, infrastructures, indigenous communities migration, health risks), biodiversity (e.g. shrinking habitat and migration changes for local animal species), and vegetation zones (e.g. growth season, and agriculture) (Hassol, 2004; NRC, 2008).

The most comprehensive tools for simulating and analyzing the horizontal and vertical structure of climate change are fully coupled atmosphere-ocean general circulation models (AOGCMs). The Fourth Assessment Report of the Intergovernmental Panel on Climate Change (IPCC AR4) highlighted the advances made by climate modeling teams over recent years, particularly the progress made by improving the parameterization of physical processes (e.g. in clouds, the cryosphere, or carbon cycle), and incorporating processes in the modeling of sea ice, land surface, boundary layer or aerosols (Randall et al., 2007). Most AOGCMs for the IPCC AR4 report do not include flux adjustments, which were previously used in the IPCC Third Assessment Report to reduce climate drift. Modeled warming is comparable to observations (Hansen et al., 2006) when the radiative effects of increasing concentrations of greenhouse gases (GHGs) are included (Hegerl et al., 2007). Figure 1.1 represents temperature observations (from HadCUT3, black line), and the simulated 20th century climate from current state of the art AOGCMs used in the IPCC AR4 report (pink and blue bands). The pink band encompasses simulations that include anthropogenic forcings (e.g., increase in GHGs concentration, such as carbon dioxide, methane, nitrous oxide; see chapter 2.1 for details) and variations in solar and volcanic activity. The temperature change of these simulations is in better agreement with observations than the simulations including natural forcings only (blue curve). Over the Arctic, the observed warming amplification is reproduced as well when anthropogenic GHGs forcings are included in the climate simulation (Johannessen et al., 2004; Serreze and Francis, 2006).

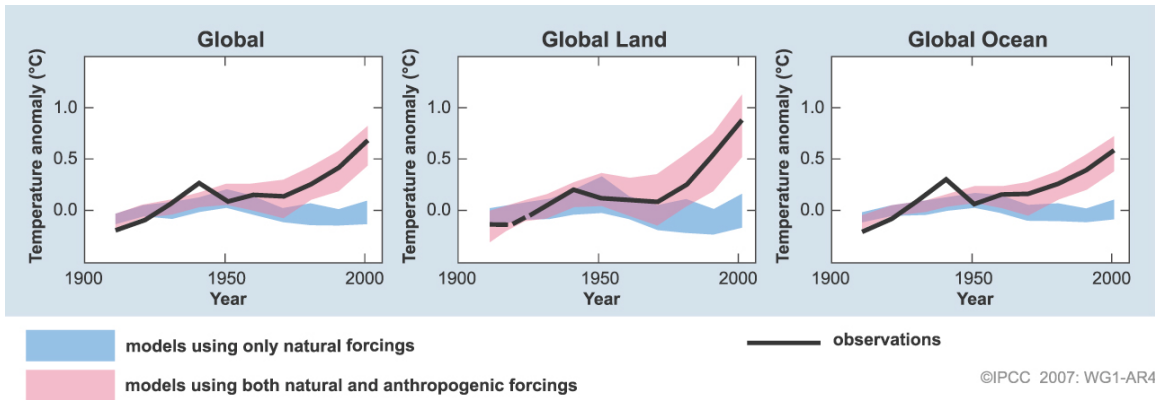


Figure 1.1: Global mean surface temperature anomalies relative to the 1901-1950 average, every 10 years from 1096 to 2005. Observations (black curve), and approximate ranges covering the middle 90% of simulations of the climate of the 20th century (pink and blue band). (Hegerl et. al 2007).

Overall, the observed features of the warming patterns are reproduced with a good degree of accuracy by AOGCMs, and therefore they can be used as a reliable tool to project the future climate (Randall et al., 2007). The IPCC AR4 report reveals the vertical and surface warming projections from a multi-model mean of 12 AOGCMs for three 21st century time periods (Figure 1.2 and 1.3 respectively). The vertical-latitude warming pattern is obtained by averaging along latitudes, and is represented over the ocean depth and the atmospheric column. Focusing on the atmospheric climate projections, we see a familiar temperature change pattern as in observations, namely a warming in the troposphere, a cooling in the stratosphere, an upper-troposphere warming maximum in the tropics, and a larger high latitude warming at the lowest atmospheric levels. This pattern remains largely unchanged in the climate change projections for the three 30-year periods in the next 100 years and intensifies with time. In Figure 1.3, the surface warming is seen to be larger over high latitudes, especially over the Northern Hemisphere. The land areas display an overall greater warming than their surrounding oceans.

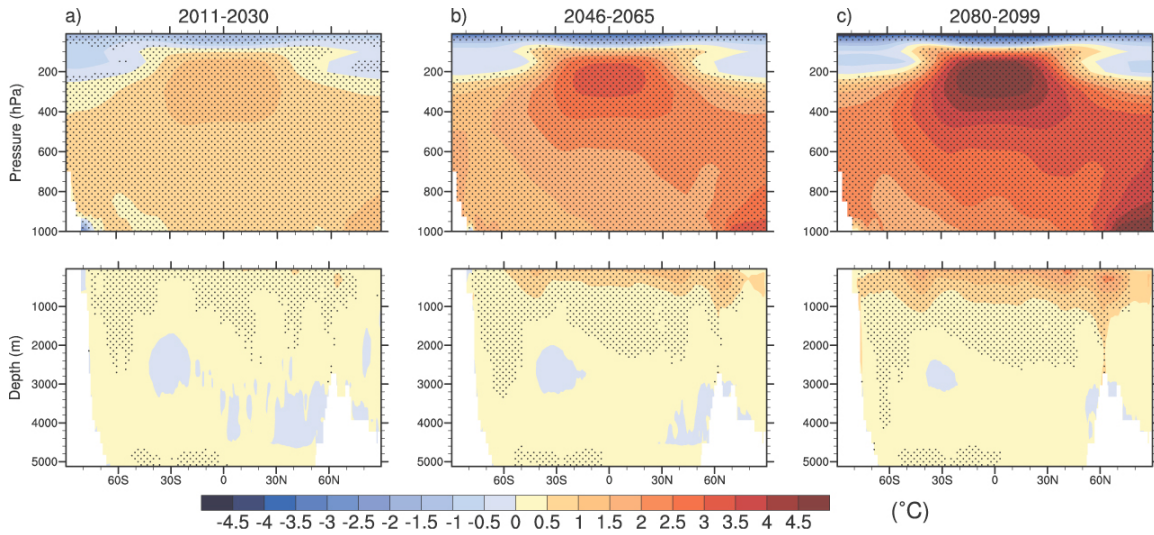


Figure 1.2: Zonal means of changes in atmospheric (top) and oceanic (bottom) temperatures ($^{\circ}\text{C}$). Multi-model mean during three time periods (a-c). (Meehl et al., 2007).

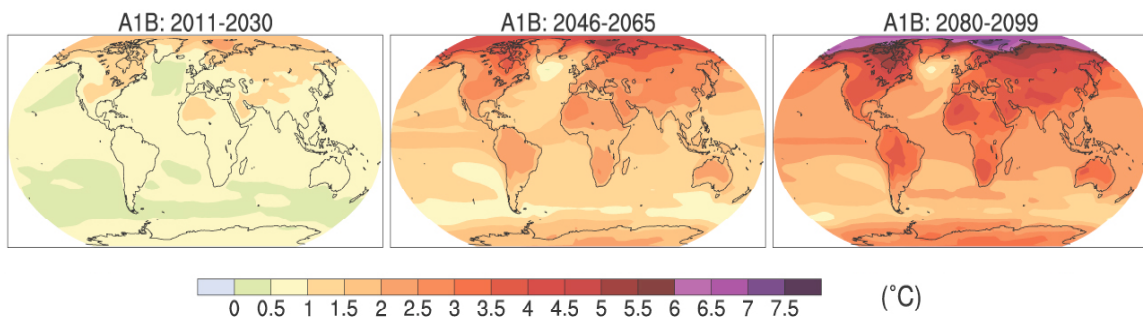


Figure 1.3: Same as Figure 1.2 but for surface temperature change projections. (Meehl et al., 2007).

Global warming estimates shown in Figure 1.2 and 1.3 depend on the radiative forcing scenario used to simulate the climate, and subsequent feedback processes that may amplify or dampen the climate response. Climate forcings produce an initial change in the earth energy balance, which generates a climate response. This in turn induces feedbacks (as discussed in section 2.1). Both forcing and feedbacks play an important role in controlling the atmospheric and surface temperature. Feedback processes are complex and difficult to quantify and still not completely understood. Local radiative feedbacks such as cloud, water vapor, and albedo feedbacks have been studied using different analysis techniques (Bony et al., 2006; Colman, 2003; Soden and Held, 2006;

Winton, 2006), and will be discussed along with the various methods used to calculate them in chapter 2. However, the role of the local and non-local dynamic feedbacks related to change in vertical energy exchange between the surface and the atmosphere and the horizontal energy transport have not been extensively assessed. In addition, no existing feedback calculation method is able to quantify the individual contributions of the external forcing (doubling of CO₂) alone, and from subsequent feedback processes including water vapor and surface albedo feedbacks, surface sensible and latent heat flux feedbacks, cloud feedback, and large-scale dynamical feedbacks to the 3-D global warming pattern.

Even though the most current version of AOGCMs depicts the current climate with a good level of accuracy, the climate warming projections vary between models and remain a significant issue. The spread in the seasonality and spatial patterns of temperature changes (e.g. the latitude of strongest warming, the timing of the maximum temperature change) can be significant between models (Holland and Bitz 2003, Serreze and Francis, 2006). The IPCC AR4 reported that the range of global warming in response to similar natural and anthropogenic (e.g. doubling of the carbon dioxide concentration) radiative forcing is about 2.1–4.4°C (Randall et al., 2007). Figure 1.4 shows the time and zonal average of the temperature change due to the doubling of CO₂ in 10 IPCC AR4 slab ocean simulations. The inter-model average (thick red line) and all the climate change simulations show an amplified warming at high latitudes, poleward of 50° North and South. Two of the models have a considerably large warming over the Northern Hemisphere that is almost three times as large as their low latitudes warming. The temperature change over the Southern high latitudes is on average smaller than over the Northern high latitudes. Even though the projected global scale of the warming patterns in AOGCMs is generally very similar from model to model, uncertainties in modeling the intensity of future climate change remain an issue and can be attributed to an incomplete understanding of radiative forcing and climate feedback processes (National Research Council, 2008). The inter-model differences in radiative forcing and feedback strengths in turn can be due to differences in the models' physical parameterizations of Earth system processes such as the treatment of cloud, aerosols, soil moisture and sea ice (NRC, 2003; Murphy et al., 2004; Stainforth et al., 2005; Serreze and Francis, 2006).

Over the Arctic it is likely due to parameterization of surface albedo, cloud processes and feedback mechanisms (Moritz et al., 2002). Previous studies on feedbacks found that the climate warming uncertainties are influenced by the representation of local radiative feedbacks such as cloud, water vapor, lapse rate, and surface albedo feedbacks (Bony et al., 2006; Soden et al., 2006). Even with what would seem like a good agreement between model's warming projections, the global effect of individual feedbacks could largely differ from one another but cancel each other, or share common systematic biases. Therefore, it is important to study the relative magnitude of different feedback processes and their contributions to the climate warming projections because it is the first step towards determining the sources uncertainties in model predictions of global warming.

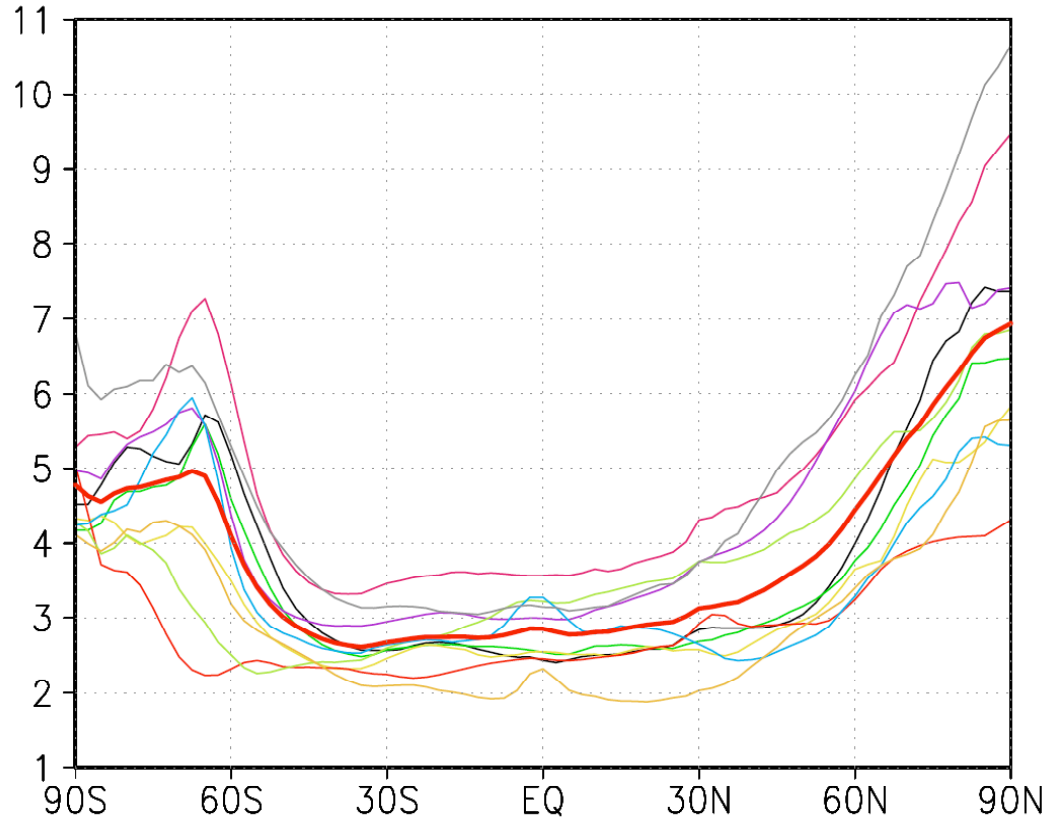


Figure 1.4: Zonal and time average of the surface warming from 10 IPCC AR4 climate models and inter-model average (thick red line). $2 \times \text{CO}_2$ minus control slab ocean climate simulations (units: Kelvin).

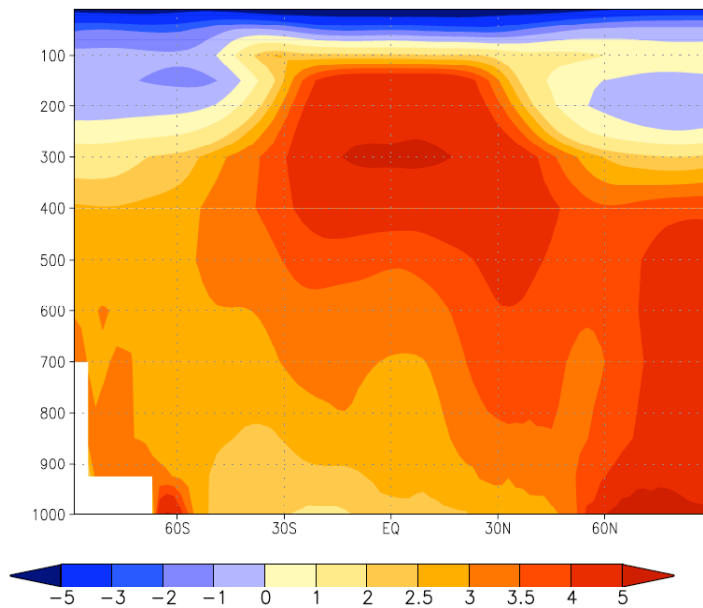
1.1 Objectives

The overall objective of this dissertation is to improve the physical understanding of feedback processes and determine the contribution of the radiative forcing and individual feedback processes to the 3-D warming pattern. The surface and vertical warming projection due to the doubling of CO₂ simulated by the GFDL_CM2.0 climate model is presented in Figure 1.5. The temperature change is in degrees Kelvin and is averaged over latitudes. Similarly to Figure 1.2 and 1.3, the warming pattern shows a large surface polar warming and large upper tropospheric warming in the tropics, which leads to an amplification (reduction) of the temperature gradient at upper levels (surface). A stratospheric cooling is also apparent. The warming over ocean is smaller than the global mean of 2.93 K except over high latitudes. The Northern high latitudes appear to warm at a faster rate than the Southern high latitudes. The main tasks are to compare quantitatively the importance of the radiative forcing, and the subsequent feedback processes, including the water vapor feedback, surface albedo feedback, surface heat flux feedback, and the sum of the large-scale dynamical feedback and change in cloud radiative forcing, to the global warming pattern using a new feedback analysis technique.

1.2 Approach

A new method to be described in sections 2.2 and 4.1 is used to examine the 3-D profiles of the radiative energy flux perturbations due to external forcing, water vapor feedback and surface albedo feedbacks, the non-radiative energy flux perturbations due to the surface turbulent heat flux feedback, and the sum of the large-scale scale dynamical feedback and change in cloud radiative forcing. Then the partial temperature changes associated with each of these individual energy flux perturbations are calculated. These partial temperature changes are additive and their sum is compared with the temperature change produced by the original GFDL_CM2.0 global warming simulation. The calculation of these partial temperature changes enables us to examine the vertical and horizontal distribution of each feedback and their associated temperature change patterns.

(a) Atmospheric warming projection



(b) Surface warming projection

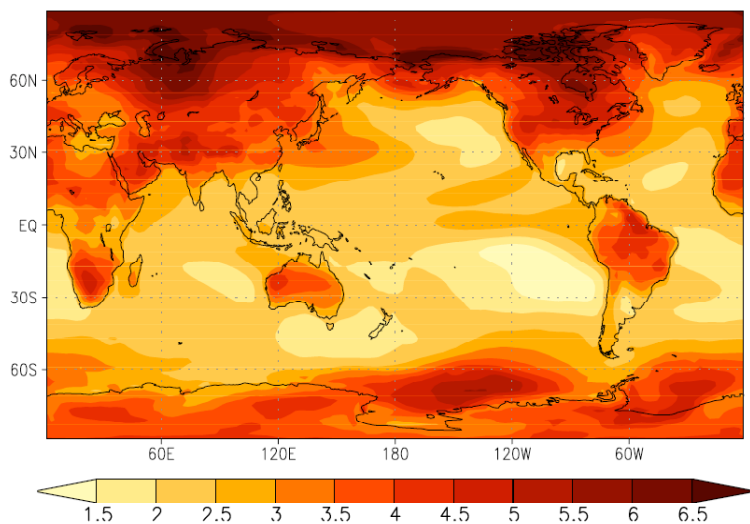


Figure 1.5: Zonal and time mean of: a) the atmospheric and b) the surface warming from the GFDL_CM2.0 climate model, $2 \times \text{CO}_2$ minus control slab ocean climate simulations (units: Kelvin).

1.3 Organization of the Dissertation

The presentation of the dissertation is organized as follows. The next section discusses the relationship between external forcings, climate feedbacks, climate sensitivity, and the climate projection uncertainties. It also provides an overview of the current methods used to calculate climate feedbacks and introduces the new technique used in the dissertation. The current understanding of the role of radiative feedbacks processes is then summarized. The GFDL_CM2.0 IPCC AR4 climate model and its climate simulations are briefly described in chapter 3. The radiation transfer model utilized to calculate the different energy flux perturbations and the implementation of the climate feedback analysis method applied in this dissertation is explained in chapter 4. The efficiency of the method is discussed. The basic climatology of the GFDL_CM2.0 general circulation model is then compared to reanalysis data in chapter 5 to assess its performance in reproducing the present day climate. The following chapter discusses the energy flux perturbation viewed at the TOA from the external forcing and subsequent feedbacks. Chapter 7 presents the vertical and meridional profiles as well as the surface distribution of the energy flux perturbations and associated partial temperature changes due to the external forcing and subsequent feedbacks. The final chapter summarizes the key findings of my dissertation.

CHAPTER 2

BACKGROUND ON CLIMATE FEEDBACKS

The concepts of climate forcing and feedback are closely related to each other. They are addressed in section 2.1 together with the notion of climate sensitivity and its associated uncertainty. The different techniques for analyzing climate forcing and feedbacks are explained in section 2.2. The current understanding of climate forcing and feedbacks and their relation to global warming patterns and strengths are discussed in the last section.

2.1 Concept of Sensitivity, Forcing, Feedback, and, Uncertainty

When subject to an external forcing, the climate system would evolve to a new equilibrium state from its current equilibrium state. The difference between the two equilibrium states is termed as the response of the climate system to the external forcing. The climate system response to an external forcing includes, for example, changes in atmosphere and surface temperature, water vapor, cloud, evaporation/rainfall, and, atmospheric and oceanic circulations. Climate sensitivity is expressed as the amount of changes in a given variable (say temperature) per unit of external forcing, a simple measure that has been used to quantify the effect of an external forcing on the climate. The phrase of climate sensitivity has been used by the scientific community in a variety of ways, the most common definition given by Randall et al. (2007) for the IPCC AR4 is the “global annual mean surface air temperature change experienced by the climate system after it has attained a new equilibrium in response to a doubling of atmospheric CO₂ concentration (forcing)”. In other words it is a response (output of the system) in the form of a temperature change (concerned variable) to an energy input to the system generated by a forcing. The climate sensitivity varies with the type of forcing agent used and its distribution in the atmosphere, the climate mean state, and model

parameterizations (Randall et al., 2007). The forcing agents are external factors perturbing the Earth's energy balance and are quantified as the rate of energy change per unit area (W m^{-2}). Factors responsible for modifying the energy balance consist of natural (e.g. Solar variability, volcanic eruptions) and anthropogenic (input of GHGs and aerosols in the atmosphere, land uses change) forcings. The climate forcing is viewed as the change in net radiative energy flux in the atmosphere and at the surface due to a change in external factors of the climate system. .

The climate sensitivity depends on not only the types of external forcings, but also internal physical and dynamical processes in the climate system. The effects of these internal physical and dynamical processes on the climate sensitivity are called climate feedbacks. As defined by Randall et al. (2007) for the IPCC AR4, a climate feedback is “an interaction mechanism between processes in the climate system where the result of an initial process (i.e. radiative forcing) triggers changes in a second process that in turn influences the initial one”. More specifically it is an energy flux perturbation (input) induced by the system response (output) to an external forcing. The energy flux perturbations are the changes in both the non-temperature induced radiative and non-radiative energy fluxes of the climate system. The feedback agents responsible for the non-temperature induced radiative energy flux perturbations are water vapor, clouds and surface albedo. The non-radiative energy flux perturbations arise from the change in transport of total energy in the atmosphere and ocean, and the changes in the surface turbulent energy exchanges with the atmosphere. An individual climate feedback can either amplify or dampen the external radiative forcing. A positive feedback enhances the original energy input while a negative feedback reduces the original energy input. The climate response is the change in atmospheric and surface temperature in response to climate forcing and subsequent feedbacks. The schematic diagram presented in Figure 2.1 explains the relationship between the response (global temperature change: ΔT), the forcing (doubling of CO_2), and feedbacks.

The classical definitions adopted by the IPCC AR4 differ in their characterization of forcing and response. The change in surface mean temperature is considered to be the climate response to the radiative forcing and at the origin of the generation of feedbacks. The concept of radiative forcing hasn't changed since previous assessments, and is

defined by Ramaswamy et al. (2001) as “the change in the net irradiance at the tropopause due to a change in an external driver of climate change after allowing for stratospheric temperatures to readjust to radiative equilibrium but with surface and tropospheric temperatures and state held fixed at the unperturbed values”. Feedbacks are not induced by the climate system response as a whole, but by the surface temperature change only, and they only affect the TOA radiation budget.

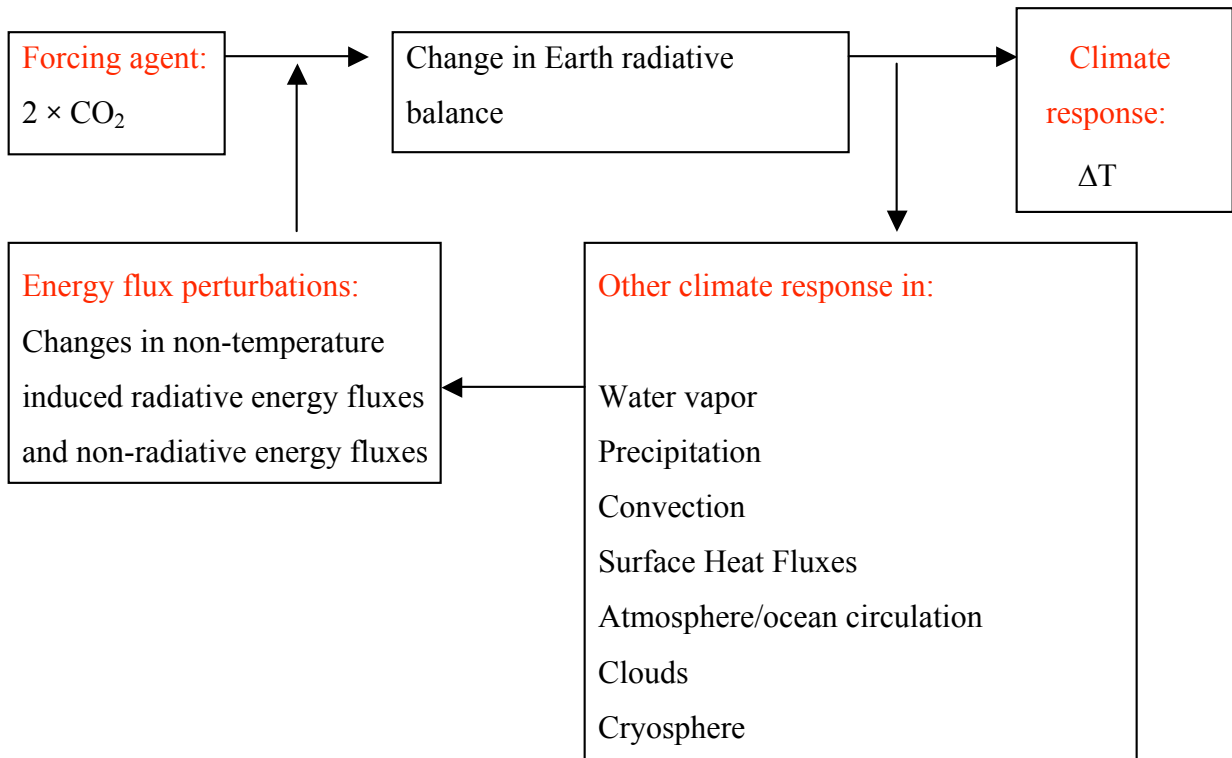


Figure 2.1: Diagram showing the relation between climate forcing, feedback and response.

The current AOGCMs used in the IPCC AR4 have a range of equilibrium climate sensitivity between 2.1 and 4.4 °C. Because all of these IPCC AR4 climate perturbation simulations are supposedly being made with the same forcings, namely anthropogenic radiative forcings, the spread of the climate sensitivity derived from various IPCC AR4 climate perturbation simulations is indicative of uncertainties of our estimate of climate sensitivity using climate models. Most of the climate sensitivity uncertainty is due to the differences in feedbacks in various climate models (Bony et al., 2006). Large

uncertainties remain in the estimation of the radiative feedbacks. Figure 2.2 displays the climate feedback parameters for the water vapor (WV), cloud (C), surface albedo (A), and lapse rate (LR) feedbacks calculated in various recent studies (Colman 2003, Soden and Held 2006, Winton 2006) estimated with different methods, which will be discussed in more details in the next section. The positive (negative) values indicate a positive (negative) feedback corresponding to an amplification (reduction) of the climate sensitivity. The water vapor feedback represents the largest positive feedback, with an average value of 1.8 Wm^{-2} per one degree of global surface warming. All three studies show a spread in the strength of the water feedback parameter that could be due to uncertainties in the representation of physical processes controlling the water vapor in the upper-troposphere. The water vapor feedback is often studied along with the lapse rate feedback, which is negative (Colman, 2003, see section 2.3 for more details). The spread in lapse rate feedback is mainly due to inter-model differences in meridional warming patterns (Soden and Held, 2006). The combined feedback is still positive but much smaller as models with large water vapor feedbacks tend to have large lapse feedbacks. The surface albedo feedback has a small positive value (0.26 Wm^{-2} per one degree of global surface warming on average) and also shows the smallest spread. Qu and Hall (2005) studied these uncertainties and discovered that their sources stem from the parameterization of surface processes. Finally the cloud feedback is positive with an average of 0.69 Wm^{-2} per one degree of global surface warming and has the largest spread. One model even predicts a negative cloud feedback. It is therefore believed that cloud feedback is the primary source for the range in climate sensitivity, which is in agreement with previous study by Cess et al. (1990). This large spread in cloud feedback is in part due to different assumptions about the parameterization of convective and large-scale clouds in climate models. Zhang (2004) and Stephens (2005) gave a review of the concepts of cloud feedback and its role in defining the sensitivity of a climate model. Both studies concluded that the simulation of cloud processes in AOGCMs and their climate feedbacks remains an issue due in part to subgrid-scale dynamics and physics parameterization problems.

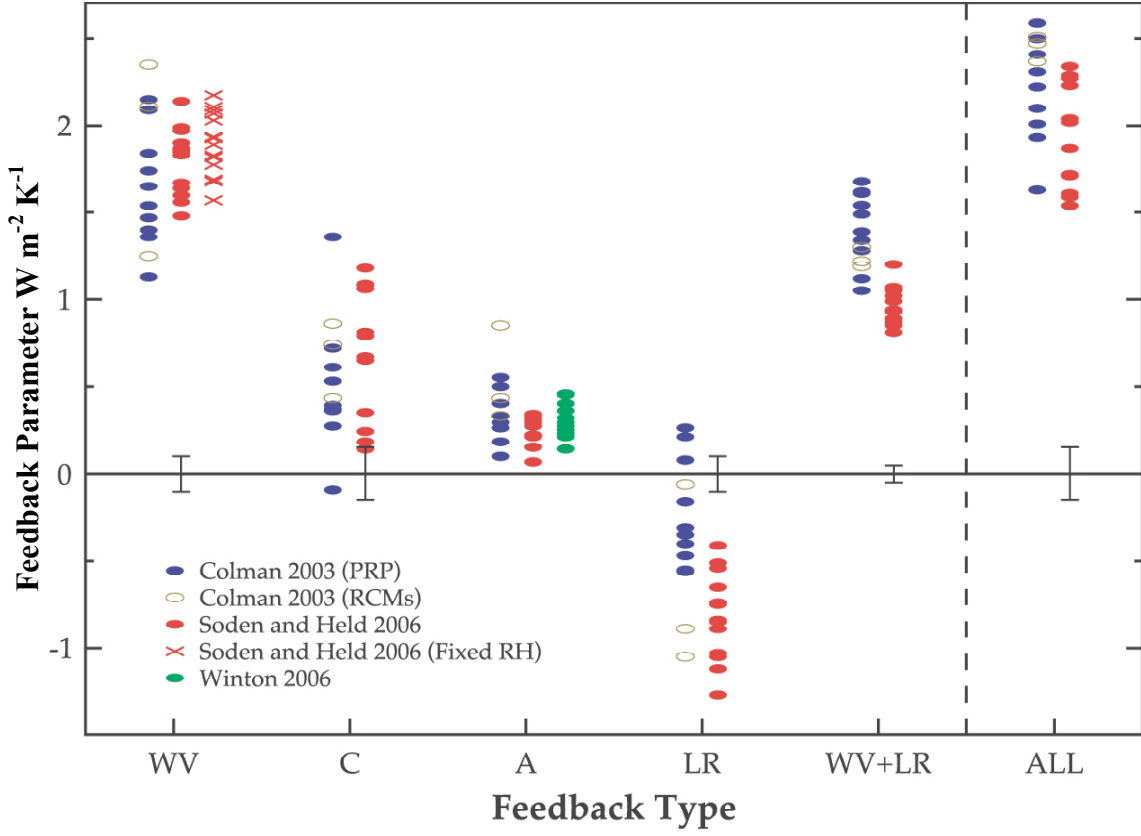


Figure 2.2: Feedback parameters comparison (WV-water vapor, C-cloud, A-albedo, LR-lapse rate) in different studies by Colman (2003), Soden and Held (2006), Winton (2006).

It is known that feedback analysis does not directly address the causal relationship among feedbacks. In feedback analysis, each feedback is assumed to be independent of other feedbacks. What can be answered from feedback analysis is the total effect of each feedback agent on the total climate sensitivity parameter in the PRP method or on the total temperature change in the CFRAM (Climate Feedback-Response Analysis Method). Part of the differences between the spread in each feedback parameter from one study to another (Colman, 2003; Soden and Held, 2006; and Winton, 2006) might be due to the use of different calculation methods (Randall et al., 2007). These methods are discussed in the following section.

2.2 Methods to Study Climate Forcing and Feedbacks

Climate forcing and feedbacks have been diagnosed using different approaches presenting different strengths and weaknesses that are reviewed in this section. The main technique is the partial radiative perturbation (PRP) method. It is described and compared with the new Climate Feedback-Response Analysis Method (CFRAM) developed by Lu and Cai (2008) in the second part of this section.

In the literature, the concept of feedback analysis rests on the Earth radiation balance at the TOA. The simplified Earth energy budget displaying the annual average energy exchanges within the Earth-Atmosphere system is presented in Figure 2.3. At the TOA the global mean radiation budget is balanced. The incoming solar radiation equals the reflected solar radiation and the outgoing longwave radiation. The incoming solar radiation is absorbed by the atmosphere and the surface, and is also reflected by clouds, aerosols, atmosphere, and the surface. The absorbed solar radiation warms the surface and atmosphere and the surface loses energy by emitting longwave radiation via turbulent and convective energy exchange processes (i.e., surface sensible heat and latent heat fluxes). The longwave radiations emitted by the surface are then either absorbed by the atmosphere or radiated directly to space. Part of the energy gained by the atmosphere via absorption is radiated back toward the Earth surface (greenhouse gas effect).

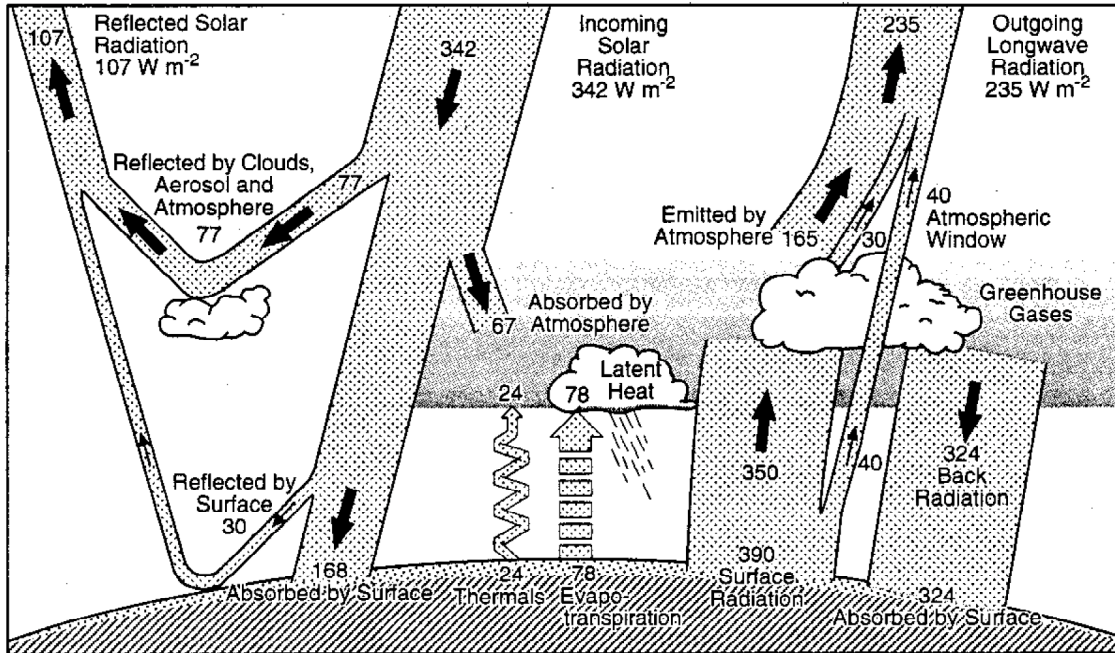


Figure 2.3: Globally averaged energy budget (units: W m⁻²). (Kiehl and Trenberth, 1997).

Although the Earth as a whole is in radiative equilibrium when the TOA net radiation is averaged over a long period of time, locally the climate system does not have to be in radiative equilibrium because of atmospheric and oceanic motions. This is also the case in the climate simulations (control climate and doubling of carbon dioxide) used in this dissertation. Locally the net solar radiation entering the system must therefore balance the infrared radiation leaving the system and the non-radiative energy flux divergence caused by the atmosphere and ocean energy transport. So the local energy balance of the climate system at the TOA is (the symbols for time mean are omitted):

$$S^{TOA} - R^{TOA} + D^{a+o} = 0 \quad (2.1)$$

Where S^{TOA} is the net solar energy flux at the TOA equaling to the solar radiation energy absorbed by the atmosphere and the surface. It depends on the planetary and surface albedo, aerosol and greenhouse gases concentration, and clouds distribution. R^{TOA} is the infrared radiation flux at the TOA and depends on the temperature and humidity profile as well as the distribution of greenhouse gases. D^{a+o} represents the convergence of the total horizontal non-radiative energy flux in the atmosphere and ocean. The energy fluxes

are expressed as the energy flux per unit area expressed in W m^{-2} . The heat storage term is neglected because it is considered very small under steady state condition. Moreover, we treat the ocean as one layer, therefore the heat flux from the interior of the Earth to the ocean is implicitly included in the calculations.

2.2.1 Methods Based on energy balance at the TOA

Nearly all of the existing methods reported in the IPCC AR4 consider the external forcing as an energy flux perturbation at the TOA, which is balanced by the radiative response of the climate system (change in the net energy output of the climate system) under steady state. Feedback agents are viewed as mechanisms that directly affect the radiation budget at the TOA.

CO₂ external forcing and surface temperature change: The external forcing imposed on the climate system by the doubling of CO₂ is defined as a net flux imbalance at the TOA due to the change in CO₂ alone. It is commonly calculated using off-line radiative transfer models and letting the stratospheric temperature readjust to radiative equilibrium and fixing surface and tropospheric temperatures at their control climate values (namely stratospheric adjustment radiative forcing). The stratospheric temperature adjustment is necessary because the stratosphere returns to radiative equilibrium much faster than the troposphere, in approximately one year (Jacob et al., 2005). It can also be calculated instantaneously with atmospheric and surface temperatures fixed (instantaneous radiative forcing), or with only surface temperature fixed and allowing the atmospheric temperature to adjust (zero-surface temperature change radiative forcing). Based on Gregory et al. (2004), the globally averaged external radiative forcing (ΔF) generates a radiative response of the climate system at the TOA, namely $\Delta(S-R)_{\text{due_to_climate_response}}$ in (2. 2), which exactly balances the external radiative forcing when the climate system reaches a new equilibrium state:

$$\Delta(S - R)_{\text{due_to_climate_response}} + \Delta F = 0 \quad (2. 2)$$

The radiative response, $\Delta(S-R)_{\text{due_to_climate_response}}$, is assumed to be proportional to the global mean surface temperature change (ΔT_S), or $\Delta(S-R)_{\text{due_to_climate_response}} = -\lambda \Delta T_S$, where λ is the feedback parameter and the negative sign represents an increase in outgoing radiative energy due to an increase in surface temperature. Therefore, when the climate system readjusts to a new equilibrium state, we have:

$$\lambda \Delta T_S = \Delta F \quad (2.3)$$

Now the response of the climate system due to the forcing is taken to be the surface temperature change only.

Partial radiative perturbation method (PRP): This method was developed by Wetherald and Manabe (1988), and used in many following studies. The feedback parameter λ is equal to the sum of individual feedback parameters due to specific feedback agents (x). The strength of the feedback agent is measured by its feedback parameter (λ_x), equaling to the ratio of the total radiative perturbation at the TOA due to a specific feedback agent ($\frac{\partial(S - R)}{\partial x} \delta x$) to the total change of the surface temperature, namely:

$$\lambda = \sum_x \lambda_x \text{ where } \lambda_x = \frac{\partial(S - R)}{\partial x} \frac{\delta x}{\delta T_S} \quad (2.4)$$

The feedbacks are therefore energy flux perturbations induced by the surface temperature change. Note that $\partial(S - R)$ is the partial change in the net energy input to the climate system which is equal to the partial change in net energy output from the climate system with a negative sign. Therefore, the feedback analysis can be applied regardless of whether the incoming solar energy changes or not. For an anthropogenic radiative forcing, the solar incoming energy does not change but the presence of anthropogenic greenhouse gases would act to reduce the energy output from the climate system, implying a positive forcing. For water vapor feedback, for example, the increase of water vapor in the atmosphere would mainly decrease the energy output, again a positive forcing. For the ice albedo feedback, incoming solar radiation remains the same, but less ice/snow coverage would imply less solar energy being reflected, which acts to increase the energy input to the climate system, a positive forcing. The TOA partial radiative

perturbations are calculated from offline version of model radiation code by substituting the variable considered from a perturbed climate simulation into control climate state. This method assumes that the total radiative energy flux perturbation at the TOA can be linearly decomposed, and neglects the radiative effect of the interaction between feedback agents. This method assumes steady state. It is mostly used with long-time average but the annual cycle of each feedback parameter can be calculated too.

Cloud radiative forcing method (CRF): This method was developed by Cess et al. (1990, 1996) to diagnose climate feedback parameters from changes in TOA clear-sky radiation. The cloud radiative forcing is then computed as the difference between cloudy sky and clear sky net radiation at the TOA:

$$CRF = (S - S_{clr}) - (R - R_{clr}) \quad (2.5)$$

Online feedback suppression: This method was used by Hall and Manabe (1999), Schneider et al. (1999), and Soden et al. (2002) among others. It is used to calculate the partial temperature change due to individual feedback agent. It consists of fixing the vertical profile of a variable that is responsible for the feedback to its profile in the $1 \times \text{CO}_2$ equilibrium state. The difference between the original $2 \times \text{CO}_2$ state and the new $2 \times \text{CO}_2$ equilibrium state in which one feedback is suppressed corresponds to the partial temperature change due to that feedback. The problem arising with this method as discussed in Cai and Lu (2008) is that it includes a “compensation effect” from other feedbacks when a specific feedback is suppressed. Therefore this method cannot be used to calculate the total temperature change under radiative forcing because the partial temperature changes do not add up to the total temperature change. It also would not be suitable for diagnosing feedbacks in climate simulations with larger increase in CO₂.

Radiative Kernel: It is the most recently developed technique by Soden and Held (2006) to study climate feedbacks in a set of 14 twenty-first century climate change experiments generated for the IPCC AR4. It was most recently used by Soden et al. (2008) and Shell et al. (2008) in climate feedback analysis. The method rests on the same feedback definition as the PRP method but proposes the following technique to calculate the

feedback parameter. The feedback parameter (λ) is evaluated in terms of change in global mean surface temperature (T_s) and the change in net radiation at the TOA (S-R)

following (2. 4). Where $\frac{\partial(S - R)}{\partial x}$ is called the “radiative kernel” and represents the changes in TOA fluxes for a standard change in x . It is computed as the difference between the TOA fluxes in a control run present day condition, and the response of TOA radiative fluxes to a same incremental change in x at each atmospheric level (e.g. +1°K for the temperature Kernel, specific humidity increase corresponding to a 1°K temperature increase for the water vapor feedback kernel, or a 1% decrease in surface albedo for the albedo feedback kernel). $\frac{\delta x}{\delta T_s}$ is the climate response computed as the difference between the control and perturbed climate and divided by the change in global mean surface air temperature. Cloud feedbacks cannot be evaluated directly by calculating a cloud radiative kernel because clouds, unlike water vapor, need more than one parameter to represent them, such as cloud area, water and ice content, and water and ice drop size . These cloud properties interact with each other, therefore the cloud kernel method would require to calculate 5 cloud feedback parameters. The cloud feedback can nonetheless be estimated from the change in cloud forcing and the difference between the full-sky and clear-sky kernels.

2.2.2 Climate Feedback-Response Analysis Method (CFRAM)

This method (CFRAM) was recently developed by Lu and Cai (2008) and Cai and Lu (2008) is used in this dissertation. The implementation of the CFRAM for using the GFDL_CM2.0 climate simulation outputs is discussed in details in chapter 4. Here we briefly summarize the main features of the CFRAM. The external forcing has a vertical structure and is therefore computed in CFRAM as the change in the convergence of net radiative energy flux in the atmosphere and the surface. The subsequent feedbacks are not viewed as being induced by the surface temperature change but by the 3-D climate system response (e.g. changes in atmosphere and surface temperature, water vapor,

clouds, precipitation, heat transport). Climate feedbacks are vertical energy flux perturbations that affect the atmospheric and surface temperature (concerned variable) among other climate outputs. Therefore the radiative forcing is not directly proportional to the surface temperature change as assumed in the previous feedback calculation methods. While other methods study feedbacks that directly affect the TOA radiation budget, CFRAM computes the energy flux perturbations due to each feedback in the atmospheric column and at the surface. Therefore, the change in turbulent energy fluxes and horizontal and vertical transport of energy due to oceanic and atmospheric motion are regarded as feedbacks. The partial temperature change due to forcing or feedbacks is then determined by requiring the temperature-induced changes in the infrared radiation to balance the non-temperature induced energy flux perturbation. It represents a major advance in climate feedback calculation because the partial atmospheric and surface temperature changes associated with each individual energy flux perturbations are additive and their sum is comparable with the temperature change produced by the original IPCC global warming simulation as discussed in chapter 7.

The following is the mathematical aspect of the CFRAM. If a radiative forcing $\Delta\bar{F}^{ext}$ is applied, the climate system reaches a new equilibrium, and the difference between the new and unperturbed equilibrium states is:

$$\Delta(\bar{S} - \bar{R}) + \Delta\bar{D} + \Delta\bar{F}^{ext} = 0 \quad (2.6)$$

Δ stands for the change between the two equilibrium states and \bar{D} represents the non-radiative energy flux convergence due to non-radiative energy transport (e.g. horizontal energy transport in atmospheric and surface layers, vertical convection, surface turbulent heat fluxes, friction). The change in the radiative energy fluxes (infrared and solar radiation) due to climate response to $\Delta\bar{F}^{ext}$ can be linearly decomposed into:

$$\Delta\bar{R} = \left(\frac{\Delta\bar{R}}{\Delta\bar{T}} \right) \Delta\bar{T} + \Delta^{(h_2o)}\bar{R} + \Delta^{(c)}\bar{R} \quad \text{and} \quad \Delta\bar{S} = \Delta^{(c)}\bar{S} + \Delta^{(\alpha)}\bar{S} + \Delta^{(h_2o)}\bar{S} \quad (2.7)$$

Where the radiative flux perturbations $\Delta^{(h_2o)}(\bar{S})$ and $\Delta^{(h_2o)}(\bar{R})$ are due to the water vapor change, $\Delta^{(c)}(\bar{S})$ and $\Delta^{(c)}(\bar{R})$ are due to the clouds change, $\Delta^{(\alpha)}\bar{S}$ is due to the surface albedo change, and $\left(\frac{\partial\bar{R}}{\partial\bar{T}} \right) \Delta\bar{T}$ is the infrared energy flux perturbation due to the

temperature change throughout the entire atmosphere-surface column. It is assumed that radiative perturbations can be linearized. This assumption will be discussed and its error calculated in chapter 4.2 and 4.3.

The matrix $\left(\frac{\partial \bar{R}}{\partial \bar{T}}\right)$, which is referred to by Lu and Cai (2008) as the Planck feedback

matrix and is plotted as an example in section 4.1, is written as:

$$\left(\frac{\partial \bar{R}}{\partial \bar{T}}\right) = \begin{pmatrix} \frac{\partial R_1}{\partial T_1} & \dots & \frac{\partial R_1}{\partial T_{M+1}} \\ \vdots & \ddots & \vdots \\ \frac{\partial R_{M+1}}{\partial T_1} & \dots & \frac{\partial R_{M+1}}{\partial T_{M+1}} \end{pmatrix} \quad (2.8)$$

Substituting (2.7) into (2.6) we obtain:

$$\left(\frac{\partial \bar{R}}{\partial \bar{T}}\right) \Delta \bar{T} = \Delta F^{(ext)} + \Delta^{(\alpha)} \bar{S} + \Delta^{(h_2o)} (\bar{S} - \bar{R}) + \Delta^{(c)} (\bar{S} - \bar{R}) + \Delta (\bar{D}) \quad (2.9)$$

The radiation flux change only due to a change in the atmosphere-surface column temperature (LHS of 2.9) is equal to the sum of the radiative energy change due to the external forcing and due to its subsequent feedbacks (RHS of 2.9) in the atmospheric and surface layers.

2.2.3 Special Cases PRP Versus CFRAM at the TOA

Since the PRP method calculates the feedback parameters from the energy flux perturbation at the TOA, we can only compare the PRP method with the CFRAM at the TOA. Applying the vertical sum of the LHS of (2.9) over M atmospheric layers and the surface layer (M+1), $\left(\frac{\partial \bar{R}}{\partial \bar{T}}\right) \Delta \bar{T}$ becomes:

$$\sum_{i=1}^{M+1} \left\{ \sum_{j=1}^{M+1} \frac{\partial R_i}{\partial T_j} \Delta T_j \right\} = \sum_{j=1}^{M+1} \frac{\partial R_{TOA}}{\partial T_j} \Delta T_j = \left(\sum_{j=1}^{M+1} \frac{\partial R_{TOA}}{\partial T_j} \right) \Delta T_S + \sum_{j=1}^{M+1} \left(\frac{\partial R_{TOA}}{\partial T_j} \right) (\Delta T_j - \Delta T_S) \quad (2.10)$$

Equation (2.9), after the vertical summation over all M+1 layers, is then rearranged into:

$$\begin{aligned} & \left(-\sum_{j=1}^{M+1} \frac{\partial R_{TOA}}{\partial T_j} \right) \Delta T_S + \sum_{j=1}^{M+1} \left(-\frac{\partial R_{TOA}}{\partial T_j} \right) (\Delta T_j - \Delta T_S) \\ & + \Delta^{(\alpha)} \bar{S}_{TOA} + \Delta^{(h_2o)} (\bar{S}_{TOA} - \bar{R}_{TOA}) + \Delta^{(c)} (\bar{S}_{TOA} - \bar{R}_{TOA}) - \Delta (\bar{D}_{TOA}) = -\Delta F_{TOA}^{ext} \end{aligned} \quad (2. 11)$$

2.2.3.1 PRP. In the PRP method the forcing is regarded as a radiative flux perturbation at the TOA, the response is a surface temperature change, and the total feedback parameter (λ_{tot}) is the ratio of the radiative flux perturbations at the TOA due to the external forcing to the surface temperature change. The total feedback parameter is equal to the sum of the feedback parameters due to individual climate feedback agents. The feedback parameters λ_{tot} is calculated by dividing (2. 11) by ΔT_S :

$$\lambda_{tot} = \frac{-\Delta F_{TOA}^{ext}}{\Delta T_S} = \lambda_P + \lambda_\Gamma + \lambda_\alpha + \lambda_c + \lambda_w + \lambda_D \quad (2. 12)$$

Where:

$$\begin{aligned} \lambda_P &= \left(-\sum_{j=1}^{M+1} \frac{\partial R_{TOA}}{\partial T_j} \right), \quad \lambda_\Gamma = \sum_{j=1}^{M+1} \left(-\frac{\partial R_{TOA}}{\partial T_j} \right) \frac{(\Delta T_j - \Delta T_S)}{\Delta T_S}, \quad \lambda_\alpha = \frac{\Delta^{(\alpha)} \bar{S}_{TOA}}{\Delta T_S} \\ \lambda_c &= \frac{\Delta^{(c)} (\bar{S}_{TOA} - \bar{R}_{TOA})}{\Delta T_S}, \quad \lambda_{h_2o} = \frac{\Delta^{(h_2o)} (\bar{S}_{TOA} - \bar{R}_{TOA})}{\Delta T_S}, \text{ and } \lambda_D = \frac{-\Delta D_{TOA}}{\Delta T_S} \end{aligned} \quad (2. 13)$$

2.2.3.2 CFRAM at TOA. In the CFRAM method, the forcing is viewed as an external perturbation profile in the atmosphere-surface column at each grid point. The response is a vertically varying atmosphere-surface temperature profile at each grid point. The feedback is any energy flux perturbations that are not caused by the longwave radiation change due to temperature changes. The partial temperature changes can be calculated by dividing (2. 11) by $-\lambda_P$ defined in (2. 13). These partial temperature changes (2. 14) are additive (2. 15).

$$\begin{aligned} \Delta T_S^{tot} &= \frac{\left(-\sum_{j=1}^{M+1} \frac{\partial R_{TOA}}{\partial T_j} \right) \Delta T_S}{-\lambda_P}, \quad \Delta T_S^\Gamma = \frac{\sum_{j=1}^M \left(-\frac{\partial R_{TOA}}{\partial T_j} \right) (\Delta T_j - \Delta T_S)}{-\lambda_P}, \quad \Delta T_S^\alpha \frac{\Delta^{(\alpha)} \bar{S}_{TOA}}{-\lambda_P} \\ \Delta T_S^{h_2o} &= \frac{\Delta^{(h_2o)} (\bar{S}_{TOA} - \bar{R}_{TOA})}{-\lambda_P}, \quad \Delta T_S^c = \frac{\Delta^{(c)} (\bar{S}_{TOA} - \bar{R}_{TOA})}{-\lambda_P}, \quad \Delta T_S^D = \frac{-\Delta (\bar{D}_{TOA})}{-\lambda_P}, \end{aligned} \quad (2. 14)$$

$$\text{and } \Delta T_S^P = \frac{\Delta F_{TOA}}{-\lambda_p}$$

$$\text{So that } \Delta T_S^{tot} = \Delta T_S^P + \Delta T_S^\Gamma + \Delta T_S^\alpha + \Delta T_S^c + \Delta T_S^{h_2o} + \Delta T_S^D \quad (2.15)$$

2.3 Major Findings on Climate Forcing and Feedbacks

The observed global temperature changes during the past 50 years are primarily a response to radiative forcing (Hansen et al., 2002). The forcing by the well-mixed GHGs has increased steadily over the past 50 years and represents about 70% of the increase since 1850 (Hansen et al., 1998). The atmospheric concentration of CO₂ has increased by about 25% since 1850 corresponding to the beginning of industrialization, from 280 part per million by volume to the current concentration of 384 ppmv (Peixoto and Oort, 1992). Carbon dioxide is a strong absorber of infrared radiations but is relatively transparent to shortwave radiation. The increase of CO₂ has caused the largest radiative forcing among all the principal radiative forcings (natural or human induced) included in the climate simulation between the years 1750 and 2005 as displayed in Figure 2.4 (taken from Forster et al., 2007). A positive (negative) value of radiative forcing signifies an increase (decrease) of energy of the Earth system generating a warming (cooling) of the climate. GHGs generate a positive radiative forcing at any given concentration because they absorb and emit outgoing longwave radiations, therefore creating a positive radiative energy perturbation at the TOA (that is balanced by the Earth radiative response under steady state). A CO₂ concentration of 379 ± 0.65 ppm (Forster et al., 2007) produces a radiative forcing of 1.66 W m⁻², and for a doubling of CO₂ mixing ratio the radiative forcing is calculated to be 3.7 W m⁻². A study by Collins et al. (2006) presents the comparison between the GHGs radiative forcing computed by radiative parameterizations of IPCC AR4 models and by line-by-line codes revealed that the majority of the uncertainties in radiative forcing are due to radiative transfer assumptions in AOGCMs radiation parameterization.

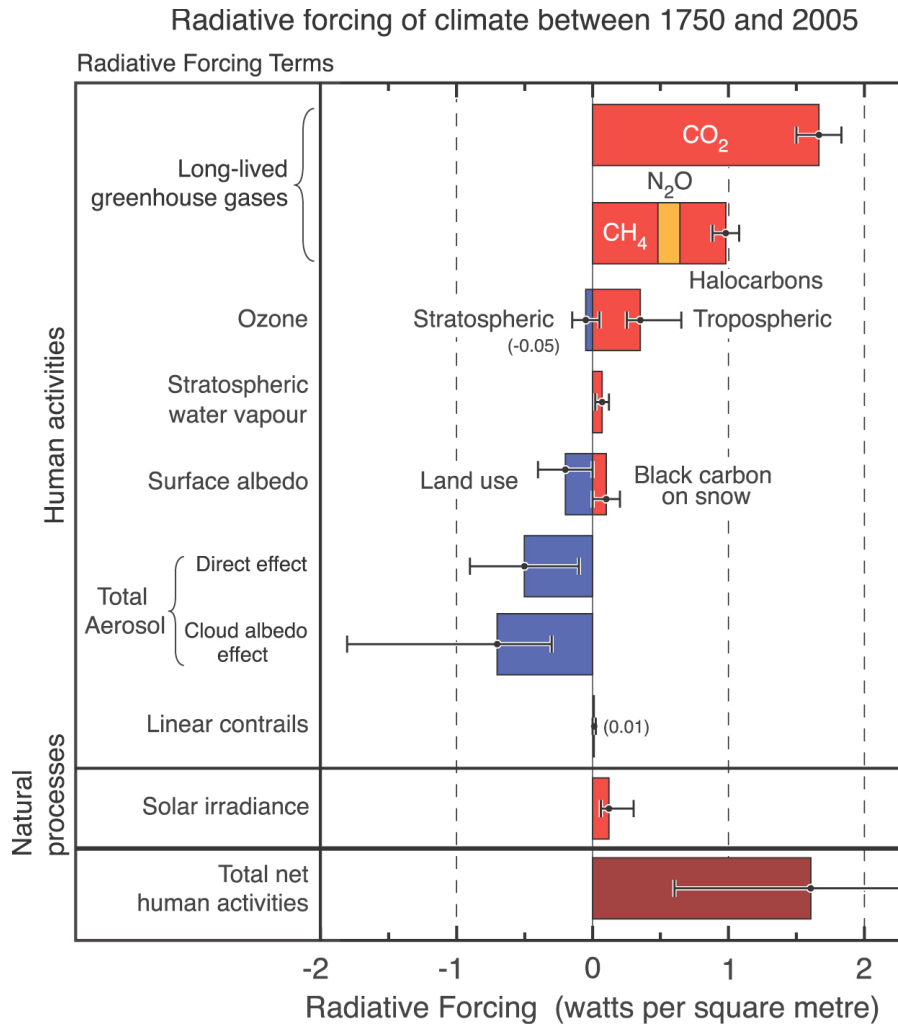


Figure 2.4: Strength of radiative forcing from human activity and natural processes in 2005 relative to year 1750. (Forster et al., 2007).

Both AOGCM warming simulations and observed warming derived from instrumental data are characterized by a high-latitude amplification and larger warming over land than oceans (Hansen et al., 2006). It is largely the result of the local surface albedo feedback (Budyko 1969; Sellers 1969; Manabe and Stouffer 1980; Randall et al. 1994; Holland and Bitz 2003; Hall 2004). The surface albedo feedback is an interaction mechanism that enhances the climate change mostly over snow and ice covered regions. The atmospheric warming generated by the increase in GHGs causes snow and sea ice to retreat. The lower albedo (or fraction of solar energy reflected) of the exposed land and ocean results in an increase in solar radiation absorbed at the surface, generating an additional warming over land and ocean which will further melt the cryosphere. The

surface albedo feedback is therefore positive and about half of the warming over high latitudes under a $2 \times \text{CO}_2$ forcing was found to be due to the albedo feedback (Hall, 2004). Numerous studies have calculated this feedback with a good degree of agreement between models even though they use different sea-ice or land components. Colman (2003) found a mean surface albedo feedback of $0.36 \text{ W m}^{-2} \text{ K}^{-1}$. Winton (2006) estimated the surface albedo feedback in 12 IPCC AR4 climate models and found a value of $0.3 \text{ W m}^{-2} \text{ K}^{-1}$ to be strongly associated with local temperature change in the Northern Hemisphere. Bony et al. (2006) concluded that strength of the northern hemisphere surface albedo feedback associated with snow changes remains uncertain and can be at the origin of divergences between models. The source of divergences of high latitude warming simulations between models is still not clear (Randall, 2007). The surface albedo feedback is not the only mechanism causing the much stronger warming in the extratropics. Cloud feedback and poleward heat transport are also found to be important contributors (e.g., Holland and Bitz 2003; Cai 2005, 2006; Winton 2006).

Water vapor is the most important GHG source of opacity for outgoing longwave radiations in the atmosphere, responsible for 60% of the natural greenhouse effect for clear skies (Kiehl and Trenberth, 1997). It provides the largest feedback in model projection of climate change (Figure 2.2) (Held and Soden 2000; Bony et al., 2006). The saturation vapor pressure (e_s) in the atmosphere is determined by the Clausius-Clapeyron relation that describes a quasi-exponential increase in saturation pressure of water vapor as temperature (T) rises:

$$e_s \propto \exp\left(-0.622 \frac{L}{R_d T}\right) \quad (2.16)$$

Where L is the latent heat of the phase transition, and R_d is the gas constant for dry air (Peixoto and Oort, 1992). Under GHG forcing, the relative humidity remains constant as observed and modeled (Randall et al., 2007), therefore an increase in temperature must generate an increase of water vapor in saturated air. Theory thus predicts a strongly positive water vapor feedback in response to global warming. Indeed, as noted in Figure 2.2, the largest positive feedback in all models is provided by the change in water vapor. Confidence in modeled distribution and variation of water vapor feedback is affected by

uncertainties in the physical processes controlling upper-tropospheric humidity and confidence in their representation in GCMs (Bony et al., 2006). The water vapor feedback is often studied along with the lapse rate feedback (Colman, 2003) because temperature and saturation pressure of water vapor are related in the atmosphere by the Clausius-Clapeyron equation. As a response to radiative forcing, the low latitudes warm at a faster rate higher in the troposphere than near the surface, which increases the emission of longwave radiations to space following the Stefan-Boltzmann law that states that the flux density emitted by a black body ($B(T)$) is proportional to the fourth power of the absolute temperature (T):

$$\pi B(T) = \sigma T^4 \quad (2.17)$$

Where σ is the Stefan-Boltzmann constant. This creates a negative feedback that dominates when averaged globally.

Clouds also directly affect the radiative transfer in the atmosphere. They reflect solar radiation to space, shielding the surface, and absorb and emit infrared radiations, adding extra energy to the atmosphere-surface system. The study of cloud feedback attempts to elucidate how the two effects vary as climate warms. A variety of cloud properties affect the radiations budget of the Earth such as the cloud height, its optical depth, or liquid and ice content (Stephens, 2005). Cloud forcing has consistently been found to be the major source of uncertainty in climate feedback analysis as it is a very complex process that interacts with other feedbacks such as the water vapor feedback and the surface albedo feedback, which makes it difficult to quantify (e.g. Cess et al., 1990; Bony et al., 2006; Randall et al., 2007; Dufresne and Bony, 2008). On a global average the cloud feedback is positive but the different feedback analysis techniques provide a range results. The CRF method by definition calculates the difference between cloudy and clear-sky atmosphere radiation, which depends on changes in water vapor, temperature, and surface albedo properties (Soden et al., 2004; Bony et al., 2006). On the other hand, the PRP method diagnoses the feedback from changes in cloud properties only but assumes that all fields are uncorrelated.

Another important dynamical factor for the spatial variation of climate sensitivity is the change in surface turbulent heat fluxes. These fluxes have been found to serve an important role in damping the warming response to radiative forcing, especially over low latitudes where the annual mean loss of thermal energy by evaporation is about 100 W m^{-2} (Hartmann, 1994). Evaporative cooling doesn't damp the high latitude warming as efficiently as in low latitudes (Hassol, 2004) where it stabilizes the SST, because this negative evaporation feedback is related to the surface temperature by the Clausius-Clapeyron equation. The surface turbulent flux feedback is also responsible for warming disparities between different regions over land, depending on the moisture available for evaporation. A study by Frankignoul et al. (2004) calculated the surface heat flux feedback using observations and model simulations and found that the turbulent heat flux feedback is negative over the Atlantic and the extra-tropical Indo-Pacific, and dominates the surface heat flux feedback over the extra-tropics. The evaporation and surface sensible flux feedbacks do not directly affect the TOA radiative fluxes and CFRAM enables its calculation. A study by Castet and Cai (2007) estimated the surface flux feedback patterns and their related temperature changes using CFRAM technique with 5 IPCC AR4 model simulations. The net temperature change patterns in response to total surface flux feedbacks were found to be positive in the mid-latitudes, Arctic region, and equatorial Pacific, but negative in sub-tropics and over Antarctica. It is important to remind that the feedback values can differ between climate models and also with observations, partly because the coarse resolution of climate models do not allow a good representation of surface turbulent heat fluxes.

Non-local feedback mechanisms associated with the changes in the atmospheric circulation also play an important role in causing the much stronger warming in the extratropics. Recent modeling studies have shown that, under radiative forcing, a poleward warming amplification would still be present in the absence of the ice-albedo feedback (Alexeev et al., 2005; Hall, 2004). The theoretical work reported in Cai (2005, 2006) and Cai and Lu (2007) shows that the atmospheric poleward heat transport effectively acts to strengthen the atmospheric greenhouse forcing in high latitudes. This is done by warming the high latitude atmosphere and thereby enhancing the downward

infrared radiation to the high-latitude surface while reducing the atmospheric greenhouse forcing by cooling the low latitude atmosphere, which in turns damps the downward infrared radiation to the low latitude surface. Modeling evidences of the so-called non-local dynamical feedback was revealed in Castet (2005) in 14 climate model simulations produced for the IPCC AR4, which showed an increase in the net radiation energy surplus (deficit) at the TOA in low (high) latitudes implying an increase of poleward heat transport in response to an anthropogenic radiative forcing. In addition, the analysis of the change in net radiation budget difference between the surface and the TOA, and the change in moisture budget (evaporation minus precipitation) implied an upward trend in the atmospheric poleward latent heat transport. Similarly to the surface heat flux feedback, this feedback cannot be calculated by any other existing method but CFRAM because it does not directly affect the TOA radiations.

CHAPTER 3

DATA

The data used throughout this research come from the GFDL_CM2.0 model simulation output, provided by the Program for Climate Model Diagnosis and Intercomparison (http://www-pcmdi.llnl.gov/ipcc/about_ipcc.php). This group is archiving coupled ocean-atmosphere general circulation model output to support the Working Group 1 component of the Intergovernmental Panel on Climate Change's (IPCC) 4th Assessment Report. The GFDL_CM2.0 model was chosen based on its sensitivity value, 2.93 K, which well within the range given by the IPCC AR4 climate models (2.1–4.4 K, Randall et al., 2007). This model does not use flux adjustment (an artificial adjustment of the surface heat, water and moment fluxes), and it also output all the necessary fields to compute the radiative energy flux convergence at each layer and at the surface. The model characteristics are listed in Table 3.1, more specifications are given in appendix A. The GFDL_CM2.0 model is one of the two latest general circulation models developed at NOAA's GFDL. The atmosphere, land, and sea-ice components of the CM2.0 are coupled to a slab ocean of 50 m depth. A 50-year simulation was archived for the control climate, but the specific humidity data was not available for the year 37 over different pressure levels, therefore the long-term averages were computed over the last 13 years of the model simulations in both control and the doubling of CO₂ experiments.

The data used as input to the radiation scheme described in Section 4.2 to calculate the partial temperature change caused by the external forcing and the different feedbacks are the incoming shortwave radiations at the TOA, and the surface pressure, temperature, and shortwave radiations (to compute the surface albedo). It also uses the 3-dimensional (17 pressure levels) profiles of ozone mixing ratio, specific humidity and atmospheric temperature from the GFDL_CM2_0.

Table 3.1: GFDL_CM2.0 model characteristics.

Institution	Geophysical Fluid Dynamics Laboratory (GFDL)
Model name	CM2.0
Components	AM2P13 – atmosphere Slab ocean LM2 – land SIS – sea ice
Atmospheric chemistry?	No
Interactive biogeochemistry?	No
What aerosols	Organic and black carbon, dust (constant) sulphate, and sea salt
Indirect effects modeled?	No indirect yet
Dynamic vegetation?	No
Ice-sheets?	No
Resolution	Latitude: 90, Longitude: 144 ($2^\circ \times 2.5^\circ$)
Years	100 yrs $2 \times \text{CO}_2$, and 50 yrs control climate

The data are derived from the monthly mean outputs of an instantaneous carbon dioxide doubling ($2 \times \text{CO}_2$) slab ocean simulation and its corresponding slab ocean control simulation (experiments 10 and 11 in the PCMDI data portal). The only varying forcing agent between the two simulations is carbon dioxide; other forcing agents are held constant in both control and the doubling of CO_2 experiments. The models were run until they reached a true equilibrium state and produced stable statistics for at least 20 years beyond equilibrium. Both experiments include a prescribed heat flux into the ocean layer, Q -flux, to keep the surface temperature of the ocean close to climatological values in the absence of ocean currents. The Q -flux substitutes the heat that would be transported if the model included currents and therefore accounts for the divergence of heat flux by the ocean circulation. The same Q -flux is used in both the control and $2 \times \text{CO}_2$ experiments meaning no change in the ocean heat transport (Stouffer et al., 2006).

CHAPTER 4

METHODOLOGY

4.1 Radiation Transfer Model

We use the radiation transfer model developed by Fu and Liou (1993, referred to as FL_RAD, hereafter) to compute all required radiative energy fluxes for feedback analysis using the GFDL_CM2.0 climate simulation outputs. FL_RAD is a delta-four-stream radiative transfer algorithm for plane-parallel atmospheres. The non-gray gaseous absorption due to H₂O, CO₂, O₃, O₂, N₂O, and CH₄ has been parameterized using the correlated k-distribution (Fu and Liou, 1993; Fu et al., 1998).

The solar energy input (the downward solar radiation at the TOA) used in our calculations is directly taken from the outputs of the GFDL_CM2.0. The surface shortwave albedo is computed as the ratio between the upward and downward shortwave radiation flux at the surface. If there is no incoming solar radiation at the surface (e.g., over winter polar cap), the albedo is set to zero. The output files of the GFDL_CM2.0 climate simulations archived by the Program for Climate Model Diagnosis and Intercomparison only have total cloud liquid/ice water content and total cloud fraction area. As a result, we only perform clear-sky radiation calculations as explained in the next section.

Except the concentration level of CO₂, which is set to be identical to the value used in the GFDL_CM2.0 climate simulations (352 ppmv for control experiment and 704 ppmv for the doubling of CO₂ experiment), the concentration levels of all other permanent greenhouses gases are set to be the values used in the original FL_RAD model (e.g., 1.6 ppmv for CH₄ and 0.28 ppmv for N₂O) in all levels. The atmospheric temperature, water vapor, and Ozone profiles used in our radiation calculations are derived from the outputs of the GFDL_CM2.0 climate simulations.

The usage of FU_RAD, instead of the original radiation transfer model in the GFDL_CM2.0 climate system would cause some differences between our offline clear-

sky radiation calculations and the clear-sky radiation fluxes derived directly from the archive of the GFDL_CM2.0 climate simulations. Soden and Held (2006) determined after comparing radiative transfer components from different models that the differences generated by using a single radiative transfer model is about 10%. Obviously, the surface albedo calculated by us could be somewhat different from the actual surface albedo used in the original GFDL climate simulations (the archive does not include the surface albedo field). This would affect accuracy of our offline radiation calculations. Another important factor that would affect the accuracy of our offline radiation calculations is that the archived data have been subject to postprocessing, which interpolates the original data on the sigma levels (25 levels) to pressure levels (17 levels).

Furthermore, our offline radiation calculations are made with monthly mean of daily means of atmospheric water vapor and temperature climatological profiles, while the radiation fields in the outputs of the GFDL climate simulations are the monthly mean climatology of the radiation fields based on instantaneous profiles of atmospheric water vapor and temperature. This may affect mid and high latitudes where large synoptic scale variations in atmospheric moisture content occur. Therefore, part of the errors in our radiation calculations is simply due to the nonlinearity in the radiation model.

Table 4.1: Globally averaged longwave (LW) and shortwave (SW) radiation flux at the surface and the TOA, and RMS error (unit: W m^{-2}).

	TOA	TOA	SURFACE	SURFACE	SURFACE
	Upward SW	Upward LW	Downward SW	Upward SW	Downward LW
GFDL_CM2.0	53.55	259.98	246.23	31.07	314.45
FL_RAD	61.77	272.75	238.59	30.57	301.05
RMS	9.53	13.32	11.89	1.66	15.21

Table 4.1 summarizes the global and time averages of the clear-sky radiative fluxes at the TOA and at the surface obtained from our offline calculations using FL_RAD and derived from the outputs of the GFDL_CM2.0 control run climate simulations ($1 \times \text{CO}_2$ experiments). The last row lists the root mean square (RMS) error. It is seen that except for the upward solar radiation at TOA, the difference between our offline calculations and the original online radiation fluxes calculated by the

GFDL_CM2.0 is within 5%, much smaller than the 10% level reported in Soden and Held (2006), despite these possible factors discussed in previous paragraph that would affect the accuracy of our radiation calculations. For example, the percentage errors in outgoing longwave radiations at the TOA, downward solar radiation at the surface, upward solar radiation at the surface, and downward longwave radiation at the surface, are 4.9%, 3.1%, and 1.6%, and 4.3%, respectively. The RMS error also gives a measure of the difference between the two radiation calculations, and the error ranges between 1.66 W m^{-2} for the upward solar radiation at the surface and 15.21 W m^{-2} for the downward longwave radiation at the surface which is only slightly larger than the mean difference values. The largest errors in our clear-sky radiation calculations are found in the reflected shortwave radiation at the TOA, which is as large as 15.3 %, or an RMS error of 9.53 W m^{-2} . A possible explanation is that the FL_RAD produces a larger scattering of solar radiation radiations back to space than the GFDL_CM2.0 model. This factor alone is also responsible for a smaller amount of solar radiation reaching the surface, which in turns also contributes to the error in the reflected solar radiation at the surface. The fact that the error in the reflected solar radiation at the surface is smaller implies that our estimate of the surface albedo by using the ratio of the upward solar radiation to the downward solar radiation at the surface is sufficiently accurate. In terms of longwave radiation, we see that our radiation calculations overestimate (underestimate) outgoing (downward) longwave flux at the TOA (at the surface). Again, these errors could be due to the use of the FL_RAD instead of the GFDL_CM2.0 radiation model. Another possible explanation is the interpolation from the 24 native sigma levels to the 17 pressure levels in the GFDL postprocessing programs could effectively increase atmospheric water vapor in the upper levels. This factor alone would be responsible for more shortwave scattering at the TOA, more outgoing longwave radiation at the TOA, less solar radiation reaching at the surface, and less downward longwave radiation (or weaker greenhouse effect) at the surface. Nevertheless, the overall error in our offline radiation calculations is within 6%, smaller than 10% reported in Soden and Held (2006).

4.2 Implementation of CFRAM

We have implemented Climate Feedback-Response Analysis Method (CFRAM) developed by Lu and Cai (2008) using FL_RAD model. We use the FL_RAD model to calculate vertical profiles of radiative energy fluxes at each grid point. For a given grid point, we then calculate the vertical profile of the convergence of the radiative energy, denoted as \vec{F}_{net} (from now on, we use a vector to denote the vertical profile of the variable under consideration). The radiative energy flux convergence, \vec{F}_{net} , at each atmospheric layer (l) is computed according to

$$F_{net}(l) = f_d(l) - f_d(l+1) + f_u(l+1) - f_u(l) \quad (4.1)$$

And at the surface ($M+1$) as:

$$F_{net}(M+1) = f_d(M+1) - f_u(M+1) \quad (4.2)$$

Where F_d and F_u represent the net downward and upward radiation at the specific level as displayed in Figure 4.1.

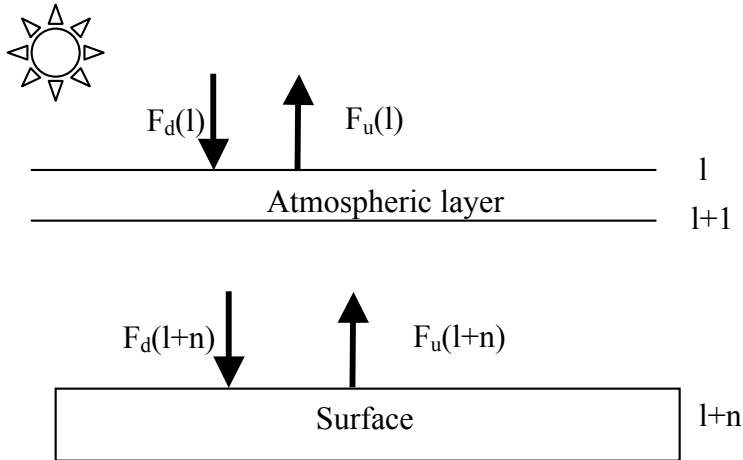


Figure 4.1: Diagram of the radiative energy flux convergence between levels l and $l+1$ and at the surface.

Now, we are ready to discuss how to calculate the radiative energy flux convergence perturbation due to each feedback term. As discussed in the previous section, because the IPCC AR4 doesn't provide detailed cloud information (e.g.: liquid

water or ice water content), the effect of clouds on atmospheric radiations cannot be calculated directly. The radiation fluxes in the atmosphere are decomposed into clear-sky radiation fluxes and cloud forcing (Cf) following

$$\bar{S} - \bar{R} + \bar{C}f_{total} = \bar{S}^{total_sky} - \bar{R}^{total_sky} \quad (4.3)$$

Therefore the energy balance equation (2. 1) is rewritten as

$$\bar{S} - \bar{R} + \bar{C}f_{total} + \bar{D} = 0 \quad (4.4)$$

Then, if an external forcing perturbation is applied, in this case the doubling of the CO₂ concentration, the climate system reaches a new equilibrium state and the difference between the two states is written as

$$\Delta(\bar{S} - \bar{R}) + \Delta(\bar{C}f_{total} + \bar{D}) = 0 \quad (4.5)$$

However, as Soden et al. (2004) discussed, strictly speaking, ΔCf include partial effects of other feedbacks, including surface albedo feedback. Following Lu and Cai (2009), we can take out part of $\Delta D + \Delta Cf_{total}$ inferred from $-\Delta(S - R)$ that is associated with surface albedo feedback in order to properly account for the surface albedo feedback.

At surface the cloud radiative forcing is decomposed into its longwave and shortwave components as

$$-\Delta(S - R)_{surface} = \Delta D_{surface} + (\Delta Cf_{total_solar} - \Delta Cf_{total_longwave})_{surface} \quad (4.6)$$

The shortwave radiation part of the cloud radiative forcing is then

$$Cf_{total_solar} = (S^{\downarrow} - S^{\uparrow})^{cld} - (S^{\downarrow} - S^{\uparrow}) = (1 - \alpha)S^{\downarrow,cld} - (1 - \alpha)S^{\downarrow} = (1 - \alpha)(S^{\downarrow,cld} - S^{\downarrow}) \quad (4.7)$$

Therefore the change in cloud radiative forcing is:

$$\Delta Cf_{total_solar} = \Delta[(1 - \alpha)(S^{\downarrow,cld} - S^{\downarrow})] = (1 - \alpha_{CO_2})\Delta(S^{\downarrow,cld} - S^{\downarrow}) - \Delta\alpha(S^{\downarrow,cld} - S^{\downarrow}) \quad (4.8)$$

Now let us define $\Delta Cf_{solar} = (1 - a_{1co2})\Delta(S^{\downarrow,cld} - S^{\downarrow})$. Equation (4.6) becomes,

$$\begin{aligned} -\Delta(S - R)_{surface} + \Delta\alpha(S^{\downarrow,cld} - S^{\downarrow})_{surface} &= \Delta D_{surface} + (\Delta Cf)_{surface} \\ &= \Delta D_{surface} + (\Delta Cf_{solar} - \Delta Cf_{total_longwave})_{surface} \end{aligned} \quad (4.9)$$

Therefore, we can use $-\Delta(S - R)_{surface} + \Delta\alpha(S^{\downarrow,cld} - S^{\downarrow})_{surface}$ to infer $(\Delta\bar{D} + \Delta\bar{C}f)$ over the entire column (see Eq. (4.15) below), which will not include the surface albedo effect in the change of cloud forcing. Note other effects, such as water vapor feedbacks, may still be included in the changes in cloud forcing. Without actual cloud information, we cannot remove the water feedback effects in the cloud forcing.

The clear-sky shortwave and longwave radiative energy flux perturbations ΔS and ΔR are then decomposed into,

$$\Delta\bar{R} = \left(\frac{\partial\bar{R}}{\partial\bar{T}} \right) \Delta\bar{T} + \Delta^{(CO_2)}\bar{R} + \Delta^{(h_2o)}\bar{R} + \Delta^{(\alpha)}\bar{R}, \text{ and } \Delta\bar{S} = \Delta^{(CO_2)}\bar{S} + \Delta^{(h_2o)}\bar{S} + \Delta^{(\alpha)}\bar{S} \quad (4.10)$$

Where $\left(\frac{\partial\bar{R}}{\partial\bar{T}} \right) \Delta\bar{T}$ is change in longwave radiation flux divergence in each layer due to the temperature change, $\Delta^{(CO_2)}(\bar{S} - \bar{R})$ is the radiative energy flux perturbation due to the external forcing alone, $\Delta^{(h_2o)}(\bar{S} - \bar{R})$ is due to the water vapor feedback, and $\Delta^{(\alpha)}(\bar{S} - \bar{R})$ is due to the surface albedo feedback. Note that $\Delta^{(\alpha)}(\bar{S} - \bar{R})$ in (4.10) includes the term $\Delta\alpha(S^{\downarrow,cld} - S^{\downarrow})_{surface}$ that has been removed from the cloud forcing calculation, as indicated in Eq. (4.14) below. Eq. (4.10) is the linearized longwave and shortwave fluxes by using the multivariate Taylor series expansion, and the higher order terms that correspond to energy flux perturbation arising from interactions between feedbacks are omitted. We do not assume that individual processes are physically independent of each other, but instead we calculate the post-process energy flux perturbations. The errors introduced by this simplification are discussed in the next section.

Substituting (4.10) to (4.5) and making use of (4.9), we obtain

$$\left(\frac{\partial\bar{R}}{\partial\bar{T}} \right) \Delta\bar{T} = \Delta^{(CO_2)}(\bar{S} - \bar{R}) + \Delta^{(h_2o)}(\bar{S} - \bar{R}) + \Delta^{(\alpha)}(\bar{S} - \bar{R}) + \Delta(\bar{C}f + \bar{D}) \quad (4.11)$$

These energy flux perturbations are calculated by taking the difference of the energy flux term between the $1 \times \text{CO}_2$ state (baseline state) and a perturbed state in which the vertical profile of the variable responsible for the feedback is fixed to its $2 \times \text{CO}_2$ value. These are the first order terms of the Taylor series expansion, again the importance of the higher order terms neglected will be quantified in the following section.

$$\Delta^{(\text{CO}_2)}(\bar{S} - \bar{R}) = (\bar{S} - \bar{R})\Big|_{T_{1\text{CO}_2}, q_{1\text{CO}_2}, \alpha_{1\text{CO}_2}, 2\text{CO}_2} - (\bar{S} - \bar{R})\Big|_{T_{1\text{CO}_2}, q_{1\text{CO}_2}, \alpha_{1\text{CO}_2}, 1\text{CO}_2} \quad (4.12)$$

$$\Delta^{(h_2o)}(\bar{S} - \bar{R}) = (\bar{S} - \bar{R})\Big|_{T_{1\text{CO}_2}, q_{2\text{CO}_2}, \alpha_{1\text{CO}_2}, 1\text{CO}_2} - (\bar{S} - \bar{R})\Big|_{T_{1\text{CO}_2}, q_{1\text{CO}_2}, \alpha_{1\text{CO}_2}, 1\text{CO}_2} \quad (4.13)$$

$$\Delta^{(\alpha)}(\bar{S} - \bar{R}) = (\bar{S} - \bar{R})\Big|_{T_{1\text{CO}_2}, q_{1\text{CO}_2}, \alpha_{2\text{CO}_2}, 1\text{CO}_2} - (\bar{S} - \bar{R})\Big|_{T_{1\text{CO}_2}, q_{1\text{CO}_2}, \alpha_{1\text{CO}_2}, 1\text{CO}_2} + \begin{pmatrix} 0 \\ -\Delta\alpha(S^{\downarrow, \text{cld}} - S^{\downarrow})_{\text{surf}} \end{pmatrix} \quad (4.14)$$

Where the last term in (4.14) represents the correction to the clear-sky estimation of the surface albedo feedback that has been taken out from the cloud forcing term as discussed above, which is zero in the atmosphere and at the surface equals to $-\Delta\alpha(S^{\downarrow, \text{cld}} - S^{\downarrow})_{\text{surf}}$.

Note that $(S^{\downarrow, \text{cld}} - S^{\downarrow})_{\text{surf}}$ is obtained from the GFDL outputs.

The last term on the right hand side of (4.11) is the sum of the non-radiative energy flux change and change in cloud forcing plus the correction to the clear-sky albedo surface feedback term. This term can be evaluated as

$$\Delta(\bar{Cf} + \bar{D}) = -\left((\bar{S} - \bar{R})\Big|_{T_{2\text{CO}_2}, q_{2\text{CO}_2}, \alpha_{2\text{CO}_2}, 2\text{CO}_2} - (\bar{S} - \bar{R})\Big|_{T_{1\text{CO}_2}, q_{1\text{CO}_2}, \alpha_{1\text{CO}_2}, 1\text{CO}_2}\right) + \begin{pmatrix} 0 \\ \Delta\alpha(S^{\downarrow, \text{cld}} - S^{\downarrow})_{\text{surf}} \end{pmatrix} \quad (4.15)$$

The archives of the GCM climate simulations include non-radiative energy fluxes at surface, namely, the surface turbulent sensible and latent heat fluxes. The perturbations in these two terms can be calculated directly using the outputs from the

GFDL climate simulations as the long time mean difference between the $2 \times \text{CO}_2$ and control simulations of the latent (LH) and sensible (H) heat fluxes. We can define the vertical profiles these two non-radiative energy flux perturbations, $\Delta\vec{F}^{(SH)}$ and $\Delta\vec{F}^{(LH)}$,

$$\Delta\vec{F}^{(LH)} = \begin{pmatrix} 0 \\ \vdots \\ 0 \\ -\Delta LH \end{pmatrix} \quad \text{and} \quad \Delta\vec{F}^{(SH)} = \begin{pmatrix} 0 \\ \vdots \\ 0 \\ -\Delta SH \end{pmatrix} \quad (4.16)$$

The negative sign in (4.16) is due to the fact that surface sensible and latent heat fluxes are defined as positive if they are upward. In other word, positive values of surface sensible and latent heat fluxes imply cooling to the surface. The difference between $\Delta(\bar{C}f + \bar{D})$ and $(\Delta\vec{F}^{(SH)} + \Delta\vec{F}^{(LH)})$ corresponds to the sum of the change in cloud forcing and the change in non-radiative energy fluxes due to changes in atmospheric convections and large-scale circulations, namely,

$$\Delta(\vec{C}f + \vec{D}^{atmos-dyn}) = \Delta(\bar{C}f + \bar{D}) - (\Delta\vec{F}^{(SH)} + \Delta\vec{F}^{(LH)}) \quad (4.17)$$

To calculate the partial temperature changes associated with each of these energy flux perturbations we compute the matrix $\left(\frac{\partial\bar{R}}{\partial\bar{T}}\right)$ referred to as the Planck feedback matrix. It represents the linearized longwave radiation changes due to changes in the atmosphere-surface column temperatures relative to the climatological temperature profile with climatological specific humidity, clouds and other atmospheric gases. It is written as:

$$\left(\frac{\partial\bar{R}}{\partial\bar{T}}\right) = \begin{pmatrix} \frac{\partial\bar{R}_1}{\partial\bar{T}_1} & \dots & \frac{\partial\bar{R}_1}{\partial\bar{T}_{M+1}} \\ \vdots & \ddots & \vdots \\ \frac{\partial\bar{R}_{M+1}}{\partial\bar{T}_1} & \dots & \frac{\partial\bar{R}_{M+1}}{\partial\bar{T}_{M+1}} \end{pmatrix} \quad (4.18)$$

The size of the matrix is the same as the number of vertical layer in the model. Note that $\left(\frac{\partial\bar{R}}{\partial\bar{T}}\right)$ varies with longitude and latitude as well as season (calendar month). Plotted in

Figure 4.2 is an example of $\left(\frac{\partial \bar{R}}{\partial \bar{T}}\right)$ taken at latitude 1S and longitude 187.75 (middle of the tropical Pacific Ocean) using January climatological vertical profiles derived from the control experiment.

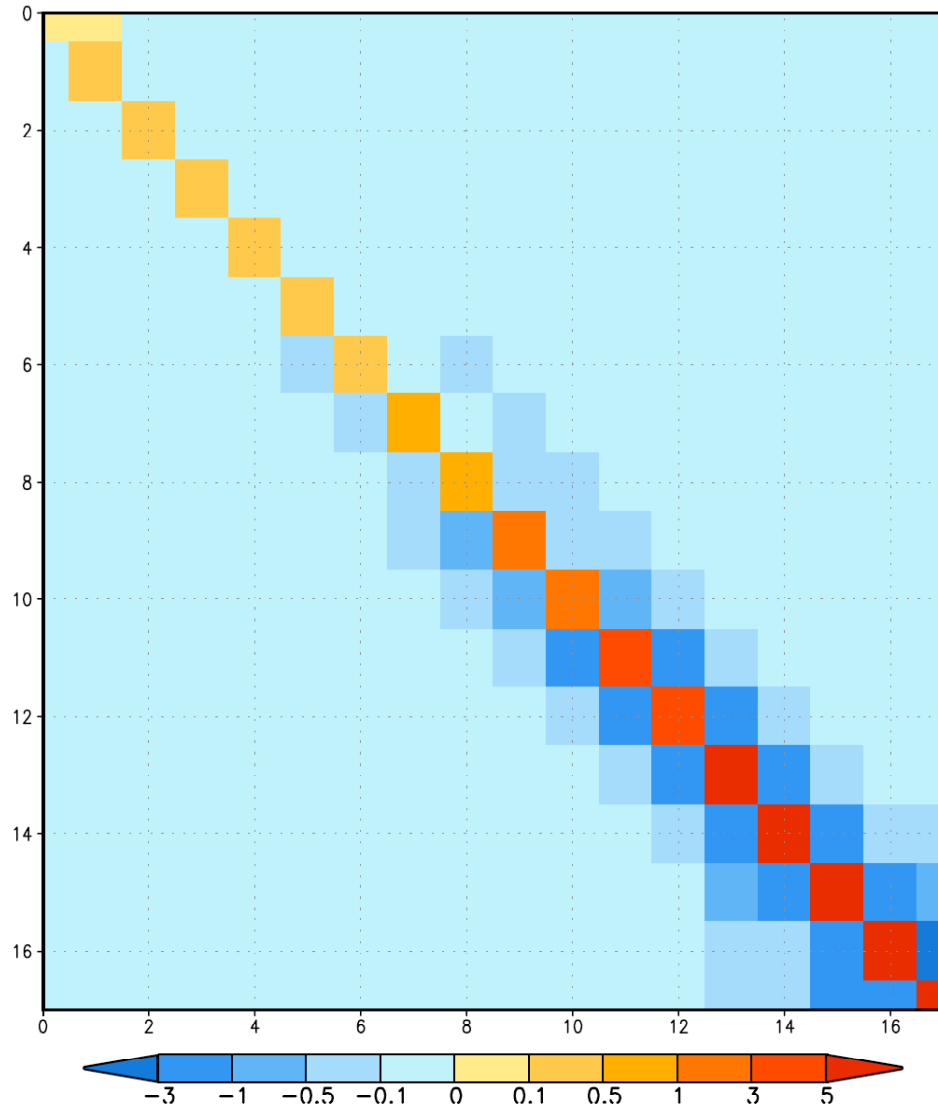


Figure 4.2: Example of the Planck feedback matrix. Each column represents the cooling rate change from the top layer to the surface layer due to a 1 K temperature increase from the equilibrium temperature profile (units: $\text{W m}^{-2} \text{K}^{-1}$).

The partial temperature perturbation due to each feedback agent and external forcing (x) can then be evaluated by:

$$\Delta\bar{T}^{(x)} = \left(\frac{\partial\bar{R}}{\partial\bar{T}}\right)^{-1} \Delta\bar{F}^{(x)} \quad (4.19)$$

Where $\left(\frac{\partial\bar{R}}{\partial\bar{T}}\right)^{-1}$ is the inverse of the Planck feedback matrix, $\Delta\bar{F}^{(x)}$ represents each of the energy flux perturbations in the right hand side of (4.11), which are defined in (4.12)-(4.17) and $\Delta\bar{T}^{(x)}$ is the vertical profile of the partial temperature perturbations whose infrared radiation perturbations balances the energy flux perturbations due to each feedback agent x at each atmospheric layer and at the surface. The total response to the external forcing imposed to the climate system (doubling of CO₂) is the sum of the partial temperature changes (Lu and Cai, 2008):

$$\Delta\bar{T}^{tot} = \sum_x \Delta\bar{T}^{(x)} = \Delta\bar{T}^{2CO_2} + \Delta\bar{T}^{h_2o} + \Delta\bar{T}^{\alpha} + \Delta\bar{T}^{(Cf+D)} \quad (4.20)$$

We will compare $\Delta\bar{T}^{tot}$ with the actual temperature changes derived from the global warming simulations made with the GFDL_CM2.

4.3 Method Validation

Let us first verify if the correction term to the clear-sky surface albedo feedback effectively removes the total surface albedo feedback under cloudy sky conditions from the (total) cloud forcing term, as indicated in (4.14) and (4.15) or (4.9). Because the correction is made only at the surface, we need to verify the result at the surface. At the surface, the change in non-radiative energy flux is only due to the surface sensible and latent heat fluxes. Therefore, (4.9) can be rewritten

$$(\Delta C_f)_{surface} = -\Delta(S - R)_{surface} + \Delta\alpha(S^{\downarrow,cld} - S^{\downarrow})_{surface}^{1CO_2} + \Delta SH + \Delta LH \quad (4.21)$$

The superscript “ 1CO_2 ” indicates that the term is evaluated using the output of the 1CO_2 climate simulations and “ Δ ” refers to the difference between the $2 \times \text{CO}_2$ and $1 \times \text{CO}_2$ climate states. Note that the first term on the RHS of (4.21) is taken from our offline clear-sky radiation calculations and the second term is from the GFDL outputs. All terms on the RHS of (4.21) have no direct information about changes in clouds. Based on the energy balance principle, the RHS should be indicative of change in cloud forcing. Because the archive of GFDL climate simulations include radiation fluxes at the surface (and at the TOA) for both clear sky and cloudy sky, we can evaluate the LHS of (4.21), the change in cloud forcing, directly from the archive of GFDL climate simulations, according to:

$$\begin{aligned} (\Delta Cf)_{\text{surface}} &= \Delta(S^{\downarrow,\text{cld}} - S^{\downarrow})_{\text{surface}} + \Delta(R^{\downarrow,\text{cld}} - R^{\downarrow})_{\text{surface}} - \Delta\alpha(S^{\downarrow,\text{cld}} - S^{\downarrow})_{\text{surface}}^{1\text{CO}_2} \quad (4.22) \\ &= (1 - a_{1\text{CO}_2})\Delta(S^{\downarrow,\text{cld}} - S^{\downarrow}) + \Delta(R^{\downarrow,\text{cld}} - R^{\downarrow})_{\text{surface}} \end{aligned}$$

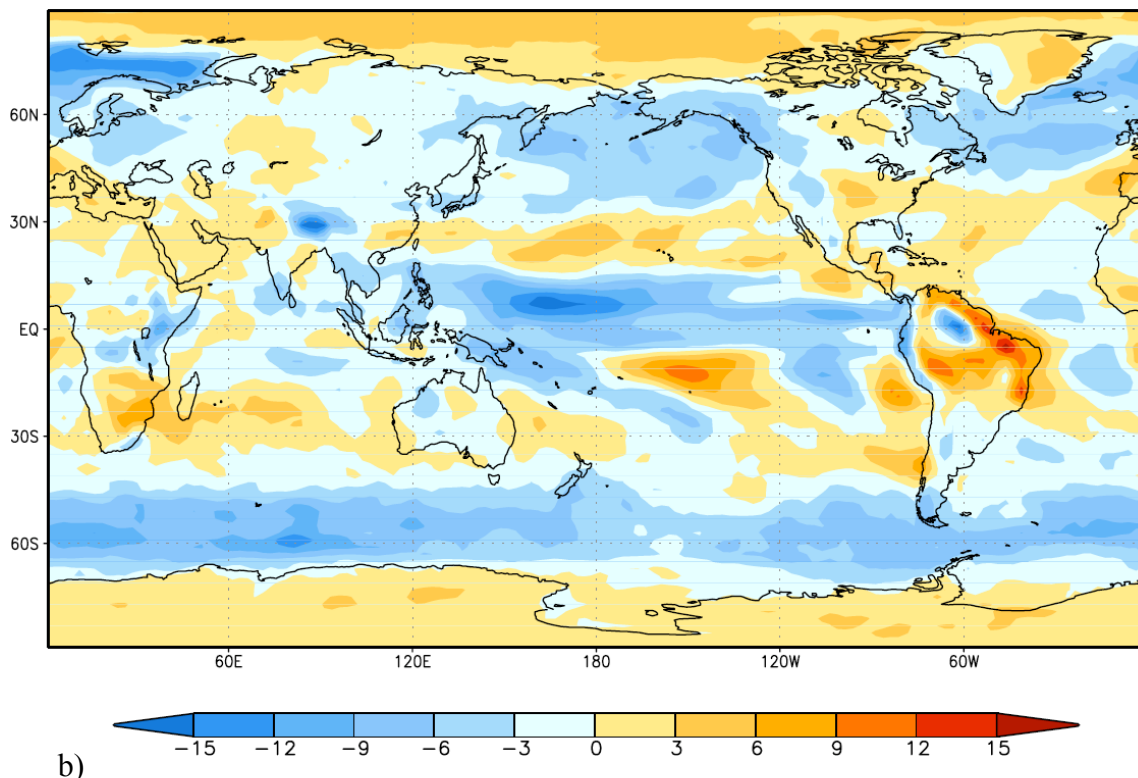
Shown in Figure 4.3a and 4.3b are the LHS and RHS of (4.21) respectively. The two calculations yield very similar geographic distribution and intensity. This implies two things: (i) the correction to the clear-sky albedo feedback calculations, namely, the term $-\Delta\alpha(S^{\downarrow,\text{cld}} - S^{\downarrow})_{\text{surface}}^{1\text{CO}_2}$, indeed removes the surface albedo feedback effects in cloud forcing, which in turns help to us isolate the total surface albedo feedback (see Eq. (4.14) above), and (ii) the method to infer the change in cloud forcing at the surface using the change in clear sky radiation at the surface and changes in the surface turbulent sensible and latent heat fluxes is feasible (e.g., RHS of Eq. (4.21) above).

It is seen that over the equatorial region, the change in cloud forcing is negative with a maximum over 15 W m^{-2} located in the western pacific. Positive changes in cloud forcing are encountered around subtropics in both hemispheres. Maximum values between 9 to 12 W m^{-2} are located over the mid-pacific. The Southern Ocean and the Northern hemisphere mid-latitudes display a negative change in cloud forcing along the storm track regions except for a narrow band of positive values around 60°S . Moreover, a positive change in cloud forcing occurs over both poles in Figure 4.3a but only over the South Pole in Figure 4.3b. The error in estimating cloud forcing using clear-sky radiation

and non-radiative energy terms (e.g., surface sensible and latent heat fluxes) over the North Pole could be due to (i) errors in our clear-sky radiation calculation in comparison with the original GFDL clear-sky radiation calculation and (ii) non-radiative energy terms that are not included in our cloud forcing calculation, such as energy loss/gain due to runoff and snow/ice melting. To confirm whether the errors are caused by the difference between the two clear sky radiation calculations, we re-evaluate all terms on the RHS of (4.21) using the output derived from the GFDL clear-sky radiation calculations (Figure 4.4). It is seen that the values over the North Pole remain negative, meaning that this discrepancy is caused by the missing terms. Due to the unavailability of the other non-radiative energy flux terms in the archive of the GFDL model outputs, we could not exactly reproduce the change of cloud forcing at surface based on the information from the clear sky radiation calculations and surface sensible and latent heat fluxes. Because these missing terms are relatively small except in the polar region, the change in cloud forcing at surface inferred from clear sky radiation is highly reliable over the most areas.

The global average of the change in cloud forcing at the surface is -1.59 W m^{-2} when calculated using GFDL's climate simulation archive with (4.22), -2.09 W m^{-2} using our offline clear-sky radiation calculations with (4.21), and -1.59 W m^{-2} using the original GFDL clear-sky radiation with (4.21). Moreover, when studying the differences of the change in surface cloud forcing between the various calculations over the annual cycle, the error arising from using our offline clear-sky radiation calculations instead of the original GFDL clear-sky radiation with (4.21) is larger than the error arising from using equation (4.21) as opposed to equation (4.22) in 8 months out of 12. Therefore differences between our clear-sky radiation calculations and the original GFDL clear-sky radiation are responsible for part of the differences between Figure 4.3a and 4.3b. In conclusion the correction term applied to the inferred change in cloud forcing at the surface yields results consistent with the independent calculation given in (4.22). More detailed discussions on the significance of the change in cloud forcing at the surface will be given in chapter 7.

a)



b)

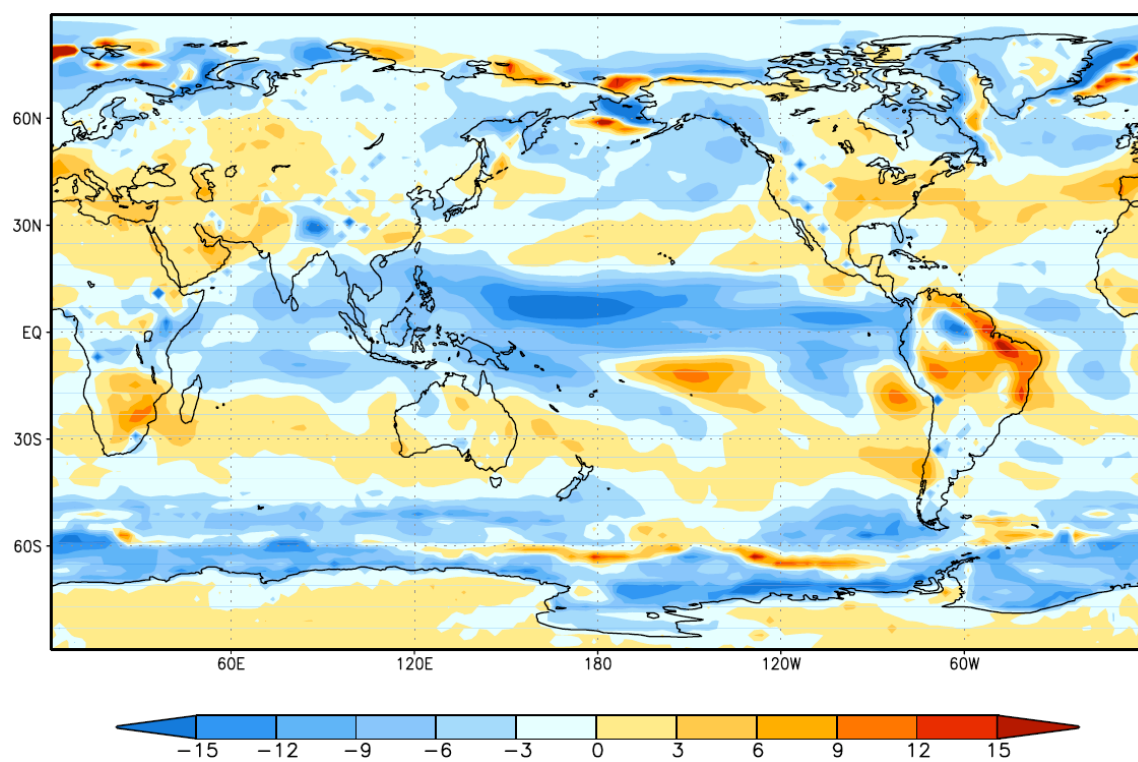


Figure 4.3: Change in cloud forcing at the surface, a) LHS of (4.21) or RHS of (4.22), b) RHS of (4.21) (unit W m^{-2}).

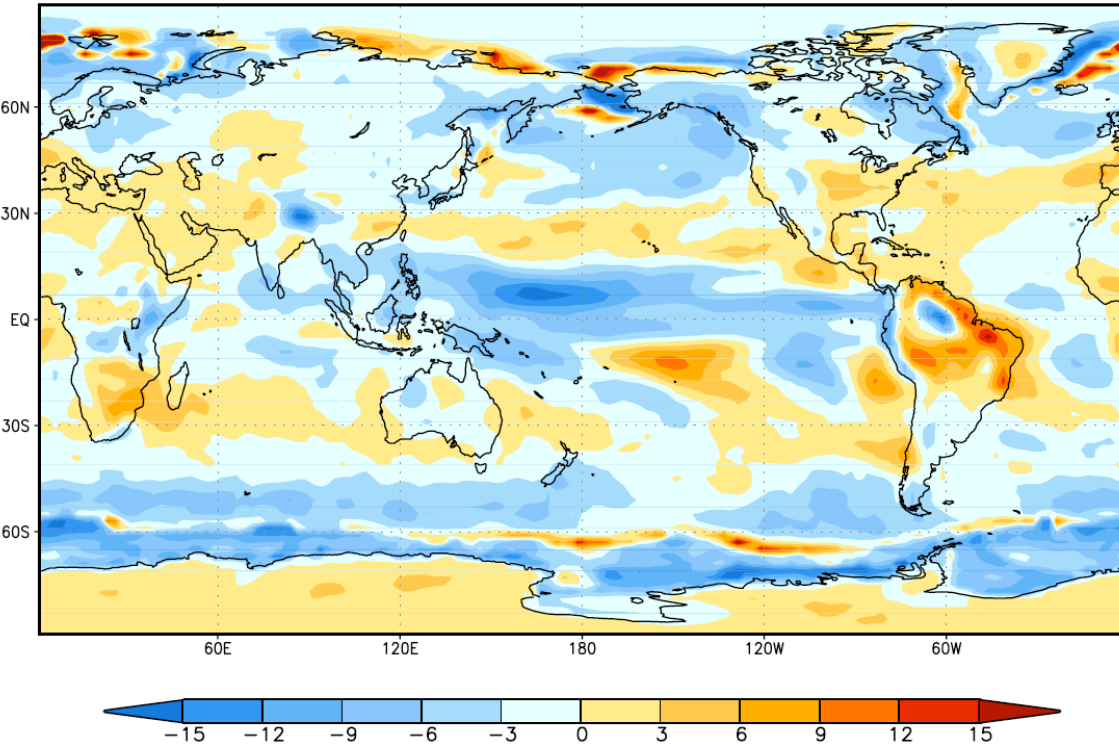


Figure 4.4: Change in cloud forcing at the surface using GFDL_CM2.0 clear sky surface radiation data for the terms in RHS of (4. 21) (unit W m^{-2}).

Feedback analysis can be ambiguous because of the time dependence and correlation between different feedback variables. For example the cryosphere feedbacks are strongly coupled to processes in the atmosphere such as polar cloud and radiation processes (Bony et al., 2006). Cloud cover is also associated with sea ice variability and changes in atmospheric boundary layer and surface energy fluxes (Schweiger et al., 2008), but also cloud radiative forcing affects poleward heat transport (Weaver, 2003). It is therefore important to note that our goal is not to determine how each feedback interact with one another in a non linear sense, but to quantify the post process temperature changes due to each feedback and the radiative forcing. Nonetheless, the non-linear terms have been neglected in the linearization process of the total energy flux perturbation into partial energy flux perturbations due to changes in CO_2 , surface albedo, water vapor, and temperature (4. 20). It is therefore important to determine the amplitude of the higher order terms of each feedback and forcing and the interaction among them. This can be achieved by verifying the accuracy of decomposing the total change in clear sky radiation

into the sum of the clear sky energy flux perturbations due to the change in CO₂, water vapor, albedo, and total temperature change

$$\Delta(\vec{S} - \vec{R}) = \Delta^{(CO_2)}(\vec{S} - \vec{R}) + \Delta^{(h_2o)}(\vec{S} - \vec{R}) + \Delta^{(\alpha)}\vec{S} - \frac{\partial \vec{R}}{\partial \vec{T}}\Delta T \quad (4.23)$$

The left hand side of (4.23) is determined by computing the total change in clear sky radiation under 2 × CO₂ forcing using our radiation transfer model ran using the 2 × CO₂ and the control climate data and taking the difference:

$$\Delta(\vec{S} - \vec{R}) = \left((\vec{S} - \vec{R}) \Big|_{T_{2CO_2}, q_{2CO_2}, \alpha_{2CO_2}, 2CO_2} - (\vec{S} - \vec{R}) \Big|_{T_{1CO_2}, q_{1CO_2}, \alpha_{1CO_2}, 1CO_2} \right) \quad (4.24)$$

The right hand side is computed as the sum of the radiative energy flux perturbations due to the forcing and feedbacks and due to the total temperature change throughout the entire atmosphere-surface column $-\frac{\partial \vec{R}}{\partial \vec{T}}\Delta T$. The temperature change is calculated using the GFDL_CM2.0 model's temperature output from the 2 × CO₂ and the control climate simulations: $\Delta T = T(2CO_2) - T(1CO_2)$.

The results are plotted as a time and zonal average in the atmosphere (Figure 4.5a) and as a time average at the surface (Figure 4.5b). The LHS of (4.23) is represented by color shadings and the sum of the RHS of (4.31) is represented by contours. The total clear-sky energy flux perturbation is represented in the atmosphere and at the surface. It shows a maximum energy flux perturbation of 2 W m⁻² over the equator between 700 hPa and 600 hPa and two secondary maxima over the mid-latitudes between 900 hPa and 700 hPa (Figure 4.5a). The minimum value (3 W m⁻²) is reached over the tropics in the upper troposphere at around 400 hPa. At the surface the positive energy flux perturbation of 8 W m⁻² over the tropical oceans occurs as well as negative energy flux perturbation over mid latitude continents (Figure 4.5b). Overall, the linearization process or the exclusion of higher order terms appears to be a good approximation to the total clear sky energy flux perturbation. The annual cycle of the sum of the radiative energy flux perturbations due to the forcing and feedbacks and due to the total temperature change (not shown here) also matches the annual cycle of the total clear sky energy flux perturbation. It is understood that errors induced by the elimination of the higher order terms could be canceling out each other but their amplitudes are believed to be small compared to the

energy flux perturbations themselves. We here conclude that the partial energy flux perturbations do add up to the total change in clear sky energy flux perturbation with a good degree of accuracy.

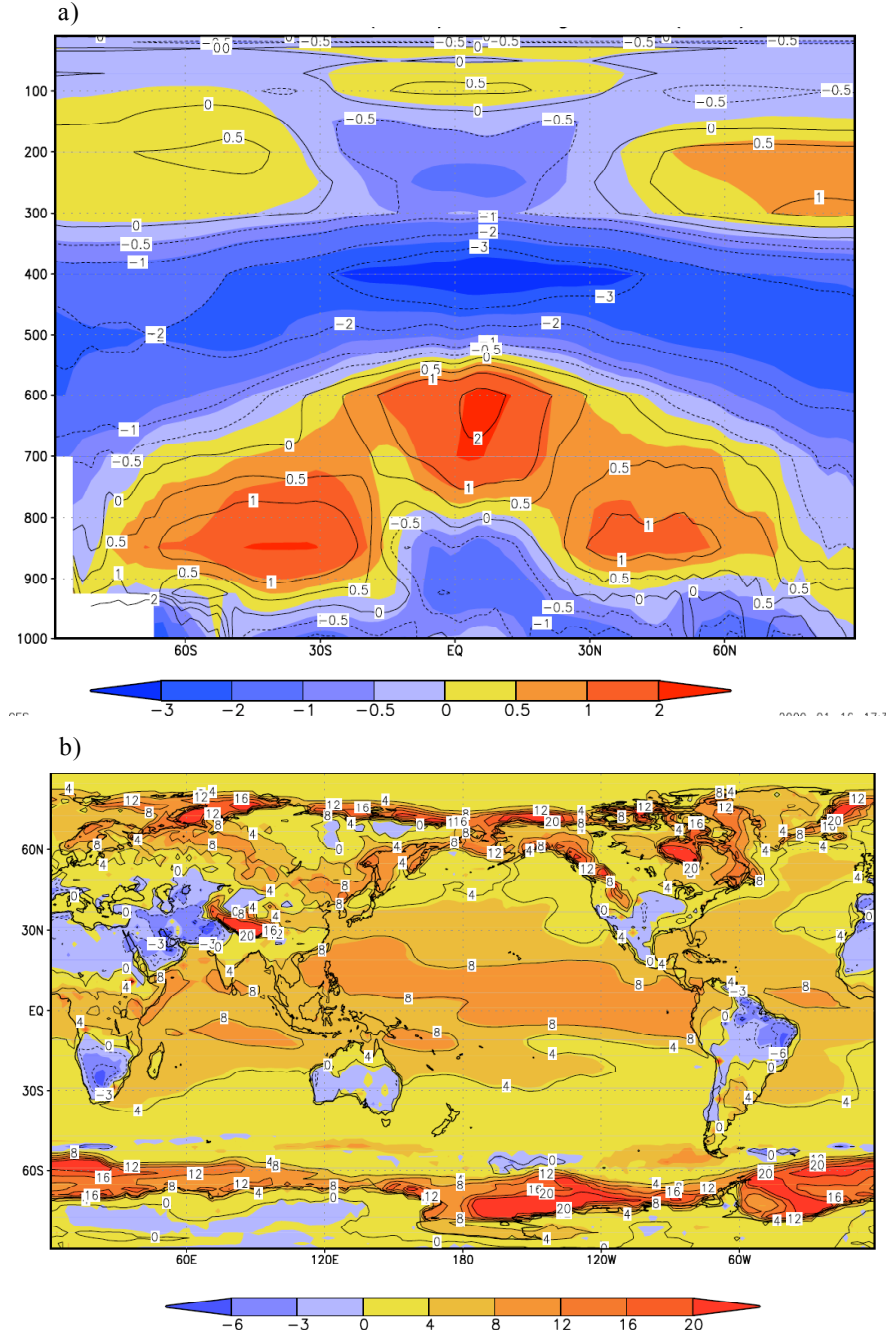


Figure 4.5: $\Delta(\text{S-R})$ color shadings and sum of the RHS of (4.23) contours. a) Zonal and time mean in the atmosphere (units: W m^{-2}), b) time mean at the surface (units: W m^{-2}).

CHAPTER 5

EVALUATION OF MODEL CLIMATOLOGY

This chapter evaluates the control climate simulation of the GFDL_CM2.0 model. This can give us an insight on the reliability of the model's climate change simulation under $2 \times \text{CO}_2$ radiative forcing because the climate system response depends on its basic state. It is therefore important to evaluate the GFDL_CM2.0 model according to its ability to simulate present-day conditions. As noted by Pincus et al. (2008) and Gleckler et al. (2008) there are no universally accepted climate metrics or objective method to define AOGCM skills in reproducing observed climate. For this study it is important to evaluate the model energy and water balance, and test fields that respond to changes in radiative forcing. These fields include solar and infrared radiations at the TOA and at the surface, turbulent heat fluxes, temperature, sea level pressure and atmospheric specific humidity.

The control slab ocean simulation was initiated with forcing agents that generally are consistent with year 1990 or late 20th century conditions and are important to simulate current climate. The forcing agents include the well-mixed greenhouse gases (carbon dioxide, methane, and nitrous oxide), tropospheric and stratospheric ozone, tropospheric sulfates, black and organic carbon, dust, sea salt, solar irradiance, and the distribution of land cover types. The direct effect of tropospheric aerosols is calculated by the model, but the indirect effects are omitted by having no direct interaction with the cloud scheme. Details of the GFDL_CM2.0 model characteristics are described in Appendix A. The simulation outputs for solar, infrared, and turbulent heat fluxes are compared to globally averaged fields computed in previous studies using satellite climatologies from CERES and ERBE. The remaining fields are compared to the NCEP-NCAR reanalysis (Kalnay et al., 1996). Since the forcing agents applied to the GFDL_CM2.0 model are consistent with the late 20th century conditions, the NCEP-NCAR reanalysis was averaged over the last decade of the 20th century (from the years 1989 to 2001). Seasonal averages are considered for the winter [December-February]

(DJF)], spring [March-May (MAM)], summer [June-August (JJA)], and fall [September-November (SON)]. Some differences in the comparison can arise from the fact that the climate model is initiated with late 20th century forcing which cannot be directly compared to a specific time range in the reanalysis, and both GFDL_CM2.0 and reanalysis are subject to different postprocessing to interpolate data into pressure levels.

5.1 Global energy and water mass balance

The TOA energy budget should reach equilibrium when averaged over a long period of time. The energy balance between solar and longwave radiations in AOGCMs is a basic requirement to simulate the energy content of the planet. The GFDL_CM2.0's long-time global average of the radiation flux at the TOA in the control simulation is 1.49 W.m⁻². This is relatively small compared to the values of the meridional profile of the net TOA energy flux varying from -120 in the poles to 70 W.m⁻² in the tropics. Nevertheless, the non-perfect balance of the net radiation flux at the TOA suggests that either the model hasn't reach its equilibrium states yet or the model energy is not in balance due to spurious sinks/sources of energy in the models. The heat storage term due to the fact that the model has not reached its equilibrium state has been included in our feedback analysis as an extra energy source/sink term at the surface, which is part of the "missing term" Figures. 7.7e and 7.7f, although this term is smaller than other terms. The same calculation using the 2×CO₂ climate simulations reveals similar results, with values of 1.55 W.m⁻². This suggests that the 2 × CO₂ climate simulations are as close to reaching their equilibrium states as the control runs as far as the global averaging is concerned.

Because the redistribution of water vapor associated with water vapor fluxes by atmospheric motion cannot introduce a sink/source of the water mass in the atmosphere, and the changes in atmospheric water vapor storage are very small for long time averaging, the global mean of the difference between evaporation and precipitation fluxes has to be zero. The global mean evaporation is indeed very close to the global mean precipitation in the GFDL_CM2.0 slab ocean model with the residuals, in terms of latent heat flux, equal to 0.17 Wm⁻² for the control simulation and 0.13W.m⁻² for the 2 × CO₂

simulation. This suggests that both climate simulations reach their equilibrium states (within 0.04 W.m^{-2} in terms of latent heat flux) as far as the global hydrological cycle balance is concerned.

5.2 Solar and infrared radiations

The fields selected for this evaluation are the solar and infrared radiations at the surface and the TOA, which are averaged over the 13-year control simulation, and the global average is calculated and compared with observations. Pincus et al. (2008) evaluated physical parameters such as TOA radiative fluxes in the IPCC AR4 climate models' 20th century simulation. The GFDL_CM2.0 model net flux at the TOA was found to agree well with satellite climatologies from CERES and ERBE. Wild et al. (2006) evaluated clear-sky solar fluxes in IPCC AR4 climate models' 20th century simulation and found that at the surface the GFDL_CM2.0 coupled model simulates the long-term annual mean of clear-sky insolation is in agreement with the clear-sky climatology at 17 observation locations.

We compare the full sky TOA radiation of the GFDL_CM2.0 slab ocean control climate simulation to various estimates provided by Wild and Roeckner (2006) from ERBE and ISCCP. The globally averaged absorbed solar radiation at the TOA (incident minus reflected) is 237 W m^{-2} in the GFDL_CM2.0 simulation, which is within the ERBE and ISCCP estimates of 240 W m^{-2} and 236 W m^{-2} . The globally averaged longwave radiation in the GFDL_CM2.0 simulation is 235.5 W m^{-2} , again extremely close to the ERBE and ISCCP values of 234 W m^{-2} and 233 W m^{-2} . The GFDL_CM2.0 model 20th century climate simulation has been evaluated (Delworth et al., 2006), and the absorbed shortwave at the TOA shows a positive bias in the high latitudes of the southern hemisphere and a negative bias over the midlatitudes of the northern hemisphere and subtropical southern hemisphere ocean compared to ERBE data. The degree of accuracy of these radiation calculations, as discussed in GFDL GAMDT (2004), is due to the fact that the TOA radiation budget is tuned to match the radiation budget available from satellite data, but at the surface the model radiation budget is rather independent.

At surface we compare the globally averaged net solar and longwave radiation in the GFDL_CM2.0 simulation with observations from GEWEX (Global Energy and Water Experiment) and GISS (Goddard Institute for Space Studies) described in GFDL GAMDT (2004) in their evaluation of the GFDL model. The GFDL_CM2.0 net solar radiation at the surface is equal to 160.3 W m^{-2} , and for the GEWEX and GISS observations equal to 164.6 W m^{-2} and 165.2 W m^{-2} . The GFDL_CM2.0 net longwave radiation at the surface is equal to -57.62 W m^{-2} , and for the GEWEX and GISS observations equal to -47.1 W m^{-2} and -50.9 W m^{-2} . These results are similar to the ones found in GFDL GAMDT (2004), with the GFDL_CM2.0 underestimating the net shortwave radiation by 4 to 5 W m^{-2} and overestimating the net longwave radiation by up to 10 W m^{-2} .

5.3 Surface turbulent heat fluxes

Surface fluxes are computed using Monin-Obukhov similarity theory, given the model's lowest level wind, temperature, and humidity, and the surface roughness lengths (GFDL GAMDT, 2004). The errors in net solar and longwave radiation at the surface, such as the overestimate of surface absorption of solar radiation and the uncertainties in downwelling longwave as seen in section 5.2, lead to uncertainties in sensible and latent heat flux estimates. A study of the Earth annual global mean energy budget by Kiehl and Trenberth (1997) estimated the latent heat flux from monthly mean global precipitation rates from the Global Precipitation Climatology Project to be 78 W m^{-2} and the sensible heat flux computed as a residual from the global energy balance at the surface is 24 W m^{-2} . Surface turbulent heat fluxes determined from a bulk formula by Sellers (1965) found the globally averaged latent and sensible heat flux to be 78 W m^{-2} and 18 W m^{-2} .

The GFDL_CM2.0 globally averaged latent heat flux is 81.9 W m^{-2} and sensible heat flux 18.7 W m^{-2} . The sensible heat flux is very similar to the one computed by Sellers (1965), but the GFDL_CM2.0 overestimates the latent heat flux by 4 W m^{-2} and underestimates the sensible heat flux by 5 W m^{-2} compared to the Kiehl and Trenberth (1997) estimates. This is consistent with the results (GFDL GAMDT, 2004) where the

GFDL model overestimates latent heat flux and underestimates sensible heat flux by a similar amount.

5.4 Temperature

In order to simulate the temperature field correctly, the GFDL_CM2.0 must represent a variety of processes with accuracy such as the distribution of insolation, clouds, surface heat fluxes, transport of energy by the atmosphere (Randall et al., 2007). The GFDL_CM2.0 coupled model forced with time-varying natural and anthropogenic agents (between 1861 and 2000) was analyzed by Knutson et al. (2006). It was concluded that the global mean temperature evolution and regional trends were reasonably well simulated. Over regional scales, too little warming was found over northern Asia, Canada, and southern Indian Ocean and too much warming over southeastern United States compared to HadCRUT2v observations. Chapman and Walsh (2007) also studied the Arctic temperature in the IPCC_AR4 coupled models' 20th century climate simulations. They found the GFDL_CM2.0 to be colder than the ECMWF ERA-40 reanalysis in winter and spring over the Barents Sea due to a larger sea ice extent in the model.

Figure 5.1 shows the seasonal cycle of the difference between the GFDL_CM2.0 slab ocean control simulation and the NCEP_NCAR reanalysis. The GFDL_CM2.0 model accounts for large fraction of the seasonal temperature pattern as depicted by the large portion of white shading over the oceans, representing a temperature bias of less than 0.5°C. The positive (negative) biases indicate regions of warmer (colder) temperatures in the GFDL_CM2.0 model compared to the NCEP-NCAR reanalysis. The position of the zero degree line is equatorward in the GFDL_CM2.0 model (red dotted line) especially over the northern hemisphere and during the boreal summer compared to the reanalysis (blue line), but almost at the same location over the southern hemisphere. This means that colder temperatures are present in the GFDL_CM2.0 model's high

latitudes in particular over the northern hemisphere. A persistent negative (cold) bias throughout the seasonal cycle is present over high latitudes (north of 60°) and northern hemisphere continents. A cold bias is found over the Barents Sea in winter and spring as pointed out by Chapman and Walsh (2007). Larger temperature differences over Polar Regions are also found in most IPCC AR4 models (Randall et al., 2007). Those data poor regions are especially hard to model. The cold bias is the largest over Northern Asia boreal winter reaching values over -6°C, and a warm bias is present over the southeastern part of the United States in summer reaching values of 6°C similarly to Knutson et al. (2006) study. In the Austral fall and winter, the bias is positive over South America and part of Antarctica indicating that the GFDL_CM2.0 model simulates surface temperatures that are warmer by 2 to 8°C than the reanalysis. As explained in Knutson et al. (2006), these discrepancies could be due for instance to errors in forcing agents or simulated response to forcing agent (e.g. omissions of indirect aerosol forcing), or errors in observed temperature data. Errors in atmospheric circulation could also be a factor.

Nevertheless the value of the spatial correlation in all seasons is 0.99, and the mean absolute error varies between 0.93°C in the boreal fall and 1.12°C in the boreal winter, which indicates an overall good agreement between the GFDL_CM2.0 and NCEP-NCAR reanalysis except over mid to high latitudes continents. This means that major processes governing surface temperature are probably represented reasonably well over large part of the globe in the GFDL_CM2.0 slab ocean model and can therefore be trusted to respond accurately to radiative forcing.

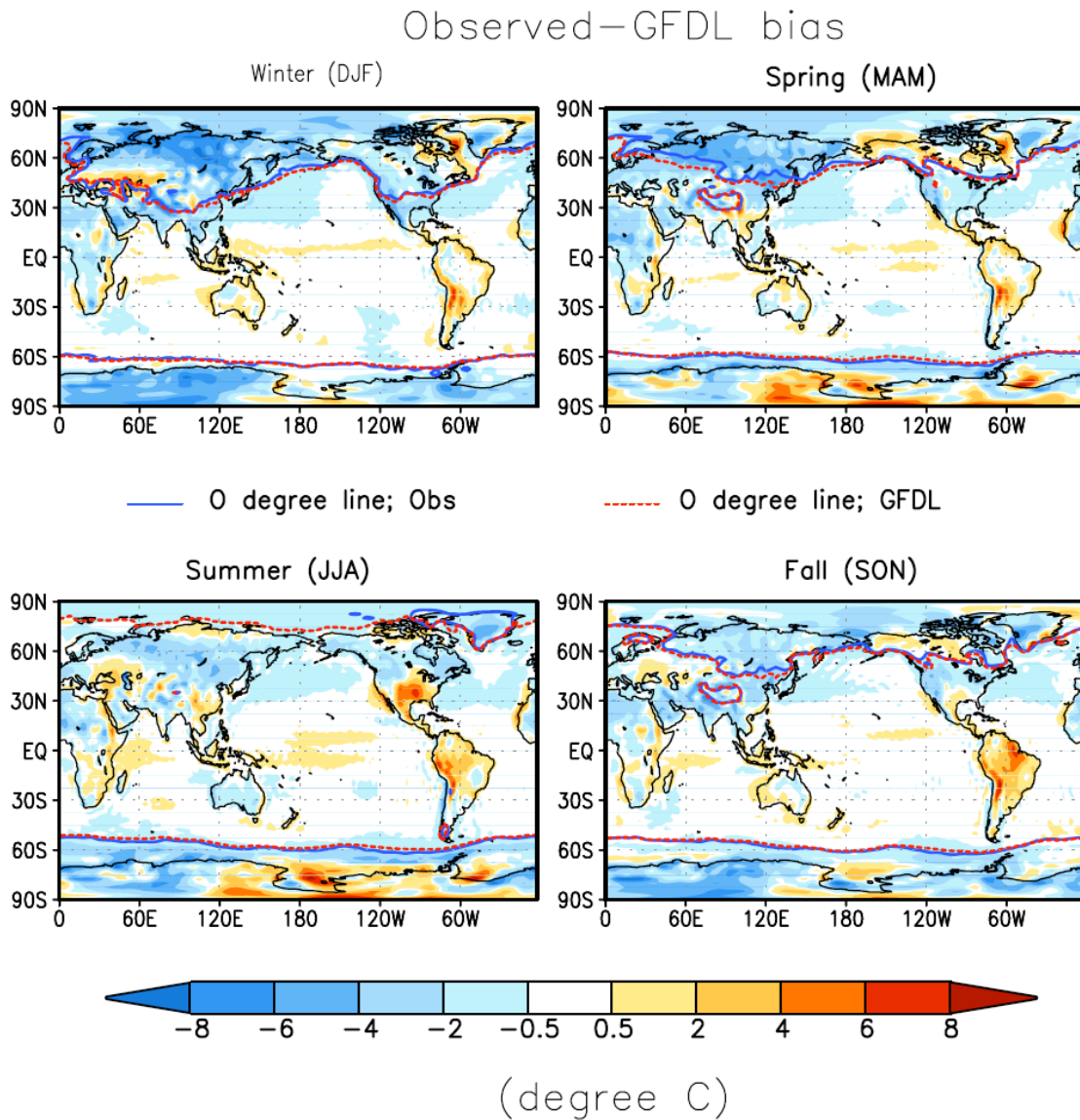


Figure 5.1: Time mean of the surface temperature difference between GFDL_CM2.0 model and NCEP-NCAR reanalysis (degree C). Zero degree line for NCEP-NCAR (blue) and GFDL_CM2.0 (red).

Analyzing the simulated atmospheric temperature pattern gives us an insight on how well radiative transfer is parameterized and heat transport is simulated. The GFDL GAMDT (2004) tested the atmospheric and land model components of the GFDL_CM2.0 model with prescribed sea surface temperatures. The largest model atmospheric temperature bias occurred at high latitudes between 100 and 500 hPa over the southern hemisphere. Randall et al. (2007) also found that the IPCC AR4 AOGCMs' 20th century

climate simulations including natural and anthropogenic forcing displayed a cold bias in the zonal mean atmospheric temperature near tropopause over high latitudes. They stated that the impact of this bias on the model's response to radiative forcing should be small relative to other uncertainties.

Figure 5.2 depicts the zonal and time mean of GFDL_CM2.0 model (red line) and the NCEP-NCAR reanalysis (blue line) atmospheric temperature. Again, the reanalysis is averaged over the year 1989 to 2001 to match the late 20th century forcing applied to the GFDL_CM2.0 control simulation. The contours are plotted at 10°C intervals. The overall temperature pattern in both data sets show the largest temperature (above 25°C) over the equatorial region with the maximum values located over each hemisphere summer season following the insolation pattern. The lowest temperatures are close to the surface at the poles and close to the tropopause over low latitudes. At the lowest atmospheric level, similarly to the surface, the zero-degree contour line is equatorward in the GFDL_CM2.0 model compared to the NCEP-NCAR reanalysis over the northern hemisphere spring and summer signifying a cold bias, and almost the same over the southern hemisphere. Over all seasons the GFDL_CM2.0 model shows a cold bias in the troposphere except over the southern hemisphere high latitudes from the lowest level to about 600 hPa. The cold bias is the largest around 300 hPa at high latitudes, especially during the boreal winter and spring. The GFDL_CM2.0 model shows a warm bias in the stratosphere over 100 hPa. This is in agreement with previous studies (GFDL GAMDT, 2004; Randall et al., 2007). Overall the biases present in the atmospheric temperature are not believed to be significant enough to affect the model's response to radiative forcing.

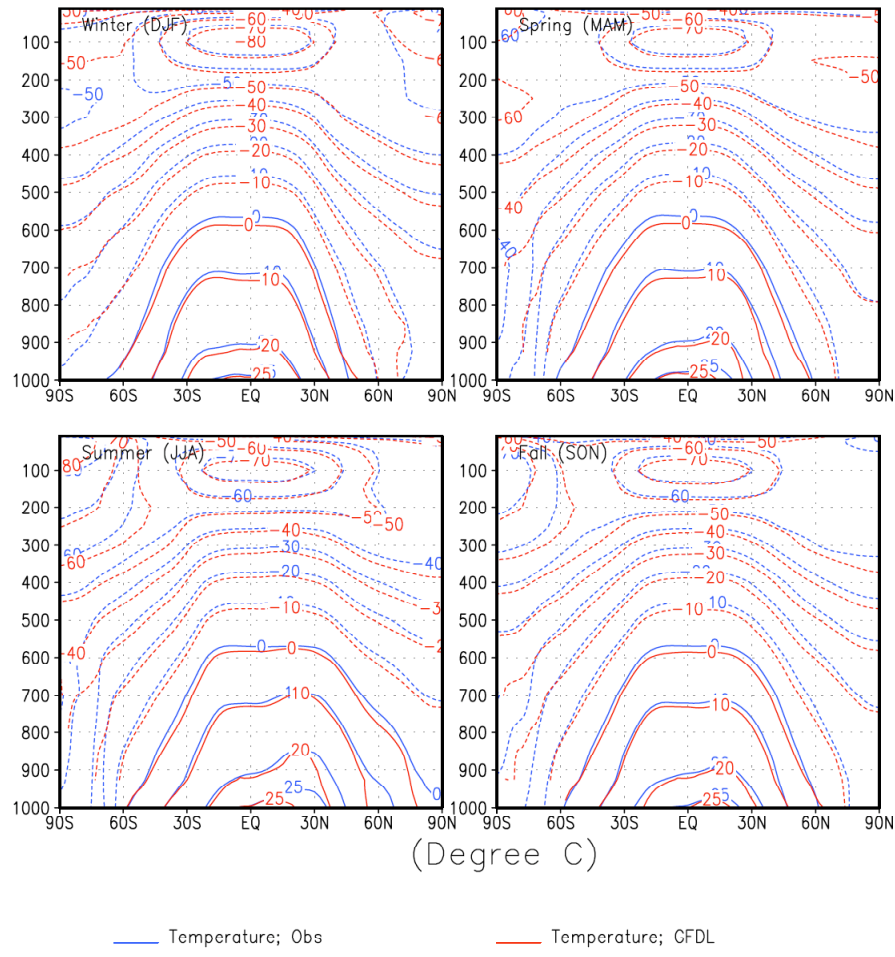


Figure 5.2: Modeled (red) and observed (blue) zonal and time mean of the atmospheric temperature. (Units degree Celsius).

5.5 Tropospheric Specific Humidity

The specific humidity is a measure of the ratio of the mass of water vapor (in g) over the total mass of air (in kg). Its accuracy is a measure of how well the evaporation, precipitation and moisture transports are simulated in climate models. It is an important field to evaluate because water vapor is an important greenhouse gas and its distribution affects outgoing longwave radiation, which in turns changes the earth radiative balance. The GFDL GAMDT (2004) evaluated the water vapor in the atmospheric and land model components of the GFDL_CM2.0 model with prescribed sea surface temperatures. They

found a moist bias in the relative humidity in the upper part of the troposphere (200-500 hPa), and a lower amount of integrated water vapor in the lower troposphere.

Figure 5. 4 displays the zonal and time mean of GFDL_CM2.0 model (red line) and the NCEP-NCAR reanalysis (blue line) tropospheric specific humidity. The overall seasonal specific humidity pattern is respected. Both data sets show the larger specific humidity (16 g kg^{-1}) at the lower level above the equator. It is associated with the position of the intertropical convergence zone and migrates northward from winter to summer crossing the equator. It reaches its largest concentration at any level over the summer hemisphere. The water vapor amount decreases rapidly towards the poles and with height to values of 0.5 g kg^{-1} at the lowest level over high latitudes in the winter hemisphere and at 300 hPa over the equator. Over low latitudes ($15^{\circ}\text{S}-15^{\circ}\text{N}$) the GFDL_CM2.0 overestimates the specific humidity from the surface to about 500 hPa, and underestimates the specific humidity above that level, as opposed to the results found in the GFDL GAMDT (2004) research. This might be because the comparison involves observations from satellites measurements that might differ from the reanalysis used here. Over the subtropics at low levels poleward at higher levels the GFDL_CM2.0 underestimates the specific humidity compared to the reanalysis. John and Soden (2006) plotted the specific humidity response to a warming climate with respect to the temperature response at different atmospheric levels and concluded that the specific humidity biases in the IPCC AR4 models have little impact on the specific humidity response to global warming. Therefore these differences are not believed to be large enough to have a significant impact on the change in water vapor under radiative forcing.

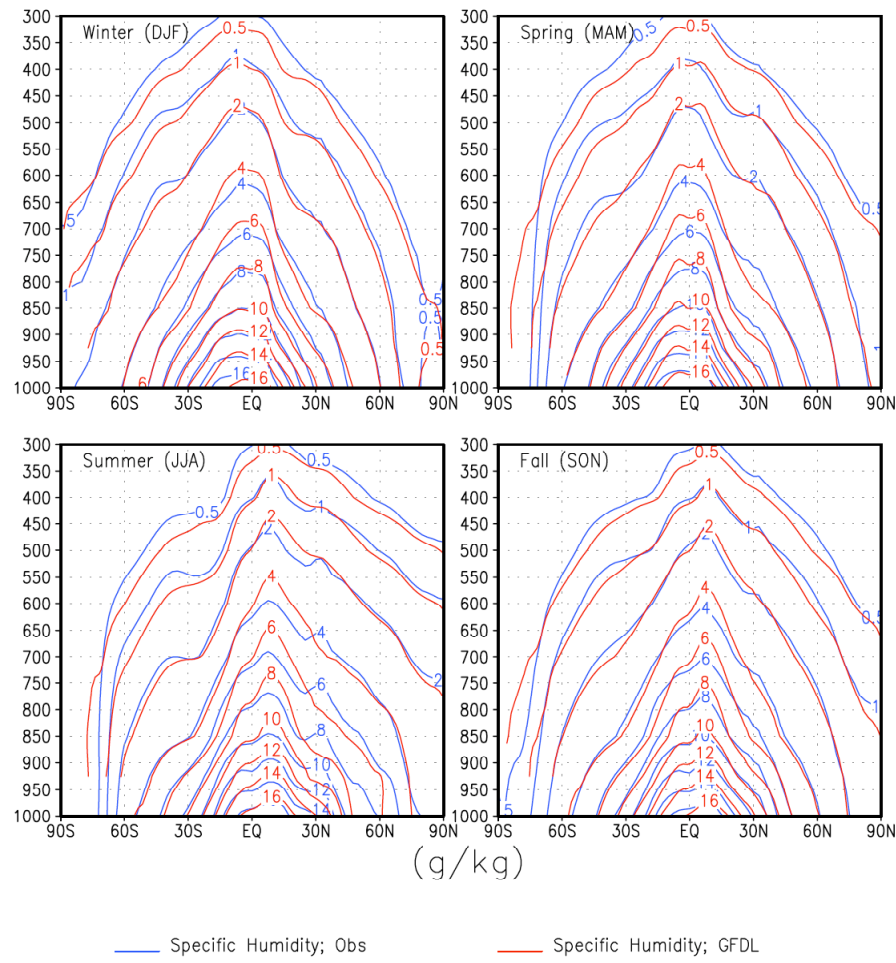


Figure 5.3: Modeled (red) and observed (blue) zonal and time mean of the atmospheric specific humidity. (Units g kg^{-1}).

CHAPTER 6

ENERGY FLUX PERTURBATIONS AT THE TOP OF THE ATMOSPHERE

Radiative energy flux perturbations at the TOA measure perturbations in energy inputs/outputs to/from the entire atmosphere-surface column. The PRP method solely deals with radiative energy flux perturbations at the TOA (see chapters 2.2.1 and 2.2.3). The CFRAM considers the vertical profiles of energy flux convergence perturbations. The vertical integrations of the vertical distribution of radiative energy flux convergence perturbations, by definition, are the radiative energy flux perturbations at the TOA. In this chapter, we examine radiative energy flux perturbations due to the doubling of CO₂, and changes in water vapor, and surface albedo. We also examine the changes in the sum of cloud forcing and large-scale dynamics inferred from the net clear-sky radiation flux at the TOA. In addition, CFRAM enables us to calculate the change in non-radiative energy fluxes due to the increase in horizontal atmospheric transport of total energy at the TOA (the slab ocean heat transport is kept constant). A positive (negative) value of perturbations in the net radiative energy flux at the TOA at a specific location indicates a net increase (decrease) in energy input into or a net decrease (increase) in energy output from the column below at that location, implying an energy source (sink) that contributes warming (cooling) in the column below. Each energy flux perturbation is averaged over time, and represents the net change in radiation convergence in the atmosphere/surface bellow.

6.1 Radiative forcing due to the doubling of CO₂

Carbon dioxide concentration has increased in the atmosphere at a current rate of 1.4 ppm yr⁻¹ from 1960 to 2005 (Forster et al., 2007), it is well mixed in the atmosphere and therefore is considered to be uniformly distributed throughout the atmosphere.

Carbon dioxide is a linear symmetric molecule with two major vibration-rotation bands in the infrared, the most relevant being centered at $15\text{ }\mu\text{m}$, close to the maxima of the Planck emission function for the Earth's surface temperature. This property enhances the infrared radiation absorption in the atmosphere, and makes CO₂ an important climate forcing agent (Petty, 2006). The external radiative forcing is the induced change in the Earth radiative balance at the TOA due to the doubling of CO₂ (from 352 ppmv to 704 ppmv in the GFDL_CM2.0 IPCC AR4 climate simulations). It is computed as the change in radiative energy flux divergence using (4. 12). This is accomplished by running the radiation transfer model once with a control climate fields and once with a doubling of the CO₂ concentration only, and taking the difference between the radiative energy fluxes in the two states. Figure 6.1 represents the time average of the net downward radiative forcing at the TOA due to the doubling of CO₂. The global average value of the external forcing at the TOA is 3.1 W m^{-2} , and 4.95 W m^{-2} at the tropopause taken to be at 200 hPa. Smaller value of the external radiative forcing at the TOA than that at the tropopause level reflects the fact that an increase in CO₂ causes stratospheric cooling (about -1.86 W m^{-2}). In a previous study by Randall et al. (2007) using the GFDL_CM2.0 model, the radiative forcing at the tropopause for the doubling of CO₂, after stratospheric adjustment, was reported to be 3.5 W m^{-2} for the GFDL_CM2.0 model. The stratospheric adjustment only allows the stratospheric temperature to reach a new equilibrium temperature that balances with the external radiative cooling rate in the stratosphere. As a result, the adjustment would yield a somewhat smaller radiative forcing at the tropopause because the stratospheric cooling effects of the external forcing have already been taken into consideration. Note that our external radiative forcing is done without considering climatological mean cloud field and without stratospheric adjustment. As pointed out by Forster and Taylor (2006), the external radiative forcing at the TOA is about 4.9 W m^{-2} without stratospheric adjustment and under clear-sky conditions.

The geographical distribution of the external radiative forcing at the TOA shows an overall positive sign (Figure 6.1). This indicates that the atmosphere is trapping more radiative energy when CO₂ is doubled than in its unperturbed state. Radiative forcing larger than 3 W m^{-2} is located over low latitudes between 45°N and 45°S . The larger energy flux perturbations are over the subtropical oceans. The strength of the external

radiative forcing at the TOA decreases toward higher latitudes. This follows loosely the distribution of the climatological longwave radiation emissions at the surface. Since the Earth's surface radiates more longwave radiations over low latitudes due to the larger temperatures (Stefan-Boltzmann law), the doubling of CO₂ will induce a larger positive forcing in the lower latitudes by trapping more longwave radiation. The external forcing tends to be smaller over the western equatorial pacific warm pool, with values between 2 and 2.5 W m⁻². This location corresponds to large atmospheric water vapor concentration; evident from the large vertically integrated specific humidity (Figure 6.2). The large water vapor concentration, which is a strong infrared radiation absorber, limits the effect of the increase in CO₂. Negative values of net downward radiative forcing are found at the TOA over Antarctica. An increase in atmospheric CO₂ concentration causes cooling in the stratosphere. Over higher latitudes, the tropopause is lower, and therefore the stratospheric cooling rate due to the doubling of CO₂ is also larger. Also the surface temperature over Antarctica is much colder, implying a much weaker radiative energy trapping by the increase of CO₂. The combination of these two effects could explain the negative values of the external radiative forcing at the TOA over Antarctica. The vertical distribution of the forcing will be discussed in the next chapter.

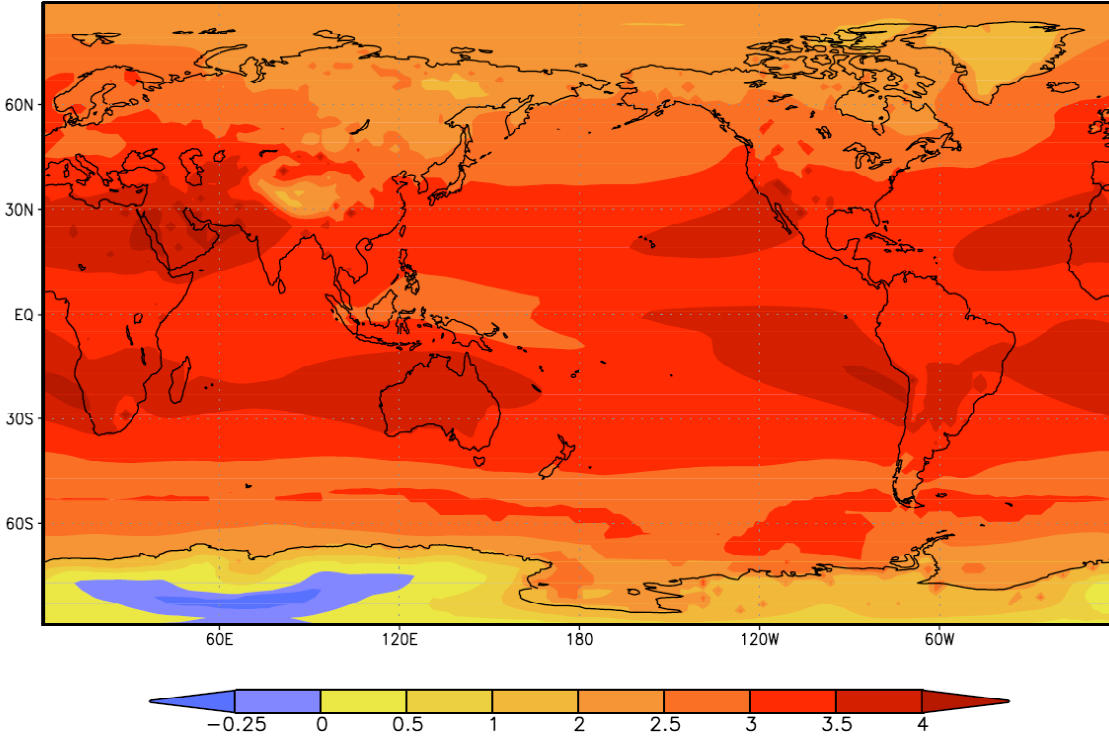


Figure 6.1: Time average of the external radiative forcing calculated at the TOA (unit: W m^{-2}).

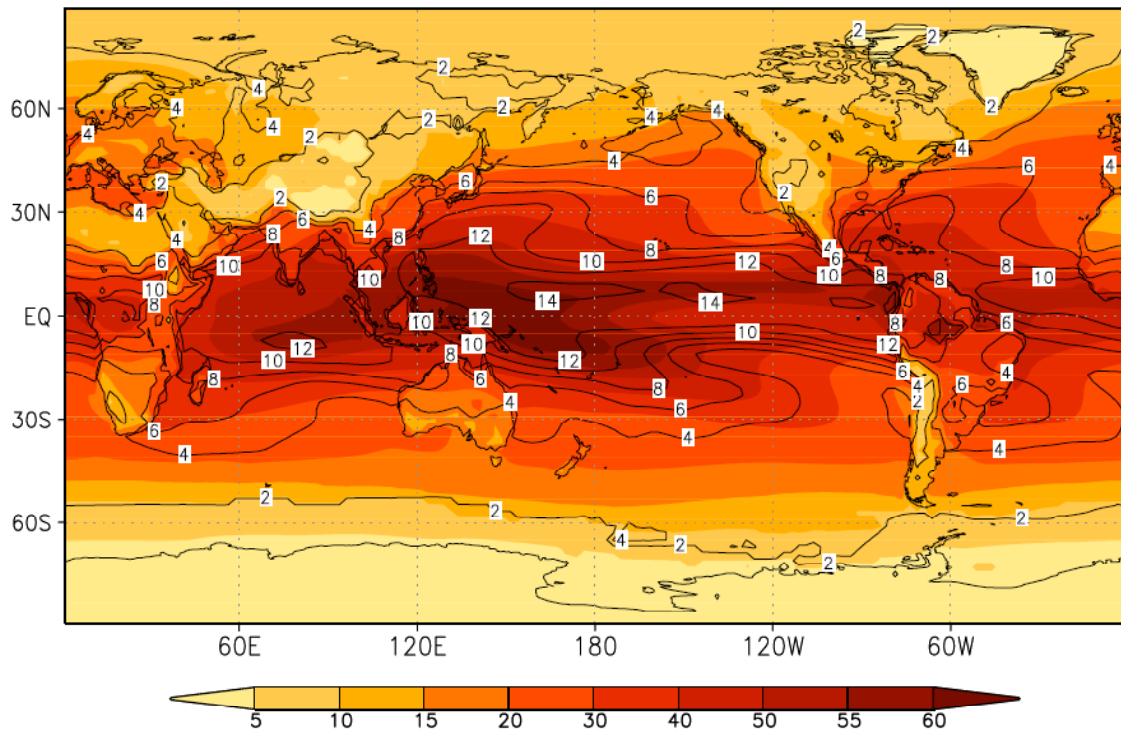


Figure 6.2: Vertically integrated specific humidity in the control simulation (color shadings), and its change in $2 \times \text{CO}_2$ simulation (contours) (unit: g/kg).

6.2 Water vapor feedback

The vertically integrated specific humidity increases due to the doubling of CO₂ as shown in Figure 6.2 (contours). The increase in atmospheric water vapor in response to the doubling of CO₂ is especially pronounced over low latitudes, which is 5 times as large as that over high latitudes. Water vapor is the most important greenhouse gas. Unlike CO₂, it is a non-linear molecule that goes through a range of rotational transitions (Petty, 2006). It absorbs infrared radiation throughout a broad spectra, especially at wavelengths shorter than 8 μm and larger than 14 μm. It also absorbs shortwave radiation. Under global warming, the atmospheric temperature warms and its water vapor holding capacity increases. As the water vapor concentration in the atmosphere increases, the amount of longwave radiation absorbed by the atmospheric column increases, creating a positive energy flux perturbation at the TOA. The water vapor feedback is computed using (4.13) by running the radiation transfer model once with a control climate fields and once with the specific humidity profile available from the 2 × CO₂ simulation, and taking the difference between the radiative energy fluxes in the two states.

Figure 6.3 displays the geographical distribution of the water vapor feedback at the TOA. The global average of the energy flux perturbation is 6.56 W m⁻², more than twice the value of the external forcing. Previous study that computed feedback parameters using the PRP method (by taking the ratio of the total radiative perturbation at the TOA due to change in water vapor to the total change in surface temperature, see equation 2.4) in the coupled ocean-atmosphere version of the GFDL_CM2.0 model gives a feedback parameter strength of 1.87 W m⁻² K⁻¹ (Soden and Held, 2006). The water vapor feedback computed using CFRAM can be compared to this value by taking the ratio of the water vapor feedback (6.56 W m⁻²) to the global change in surface temperature (2.93 K), which leads to a feedback parameter of 2.24 W m⁻² K⁻¹, 20% larger than previously computed. Part of the difference could arise from the fact that Soden and Held (2006) used a climate change scenario with increase in well-mixed greenhouse gases and aerosols (SRES A1B), and used the coupled ocean-atmosphere version of the GFDL_CM2.0 model. Also our radiation energy flux perturbation due to

change in water vapor is obtained under clear-sky condition. This could also explain a large value of water vapor feedback compared with that estimated by Soden and Held (2006). The geographical distribution of the radiative energy flux perturbation at the TOA follows closely the change in water vapor concentration displayed in Figure 6.2. Over the Equator, the radiative energy flux perturbation reaches 13 W m^{-2} and decreases poleward. The water vapor feedback is positive everywhere, which means an increase in the radiative energy convergence in the atmospheric column, but there is a difference of 12 W m^{-2} between the low and high latitudes. Over high latitudes the low temperatures combined with the small change in vertically integrated specific humidity lead to a small water vapor feedback. The radiative energy flux perturbation is smaller over Antarctica and Greenland than over the Northern hemisphere high latitudes. This resembles the time mean surface temperature pattern in the control climate (Figure 6.4), with temperatures over Antarctica about 20 K smaller than over the Arctic. The water vapor holding capacity of the atmosphere is therefore smaller over these areas, which undergo a smaller change in specific humidity under global warming. Therefore the water vapor feedback at the TOA follows the meridional temperature and specific humidity gradients. If the longwave and shortwave impacts on the water vapor feedback are studied individually, we notice that the decrease in outgoing longwave radiation at the TOA is responsible for the main water vapor feedback pattern. The outgoing shortwave radiation decreases too, from absorption by water vapor molecules, but by a smaller amount. It changes by about 0.4 W m^{-2} over the ocean, and by 0.4 W m^{-2} to 1.5 W m^{-2} over high latitudes and lands, with larger values over the Sahara (1.6 W m^{-2}) and over the Tibetan plateau (up to 2.4 W m^{-2}).

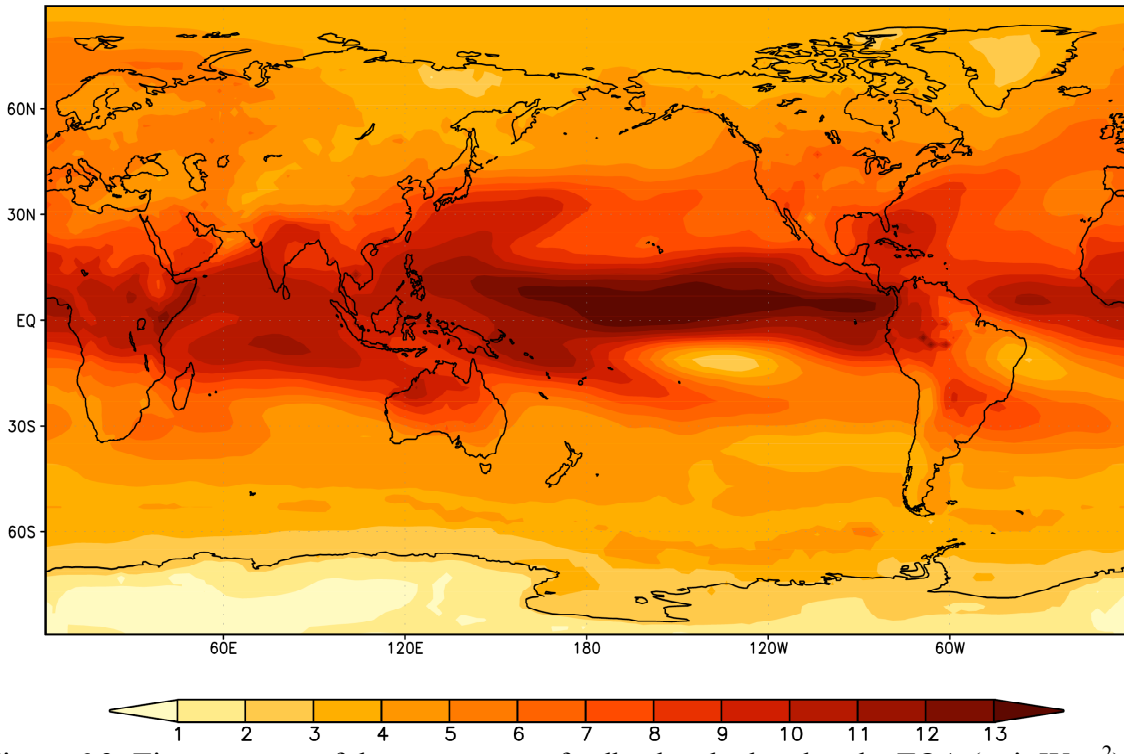


Figure 6.3: Time average of the water vapor feedback calculated at the TOA (unit: Wm^{-2}).

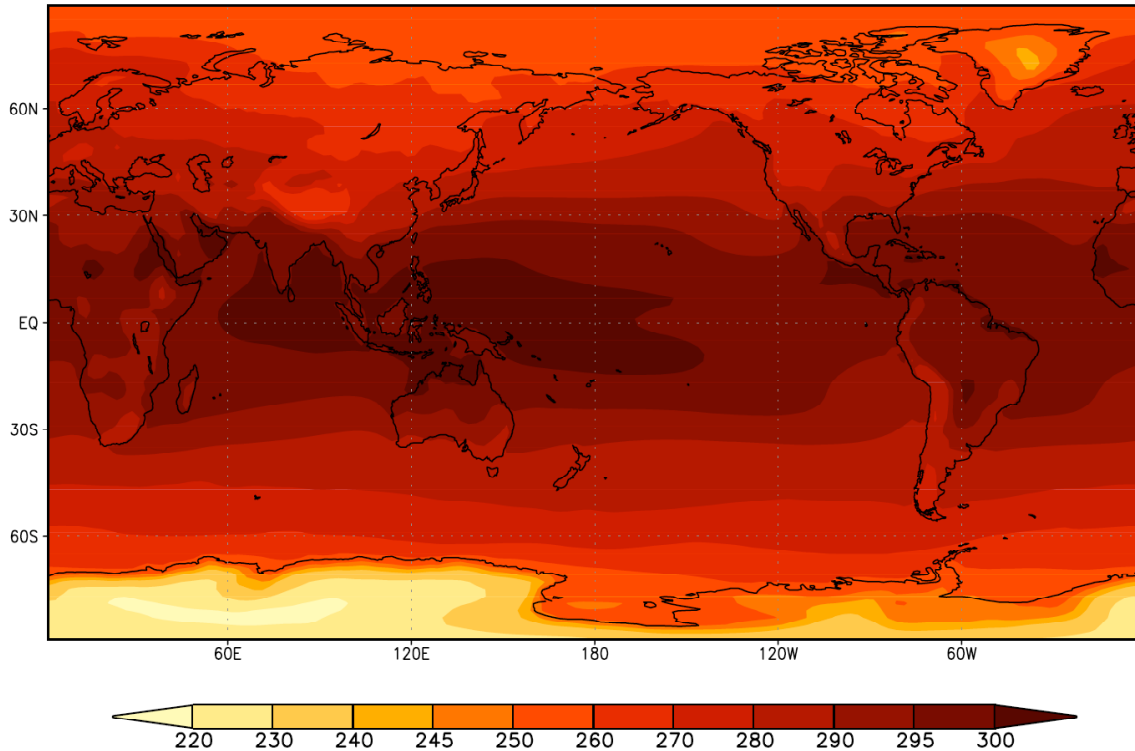


Figure 6.4: Time mean of the surface temperature in the control simulation (units: Kelvin).

6.3 Surface albedo feedback

The surface albedo is calculated as the ratio between the upward shortwave radiations and the downward shortwave radiations at the surface. Under global warming, the surface albedo in high latitudes decreases due to melting of ice/snow or change in the form of precipitation from snow to rain, which affects the shortwave range of the spectrum by increasing the amount of solar radiation absorbed at the surface. The change in radiative energy flux therefore positive at the surface and it affects the radiation budget at the TOA by decreasing the amount of reflected shortwave radiation to space. The albedo feedback is calculated using (4.14) by running the radiation transfer model once with a control climate fields and once with the surface albedo calculated from the $2 \times \text{CO}_2$ simulation, and taking the difference between the radiative energy fluxes in the two states. As discussed in chapter 4, (4.14) also includes the change in cloud forcing due to surface albedo change. The global average of the radiative energy flux perturbation at the TOA due to the change in surface albedo is equal to 1.15 W m^{-2} . A previous study that computed the feedback as the ratio of the total radiative perturbation at the TOA due to change in surface albedo to the total change in surface temperature gives a feedback parameter strength in the GFDL_CM2.0 model of $0.33 \text{ W m}^{-2} \text{ K}^{-1}$ (Soden and Held, 2006). Winton (2006) estimates the feedback to be $0.4 \text{ W m}^{-2} \text{ K}^{-1}$ for the GFDL_CM2.0 model. When taking the ratio of the surface albedo feedback to the global temperature change we get a feedback parameter similar to previous estimates with a value of $0.39 \text{ W m}^{-2} \text{ K}^{-1}$. The global average is relatively small compared to the geographical distribution of the surface albedo feedback that ranges between 0 W m^{-2} and 25 W m^{-2} (Figure 6.5). Because the surface albedo change is very little over open water and most of the land over low latitudes, except over highly elevated areas where snow cover and glaciers exist, the radiative energy flux perturbation due to change in the surface albedo mostly occurs over high latitudes. The largest energy flux perturbations are detected over the Arctic and the Southern Ocean, where sea-ice and ice sheets are melting. There is almost no change in radiative energy flux due to changes in the surface albedo over the ice sheet of Antarctica because the temperature is so low that the ice thickness remains deep enough under $2 \times \text{CO}_2$ radiative forcing. As a result the surface albedo does not change

significantly. The surface albedo feedback is larger than the external forcing and the water vapor feedback over high latitudes.

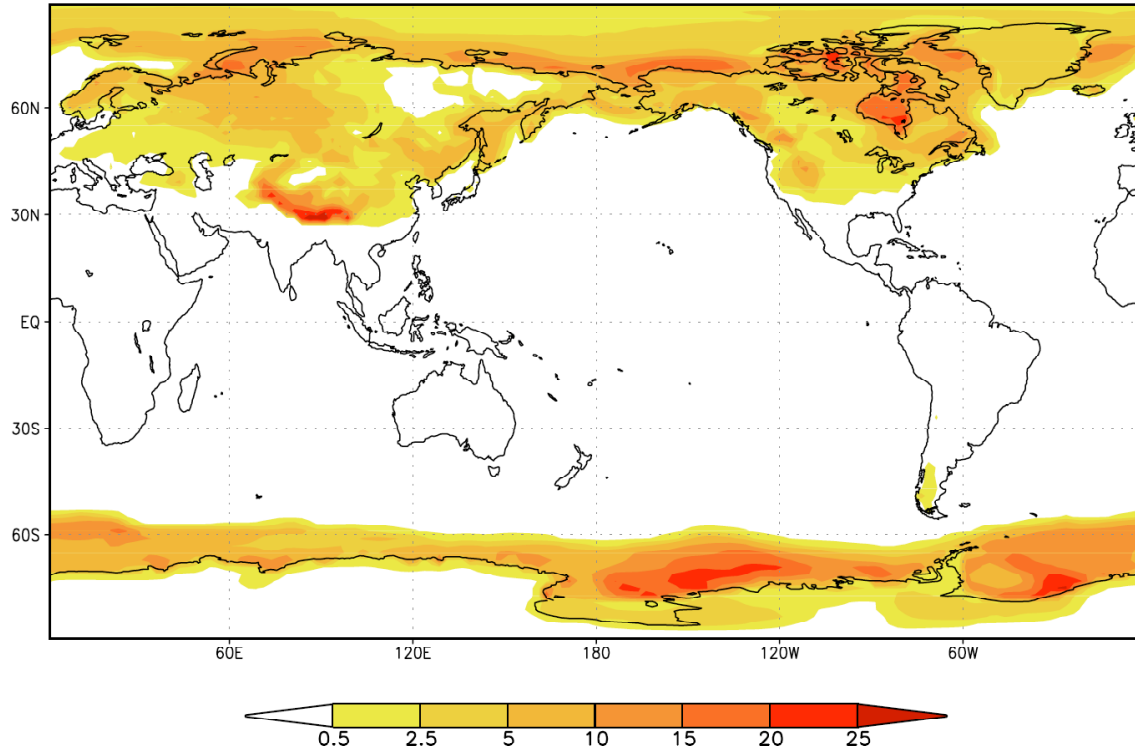


Figure 6.5: Time average of the surface albedo feedback calculated at the TOA (unit: W m^{-2}).

6.4 Inferred change in cloud forcing and dynamics

The amount of energy absorbed and emitted by the earth at the TOA is not locally balanced because of atmospheric and oceanic motions; there is a surplus of net radiation flux in low latitude and a deficit in high latitudes. If we integrate over the globe, the horizontal transport of heat is zero, since energy cannot be removed through horizontal transport. Under radiative forcing, the change in net clear sky radiation at the TOA is balanced locally by the sum of the change in poleward energy transport by the atmosphere and the change in cloud forcing (see Eq. (4.15) in chapter 4), part of which is therefore a non-radiative feedback. The change in cloud radiative forcing (CRF) and

dynamic feedback, therefore, can be inferred from the change in clear-sky net radiation flux at the TOA using (4.15). The change in clear-sky radiation can be obtained by running the radiation transfer model once with a control climate fields and once with the $2 \times \text{CO}_2$ simulation fields and taking the difference between the radiative energy fluxes in the two states. The inferred term displayed in Figure 6.6 includes a non-radiative energy flux perturbation (due to the change in dynamical heat transport), and a radiative energy flux perturbation (due to the change in CRF). It is possible to separate the change in CRF from the dynamical feedback when the clear-sky radiation energy flux perturbation at the TOA is averaged globally, because the global mean of the change in energy transport has to be zero. The global average of the clear-sky radiation change at the TOA therefore corresponds to the strength of the change in CRF, and is equal to 0.84 W m^{-2} (or $0.29 \text{ W m}^{-2} \text{ K}^{-1}$ after dividing by the global mean surface temperature change), which is relatively small compared to the other feedbacks and external radiative forcing. Cloud feedback calculated in previous studies display a large range of uncertainties. The feedback parameter computed by Soden and Held (2006) as the ratio of the total radiative perturbation at the TOA due to change in clouds to the total change in surface temperature gives a feedback parameter strength in the GFDL_CM2.0 model of $0.67 \text{ W m}^{-2} \text{ K}^{-1}$. Note that change in cloud forcing is different from the cloud feedback, because part of the change in cloud forcing is not due to change in clouds alone (and we only take out the part due to change in surface albedo from the change in cloud forcing). Therefore, it is expected the value of feedback parameter for cloud forcing is different from that for cloud feedback.

Although we cannot infer the feedbacks due changes in atmospheric circulations and due to changes in cloud forcing independently from the changes in clear-sky radiation alone, we can still relate the large-scale pattern in Figure 6.6 to the changes in poleward heat transport. In the climatological state, the earth receives more radiations than it emits back into space over low latitudes, equatorward of about 30° , and the opposite feature is true poleward of that latitude because of the poleward transport of heat. This radiation surplus (deficit) over low (high) latitudes due to the atmospheric heat transport reflects the poleward export of heat. Represented in Figure 6.6, the negative (positive) shadings over the low (high) latitudes imply an increased divergence

(convergence) of heat flux. Over the equatorial region, between 20°S and 20°N , the increase in heat flux divergence reaches 6 W m^{-2} . Poleward of these latitudes the heat flux convergence increases, especially over the poles where it reaches 6 W m^{-2} . This suggests that the poleward heat transport has been strengthened.

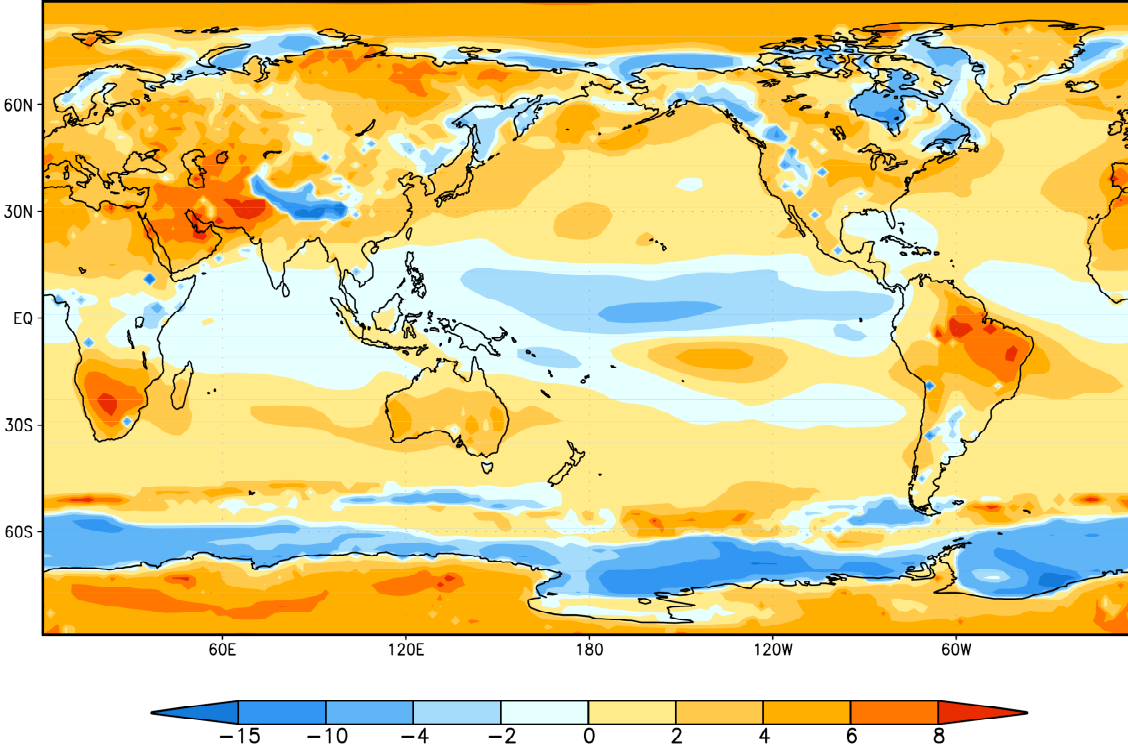


Figure 6.6: Time average of the sum of the changes in cloud forcing at TOA and in column integrated convergence of atmospheric energy transport inferred from the change of the net clear-sky radiation fluxes at the TOA (unit: W m^{-2}).

Since the energy flux perturbations due to the change in CRF and dynamic feedback are combined in Figure 6.6, it is also of interest to compare this result with an estimate of the poleward heat transport only. We infer the change in the total poleward heat transport due to a doubling of CO₂ in the GFDL_CM2.0 climate model simulation by examining the change of deficit (surplus) of the total sky net radiation flux at the TOA, similarly to equation (4.4) but with total sky radiation, according to:

$$-\Delta(S - R)^{\text{total_sky}} = \Delta D \quad (6.1)$$

Where $\Delta(S - R)^{total_sky}$ is the time averaged change between the $2 \times \text{CO}_2$ and control simulations of total-sky net radiation at the TOA. ΔD represents the time averaged change in the convergence of the total horizontal heat flux by the atmosphere, vertically integrated at a given location (in the equilibrium state, the heat storage term is assumed to be zero). If we integrate over the entire globe, the global mean of the total horizontal heat flux should be zero in the $2 \times \text{CO}_2$ and control climate states, since energy cannot be removed through horizontal transport. These global means are indeed very small but not exactly zero ($D_{1\text{CO}_2} = -1.49 \text{ W m}^{-2}$, $D_{2\text{CO}_2} = -1.54 \text{ W m}^{-2}$, and $\Delta D = -0.05 \text{ W m}^{-2}$). The total-sky radiation change is available from the GFDL_CM2.0 model's simulations outputs at the TOA and the surface. The energy flux perturbation due to the change in convergence of the vertically integrated atmospheric heat flux can therefore only be computed at the TOA (Figure 6.7) and compared to Figure 6.6. The contours in Figure 6.7 represents the convergence of the atmospheric heat transport in the control state, with positive (negative) values indicating deficit (surplus) of the net radiation energy flux at the TOA in high (low) latitudes. The shadings are the changes in the convergence of vertically integrated atmospheric energy transport inferred from the changes in the total sky radiation budget at the TOA. It is seen that the heat flux divergence at low latitudes increases by more than 10 W m^{-2} and so does the convergence of heat flux at high latitudes by up to 9 W m^{-2} over the north pole and 6 W m^{-2} over the south pole in response to $2 \times \text{CO}_2$ forcing.

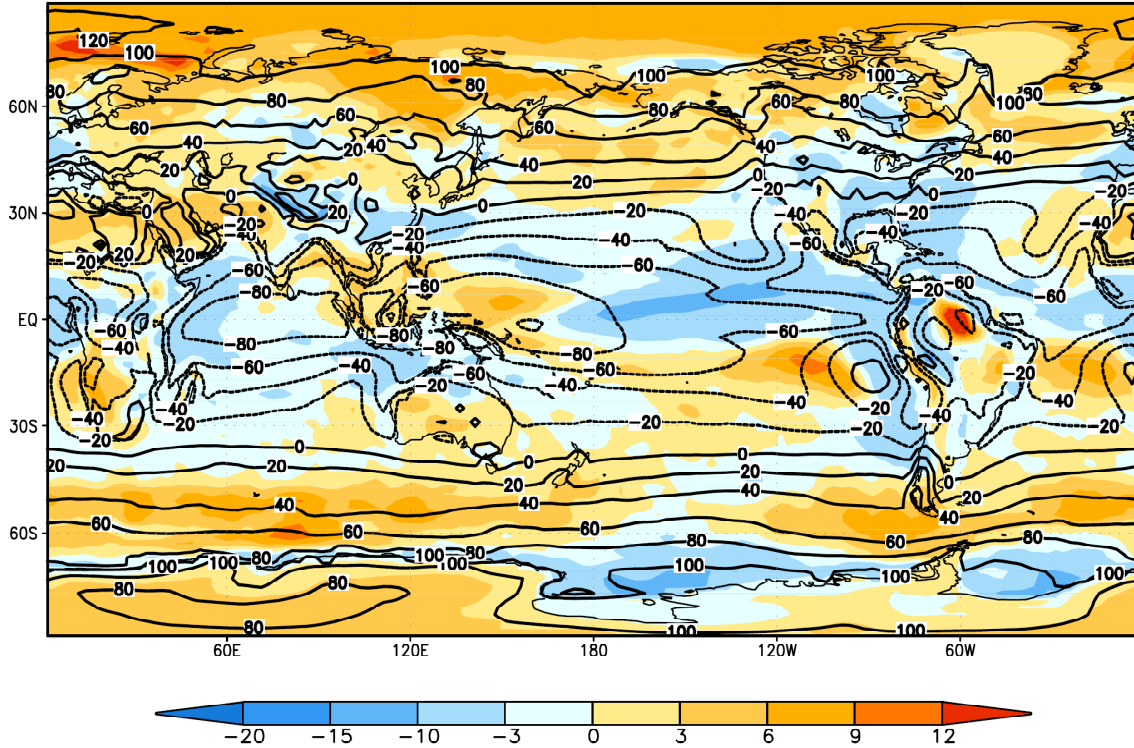


Figure 6.7: Total heat transport (contours) and change in total heat transport (color shadings) inferred from the net total sky radiation fluxes at the TOA (unit W m^{-2}).

Figure 6.8 represents the difference between Figure 6.6 (sum of the change in CRF and dynamical feedback) and Figure 6.7 (dynamical feedback only), which is an estimate of the change in CRF under radiative forcing. The effects of clouds on the TOA radiation budget are well understood. For example the high and cold clouds over tropical warm SST reduce more longwave radiation going out to the space, but increase solar radiation reflected by clouds (Stephens, 2005). As the climate warms, the cloud distribution, cloud top, and optical depth are modified, thereby changing the CRF. The global average of the change in CRF is positive, equal to 0.9 W m^{-2} , meaning that under $2 \times \text{CO}_2$ radiative forcing the change in cloud distribution and properties will increase in the amount of radiative energy in the climate system. Looking at the regional distribution in Figure 6.8, we notice that over continents the change in CRF is mainly positive except poleward of 60°N . The tropics show a zonal asymmetry in the change in CRF. The warm pool over the western part of the Pacific along with a narrow band extending toward the south-east show a decrease in CRF by as much as -10 W m^{-2} . This is also the case over

the south-eastern part of the Atlantic and Pacific Ocean, while the remaining part of the tropics shows an increase in CRF of up to 10 W m^{-2} . The subtropics show an increase in CRF, mostly less than 5 W m^{-2} . The picture over mid-latitudes is less clear. In the northern hemisphere, the change in CRF is negative over the Pacific and the northern part of the Atlantic Ocean. Over the southern hemisphere midlatitudes, the CRF is negative over the Southern Ocean, reaching values of -15 W m^{-2} , and is positive elsewhere. Finally, over the North Pole the CRF decreases by up to 5 W m^{-2} , and over the South Pole it increases by up to 5 W m^{-2} . This is consistent with the CRF calculated at the surface in Figure 4.3b using our offline clear-sky radiation calculations (RHS of equation 4.21), where we found a decrease in CRF over the North Pole to be due to additional non-cloud feedbacks due to cloudy sky temperature and water vapor changes at the surface. Over Polar Regions, an increase in low cloud cover increases the amount of shortwave radiation reflected back to space but increases the amount of longwave radiation emitted toward the surface, therefore increasing the CRF at the surface (Randall et al., 2007; Bony et al., 2006). At the TOA, more shortwave radiation is reflected back to space but less outgoing longwave radiation is reaching the TOA also generating a positive change in CRF.

It is possible to compare the geographical distribution of the change in CRF with the available cloud outputs of the IPCC AR4 climate simulations, which provide the change in total cloud fraction and total atmospheric condensed water content. The cloud area fraction in the entire atmospheric column as seen from the TOA and its change under $2 \times \text{CO}_2$ forcing is plotted in Figure 6.9a, and amount of atmospheric cloud condensed water in liquid and ice phase as well as its change under $2 \times \text{CO}_2$ forcing is plotted in Figure 6.9b. In the control climate (contours), the largest cloud area fraction (80%-90%) is present over the tropical warm pools, the midlatitude storm track, the North Pole and the Southern Ocean, and the smaller cloud cover (20%-50%) are over deserts, the eastern part of the tropical pacific basin, and the latitudes around the subtropics (20° - 30° of latitude). Comparatively, the largest amount of cloud's condensed water ($20\text{-}25 \text{ g m}^{-2}$) is present over the midlatitude storm tracks and the southern ocean, and the lowest amount (5 g m^{-2}) coincides with the locations of small cloud fraction, except over the poles because of the small availability of water vapor. One feature of the

change in clouds over continents is the decrease in cloud area fraction, especially over northern part of South America and southern part of Africa by 6 to 9%, and the slight increase in cloud condensed water. These regions coincide with an increase in CRF with values over 6 W m^{-2} because less shortwave radiation are reflected back to space by the clouds, and more longwave radiation is trapped by the increase in cloud condensed water. These regions also have a large increase in surface temperature (Figure 1.5). In the tropics there is an apparent increase in cloud fraction and water content in the eastern tropical Pacific and Atlantic oceans leading to more longwave radiation trapped by the cloud layer and more shortwave radiation reflected back to space. This area corresponds to an increase in CRF, indicating that the longwave CRF dominates the shortwave CRF over this region, except over the south-eastern part of the Atlantic and Pacific Ocean, where the CRF decreases. These regions show a small increase in surface temperature (Figure 1.5) suggesting that the shortwave CRF dominates the longwave CRF. The rest of the tropics show a decrease in cloud area fraction. Over the Indian Ocean, the cloud water content increases and both cloud changes contribute to the increase in CRF. On the other hand, over the Pacific warm pool and a narrow band extending toward the southeast, the small decrease in cloud fraction should induce a positive shortwave CRF, and the increase in cloud condensed water should induce a positive longwave CRF. Instead this region shows a strong decrease in total CRF, which may mean that the increase in cloud condensed water over this region of large cloud cover (80%-90%), strong convection, and high cloud tops has a large impact on the amount of shortwave radiation reflected back to space. The same phenomenon occurs in the northern hemisphere midlatitudes over the Pacific and the northern part of the Atlantic Ocean, and over the Southern Ocean. In the subtropics, the cloud fraction and water content are small and decrease under $2 \times \text{CO}_2$ forcing. This leads to less shortwave reflected back to space and more longwave escaping to space but the overall effect is an increase in CRF, meaning that the shortwave CRF dominates. In the southern hemisphere midlatitudes between 30° and 45°S , the CRF increases owing to the positive CRF due to the decrease in cloud area fraction. Finally, the cloud area fraction increases over high latitudes (poleward of 60°) together with the amount of atmospheric cloud condensed water of up to 8 kg m^{-2} . This leads to the positive energy flux perturbation over the South Pole and Greenland due to the positive

longwave CRF (less longwave escaping to space) dominating the negative shortwave CRF (more shortwave reflected back to space).

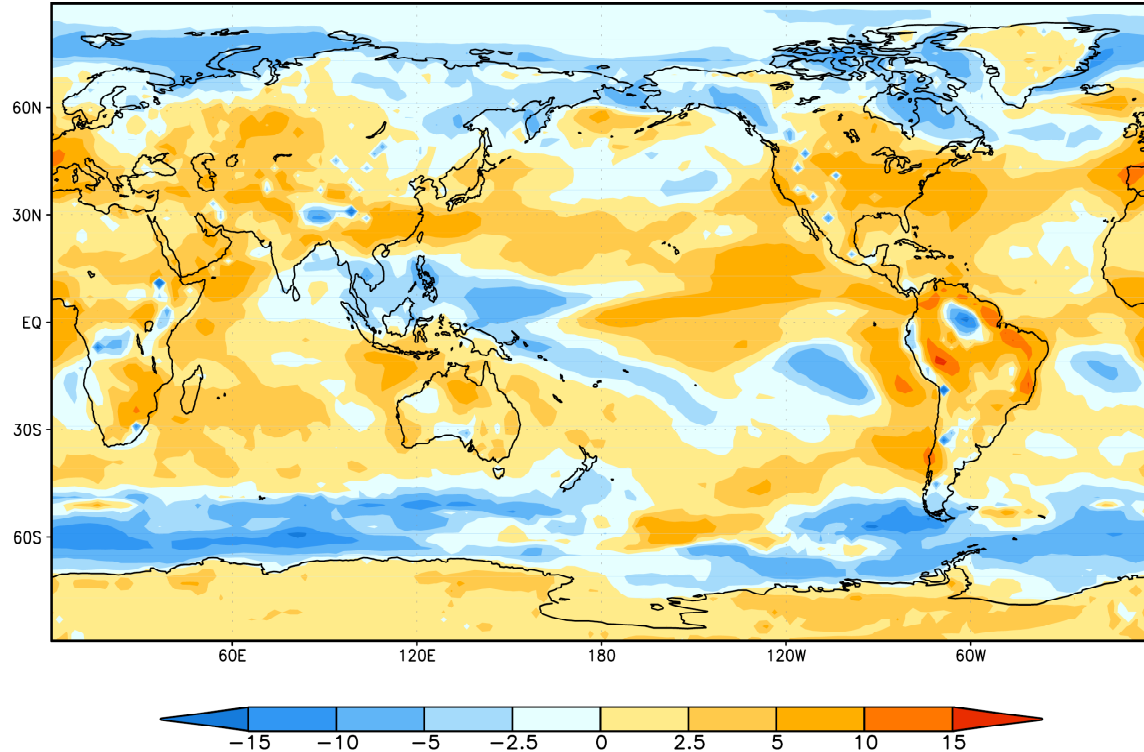


Figure 6.8: Change in cloud forcing inferred from the difference between Figure 6.6 and 6.7. (unit W m^{-2}).

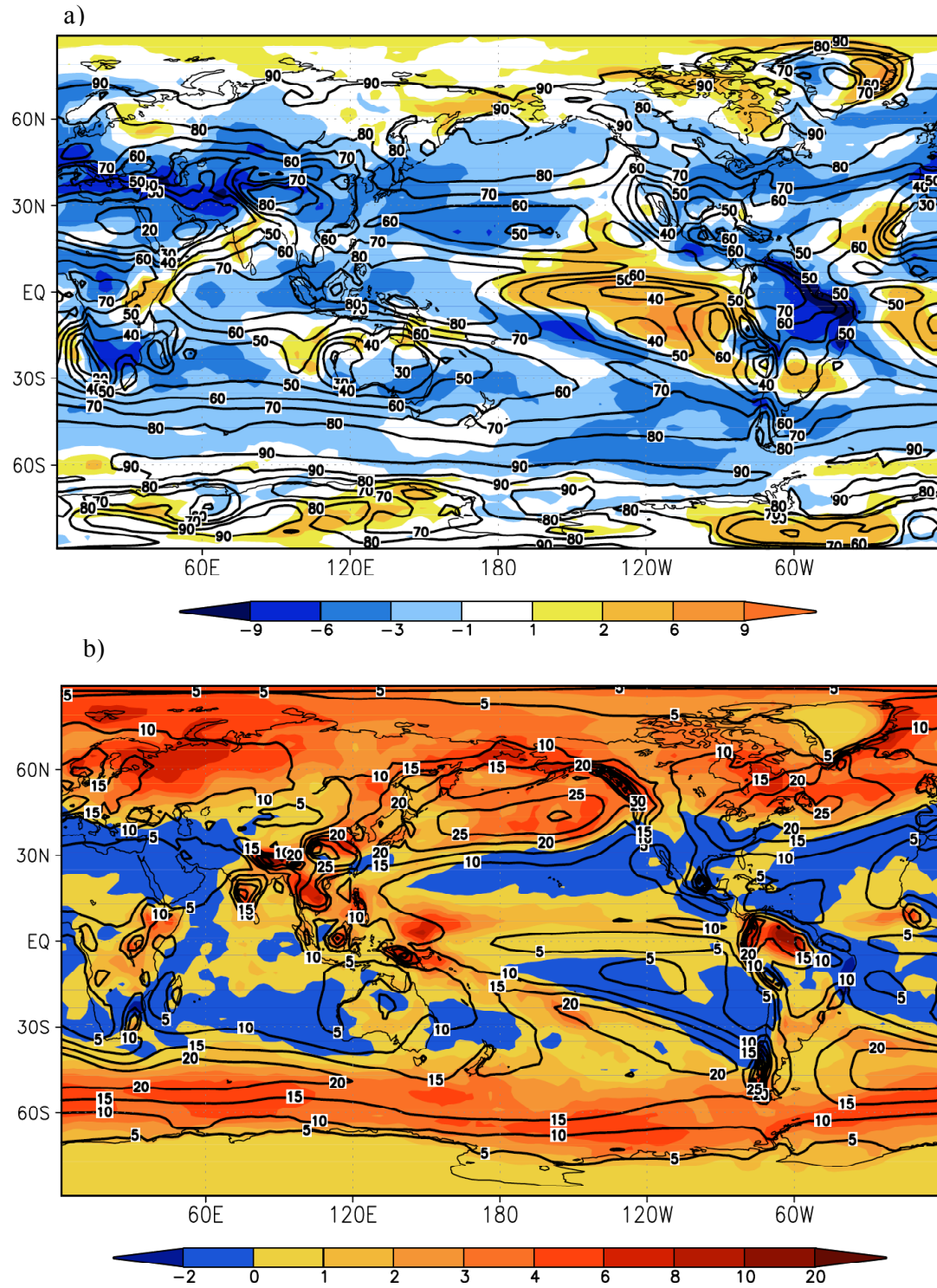


Figure 6.9: a) Cloud area fraction in the entire atmospheric column as seen from the TOA (%), and b) amount of atmospheric cloud condensed water (in both liquid and ice phases) (g m^{-2}). Control climate (color shadings), and change in the $2 \times \text{CO}_2$ climate simulation (contours).

6.5 Discussion

A comparison between the external forcing and individual energy flux perturbation at the TOA offers a perspective on net change in energy input to the climate system due to each term. Each change in energy flux at the TOA can be regarded as an energy source/sink contributing to a temperature change in the atmosphere-surface column below.

- On a global average, the water vapor feedback is the strongest positive feedback under doubling of CO₂. The next important participant in the positive radiative energy flux perturbation at the TOA is the external forcing, followed by the albedo feedback and the cloud forcing. The overall positive value of each feedback indicates that the climate system gains more energy when CO₂ is doubled, reinforcing the initial climate forcing. This requires the climate system to warm further such that the extra outgoing radiation emitted by the warmer climate system can balance the extra energy entering the system resulting from feedbacks.
- The geographical distribution of the external forcing shows larger values over low latitudes, between 45°N and 45°S, especially over the subtropical oceans and decreasing poleward. Therefore, the doubling of CO₂ by itself acts to trap more thermal energy in the tropics where the mean temperature is warmer.
- The water vapor feedback is the strongest over the equator and decreases poleward, as the change in the atmospheric specific humidity decreases. Its global average value over 60°N and 60°S is 7 W m⁻², more than twice the value of the external forcing (Table 6.1).
- The albedo feedback strongly acts over regions of sea ice melting, and also plays a role over high latitudes continents where snow and ice melt, and glaciers retreat. It is the strongest feedback above 60° of latitude, and is equal to 5 W m⁻² over the North Pole and 5.7 W m⁻² over the South Pole (Table 6.1).
- The inferred sum of the change in cloud forcing and dynamical feedback from our offline clear-sky radiation calculation displays a pattern of increased divergence (convergence) of atmospheric energy transport over low (high) latitudes. The

energy flux perturbation due to the change in poleward heat transport computed at the TOA from the GFDL_CM2.0 model's total sky simulations outputs supports this result.

- The geographical distribution of the inferred change in CRF at the TOA is complex, with a positive global average equal to 0.9 W m^{-2} . It means that the change in CRF generates a net increase of energy in the climate system.
- The averaged zonal distribution of each energy flux perturbation is summarized in Table 6.1. Over the southern and northern high latitudes (SHL and NHL) the surface albedo feedback is dominant. Over low latitudes (LOW) the water vapor feedback is the strongest. Over the southern high latitudes (90°S to 60°S), the external forcing and the water vapor feedback are weaker than over the northern high latitudes by 12.8% and 33.7% respectively. The inferred sum of the change in cloud forcing and dynamical feedback is negative over the southern hemisphere high latitudes owing to a strong negative shortwave CRF over the southern ocean, and positive elsewhere, due to an overall decrease in cloud fraction in the tropics and mid-latitudes generating a positive shortwave CRF (decrease in reflected solar radiation to space).
- The sum of the water vapor, albedo and cloud feedback parameter is $2.92 \text{ W m}^{-2} \text{ K}^{-1}$. Comparatively, Soden and Held (2006) obtained a sum of $2.87 \text{ W m}^{-2} \text{ K}^{-1}$. Differences between the same feedback parameters arise from the use of different versions of the GFDL_CM2.0 model and a different climate change scenario. But overall the total feedback parameters are very similar (within 1.7%).

Table 6.1: Average of the external forcing and each feedback as view from the TOA over high latitudes ($\pm 90^\circ$; $\pm 60^\circ$) and low latitudes (-60;60). (Unit: W m^{-2}).

	$\Delta^{(\text{CO}_2)}\text{F}$	$\Delta^{(\text{H}_2\text{O})}\text{F}$	$\Delta^{(\alpha)}\text{F}$	$\Delta^{(\text{Cf+D})}\text{F}$
SHL (-90;-60)	2.06945	2.68525	5.75289	-2.01349
LOW (-60;60)	3.25221	7.06191	0.460837	0.996162
NHL (60;90)	2.37326	4.04636	5.00146	1.70138

CHAPTER 7

RESULTS OF CFRAM ANALYSIS ON THE GFDL_CM2.0 GLOBAL WARMING SIMULATION

The energy flux perturbations due to the external forcing and subsequent feedbacks studied at the TOA in Chapter 6 are here calculated at each atmospheric layer and at the surface. They are computed together with their associated partial temperature changes using CFRAM. The first three sections of this chapter study the clear-sky thermodynamic feedbacks and associated partial temperature changes due to the doubling of CO₂, changes in water vapor, and surface albedo. The next three sections study the feedbacks due to changes in surface turbulent heat fluxes, surface cloud feedback, and the sum of the change in cloud forcing and large-scale dynamics inferred from the change in net clear-sky radiation flux in the atmosphere. The radiative energy flux perturbations at each atmospheric layer are defined as the changes in the convergence of radiative energy fluxes in atmospheric layers. The surface energy flux perturbation is defined as the change in energy flux into the surface layer. The vertical summation of the radiative energy perturbations in each atmospheric layer and at the surface layer is identical to the radiative energy perturbation at the TOA. The sum of partial temperature change in the atmosphere and at the surface due to external forcing and individual feedbacks can be compared to the GFDL_CM2.0 model simulated total warming to study how each feedback affect the total temperature change pattern described in Figure 1.5.

7.1 External radiative forcing and its induced temperature changes

The partial temperature change associated with the energy flux perturbation due to the doubling of atmospheric CO₂ concentration is computed at each atmospheric layer and at the surface as the product of the inverse of the Planck feedback matrix and the energy flux perturbation:

$$\Delta\bar{T}^{(CO_2)} = \left(\frac{\partial\bar{R}}{\partial\bar{T}} \right)^{-1} \Delta\bar{F}^{(CO_2)} \quad (7.1)$$

where $\Delta\bar{F}^{(CO_2)}$ is computed using (4.12). The zonal and time mean of the vertical profile of the energy flux perturbation, and the time mean of the surface energy flux perturbation due to the doubling of CO₂ are displayed in Figures 7.1a and 7.1c. The associated temperature changes in the atmosphere and at the surface are displayed in Figures 7.1b and 7.1d.

The radiative forcing in the atmosphere (Figure 7.1a) shows a bell shape pattern of positive values from the lower part of the troposphere up to 700 hPa over high latitudes and 500 hPa over the equator. Two maxima are located between 900 and 800 hPa over the extratropics. As noted in chapter 6, the greenhouse effect of carbon dioxide competes with the greenhouse effect of water vapor. This occurs in the 12-18 μm spectral region, where the CO₂ absorption bands overlaps with the pure rotational and continuum water vapor bands of water vapor (Kiehl and Ramanathan, 1982). The energy flux perturbation due to radiative forcing is therefore smaller over the equator at the surface with a 3.5 W m⁻² difference between low and high latitudes, and in the atmosphere from 900 hPa to 700 hPa with a 1.5 W m⁻² difference between low and mid-latitudes. The large water vapor concentration in the mean control state limits the greenhouse effect of the increase in CO₂ concentration over these regions. The vertical limit of the positive energy flux perturbation is higher in the atmosphere over the tropics than at the poles. Moving vertically, the energy flux perturbation becomes negative up to 300 hPa, then positive again near the tropopause.

At the surface (Figure 7.1c), the energy flux perturbation is positive everywhere with values up to 4 W m⁻² over high latitudes, regions of high elevations, and deserts.

The water vapor concentration in the mean state over these regions is minimum (see Figure 6.2). As a result, the overlapping effect between CO₂ and water vapor is minimal in these regions. Therefore, even though the low surface temperatures over cold places lead to only a small amount of additional outgoing long wave radiation being trapped by the increase of CO₂ compared that in low latitudes the external energy perturbation at the surface can still be strongest in high latitudes. These values are twice as large as the maximum values in the atmosphere. Comparing the radiative forcing at the TOA (Figure 6.1) to its surface distribution, one can notice that the location of largest energy flux perturbation at the TOA differs from its location at the surface. This means that a large part of the change in radiation convergence in the atmosphere/surface bellow calculated at the TOA over the tropics is carried out in the atmosphere (Figure 7.1a). The small values of the total energy flux perturbation at the TOA over high latitudes even though the surface yield large radiative forcing there is due to the fact that the tropopause is lower over high latitudes, and therefore the stratospheric cooling rate due to the doubling of CO₂ is also larger. Also the surface temperature over Antarctica is much colder, implying a much weaker radiative energy trapping by the increase of CO₂. It is important to study radiative forcing not only at the TOA, as done in the PRP method, or at the surface as suggested in Randall et al. (2007), but also in the entire atmospheric column to gain a better understanding of the effect of the doubling of CO₂ on the change in radiative energy flux convergence in the atmosphere/surface bellow.

The vertical and surface profile of the partial temperature change (Figures 7.1b and 7.1d) is calculated by requiring its associated infrared radiation perturbation to balance the perturbation forcing (due to the doubling of CO₂) at each layer using (7.1). The temperature change is the largest over the poles at the surface and in the lowest troposphere where it reaches 1.7 K. The warming is the smallest over the equator at the surface and lowest troposphere where it only reaches 1 K. The maxima then meet each other over the equator in the mid-troposphere. Although the general pattern of the atmospheric warming due to the external forcing follows the spatial variation the external forcing, the details differ with the atmospheric energy flux perturbation pattern. For example, in the upper troposphere, the external radiative forcing is negative, but the

temperature change there is still positive. This is because the energy flux perturbation at each atmospheric layer/surface is in balance with the infrared radiation perturbation in that layer/surface generated by the temperature change in the entire atmosphere-surface column. In other words the atmosphere and surface temperature change are not independent from one another. In the lowest troposphere, the warming pattern is similar to the total temperature change in the GFDL_CM2.0 model $2 \times \text{CO}_2$ simulation (Figure 1.5a), but the intensity of the warming is much smaller, implying that the subsequent feedbacks (water vapor, albedo, cloud, and large scale dynamics) contribute largely to the total warming. Negative temperature changes are present in the mid-troposphere over the South Pole where the negative energy flux perturbation is the largest, and in the stratosphere because the external radiative forcing is negative there. At the surface, the temperature change is the strongest over high latitudes because the external forcing is strongest there, contributing to the global warming pattern in the GFDL_CM2.0 model $2 \times \text{CO}_2$ simulation (Figure 1.5b). The globally averaged temperature change at the surface due to the radiative forcing alone is equal to 1.08 K. Comparing it to the globally averaged total temperature change in the GFDL_CM2.0 model, 2.93 K, highlights the importance of the subsequent feedbacks in the total temperature change as discussed in the remaining part of this chapter.

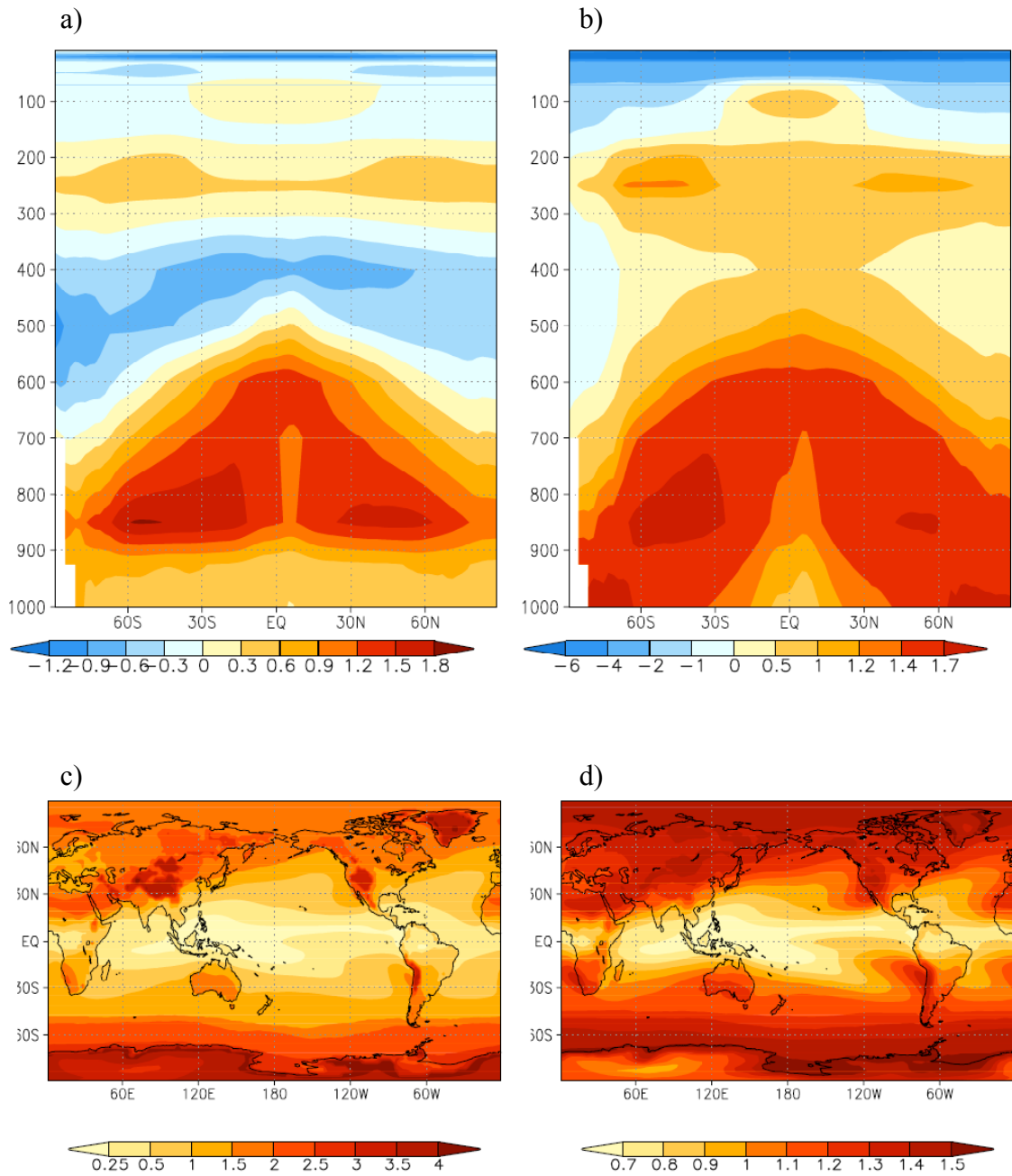


Figure 7.1: Radiative energy flux perturbation (unit: W m^{-2}), and associated partial temperature change (unit: K) due to external forcing: zonal and time mean of the vertical profile a) and b), and time mean at the surface c) and d).

7.2 Water vapor feedback and its induced temperature changes

The partial temperature change associated with the energy flux perturbation due to the change in water vapor concentration under radiative forcing is computed at each atmospheric layer and at the surface as the product of the inverse of the Planck feedback matrix and the energy flux perturbation:

$$\Delta\bar{T}^{(h_2o)} = \left(\frac{\partial\bar{R}}{\partial\bar{T}} \right)^{-1} \Delta\bar{F}^{(h_2o)} \quad (7.2)$$

where $\Delta\bar{F}^{(h_2o)}$ is computed using (4.12). The zonal and time mean of the vertical profile of the energy flux perturbation, and the time mean of the surface energy flux perturbation due to the water vapor feedback are displayed in Figures 7.2a and 7.2c. The associated temperature changes in the atmosphere and at the surface are displayed in Figures 7.2b and 7.2d.

In the atmosphere (Figure 7.2a), the range of the change in energy flux perturbation is comparable with that of the radiative forcing (between -1.2 W m^{-2} and 1.5 W m^{-2}), but the larger values are located in the lower part of the troposphere, where the largest change in water vapor occurs. Indeed, Figure 7.3 shows that the change in specific humidity (contours) displays a large increase over the equator, and a smaller increase as we move away from the source of moisture toward high latitudes and the upper troposphere. The energy flux perturbation due to change in atmospheric water vapor is negative over a large portion of the atmosphere with maximum values over 30 degrees of latitudes below 900 hPa, connecting over the equator between 900 and 800 hPa. A positive energy flux perturbation is present over the equator and high latitudes below 950 hPa, and between 700 and 600 hPa with a maximum of 1.5 W m^{-2} . The radiative energy flux perturbation is also positive from 60°S to 60°N over the mid-troposphere, over all latitudes at 300 hPa, and over the equator at 100 hPa. These values are much smaller than that at the TOA, where the radiative energy flux perturbation due to water vapor feedback can be as large as 13 W m^{-2} (see Figure 6.3). Therefore the larger part of

the change in radiative energy flux perturbation due to water feedback at the TOA over the equator is due to the energy perturbation at the surface.

Indeed, the energy flux perturbation due to water vapor feedback at the surface is positive everywhere, with values over the equator that are one order of magnitude larger than in the atmosphere (more than 12 W m^{-2}). It is also much larger than the energy flux perturbation due to the external radiative forcing over the tropics and also over the northern high latitudes. However, they are very similar in strength over the southern high latitudes. This is consistent with Collins et al. (2006) results that found that the surface forcing due to the water vapor feedback is larger than the surface forcing by well mixed greenhouse gases in both line by line and AOGCM calculations under clear-sky and aerosol free condition.

The vertical and surface profile of the partial temperature change (Figures 7.2b and 7.2d) is calculated by requiring its associated infrared radiation perturbation to balance the perturbation forcing (due to the water vapor feedback) at each layer using (7.2). The temperature change shows an opposite warming signal than the temperature change due to the external radiative forcing in the lower troposphere and at the surface, with larger warming over the equator throughout the troposphere and a maximum warming of 5°C at the surface. This follows the vertical and meridional distribution of the energy flux perturbations due to water vapor feedback. The change in atmospheric temperature is negative over high latitudes from 700 hPa all the way to the TOA, also due to the negative energy flux perturbation over these areas, and because they are far away from the impact of the surface warming. It is seen that temperature changes due to water vapor feedback in the lower troposphere are positive although the radiative energy perturbations there are negative. Recall that in the CFRAM, the temperature changes in all layers (including the surface layers) due to feedbacks are calculated jointly (via the inverse of the Planck matrix) in such a way that the infrared radiation perturbations due to the (calculated) temperature changes in the entire atmosphere-surface column are exactly balanced with the energy perturbations due to feedbacks. Therefore the warming pattern in the lower troposphere due to the water vapor feedback is dominated by the impact of the large energy flux perturbation at the surface, instead of the radiative energy

perturbations in the lower troposphere themselves. In the upper troposphere and stratosphere, the warming pattern is similar to the total temperature change in the GFDL_CM2.0 model $2 \times \text{CO}_2$ simulation (Figure 1.5a) with a larger warming over the equator at 300 hPa, and cooling over high latitudes above 200 hPa and in the stratosphere. However, they differ greatly below 400 hPa. At the surface, the temperature change reaches 5 K over the equator, which is relatively small compared to the strength of the energy flux perturbation at the surface. This is because large portion of the atmosphere has a negative energy flux perturbation, which acts to reduce the surface warming. Compared to the global warming pattern in the GFDL_CM2.0 model $2 \times \text{CO}_2$ simulation (Figure 1.5b), the water vapor feedback shows an opposite pattern, with the large equatorial warming disappearing in the global warming pattern. Nevertheless, it contributes to almost half of the large (5.5 K) warming over the northern high latitudes, more than the external radiative forcing contribution over the same region. It also contributes equally to the warming over the southern high latitudes with the radiative forcing. The globally averaged temperature change at the surface due to the water vapor feedback alone is equal to 2.53 K, more than twice the temperature change due to the external radiative forcing.

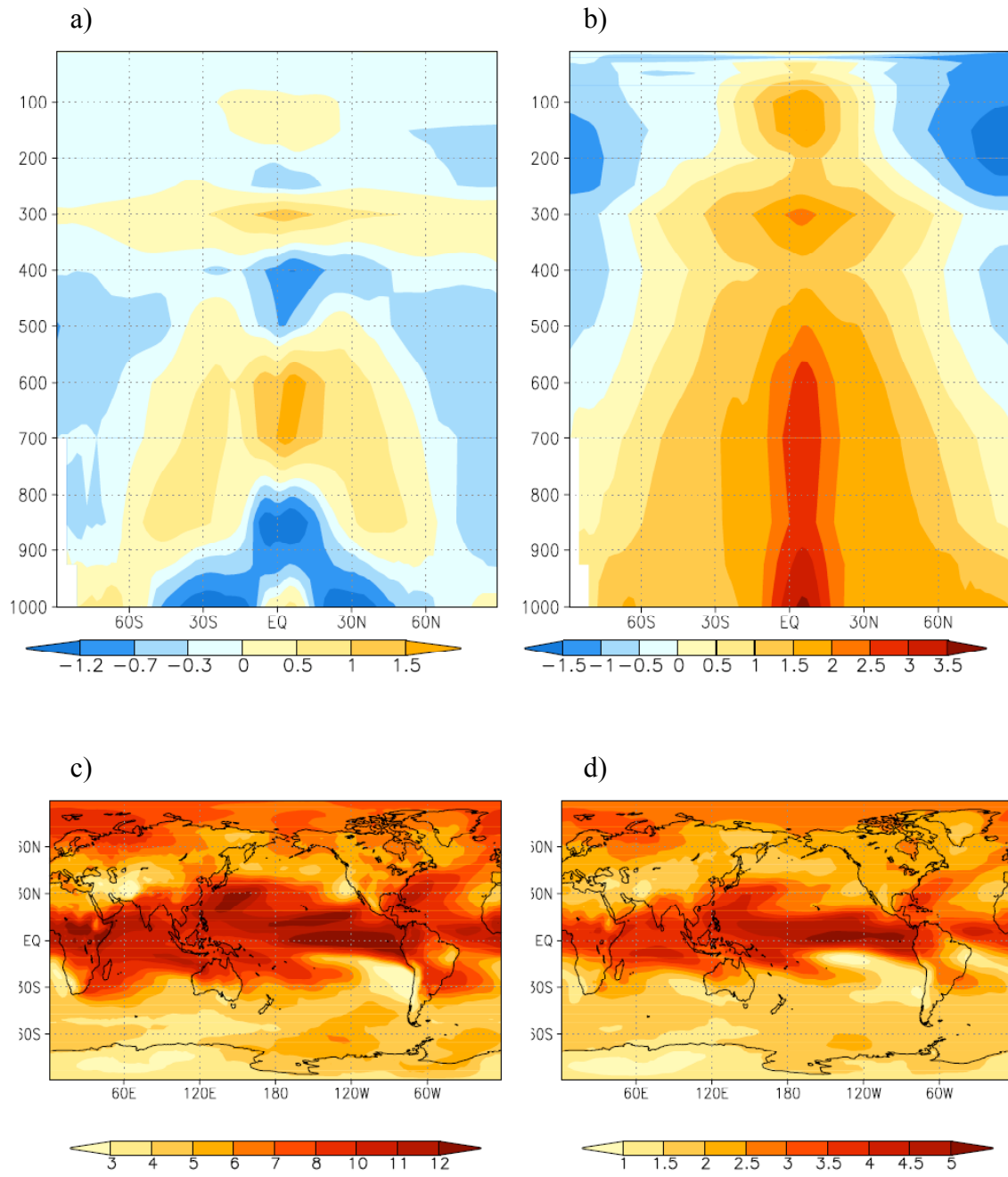


Figure 7.2: Radiative energy flux perturbation (unit: W m^{-2}), and associated partial temperature change (unit: K) due to the water vapor feedback: zonal and time mean of the vertical profile a) and b), and time mean at the surface c) and d).

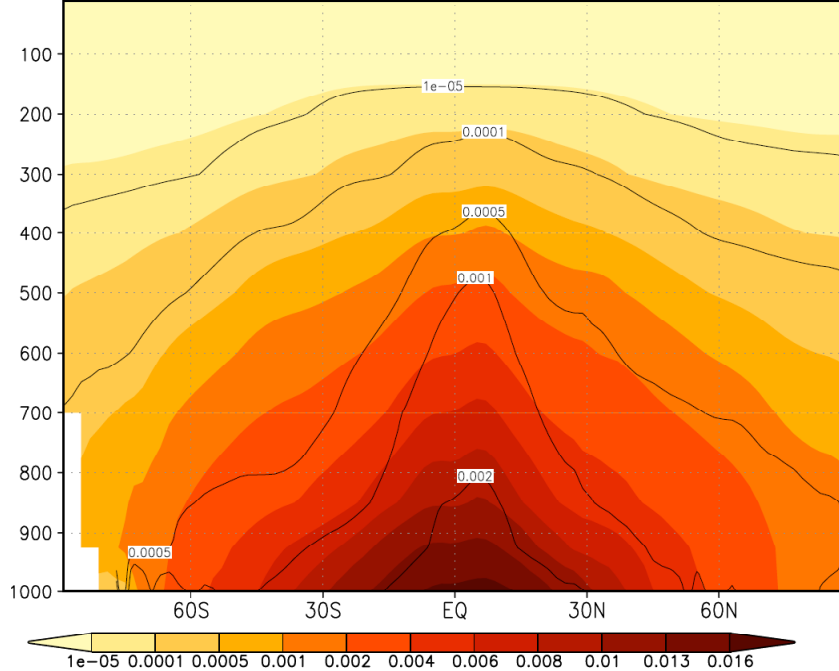


Figure 7.3: Zonal mean of the vertical profile of specific humidity (color shadings), and change in specific humidity in the $2 \times \text{CO}_2$ climate simulation (contours), (unit: kg/kg).

7.3 Surface albedo feedback and its induced temperature changes

The partial temperature change associated with the energy flux perturbation due to the surface albedo feedback is computed at each atmospheric layer and at the surface as the product of the inverse of the Planck feedback matrix and the energy flux perturbation:

$$\Delta \bar{T}^{(\alpha)} = \left(\frac{\partial \bar{R}}{\partial \bar{T}} \right)^{-1} \Delta \bar{F}^{(\alpha)} \quad (7.3)$$

where $\Delta \bar{F}^{(\alpha)}$ is computed using (4.12). The zonal and time mean of the vertical profile of the radiative energy flux perturbation, and the time mean of the surface radiative energy flux perturbation due to the change in surface albedo are displayed in Figures 7.4a and

7.4c. The associated temperature changes in the atmosphere and at the surface are displayed in Figures 7.4b and 7.4d.

The radiative energy flux perturbation in the atmosphere and surface (Figure 7.4a and 7.4b) due to the surface albedo feedback is only present over regions where snow and ice are melting or the form of precipitation changing from snow to rain. It is negative in the lowest part of the atmosphere, and is two orders of magnitude smaller than at the surface, with values reaching -0.1 W m^{-2} at most close to the surface. This is because the increase in shortwave radiation absorbed at the surface when snow/ice melts implies a reduction of the upward solar energy flux reflected from the surface available for absorption atmospheric (water vapor) molecules, responsible for a negative the energy flux perturbation in the lowest troposphere.

At the surface, the radiative energy flux perturbation is strongly positive, with values reaching as large as 25 W m^{-2} , which is considerably larger than the energy flux perturbations due to the external forcing and due to atmospheric water vapor change. The location of the maximum energy flux perturbation due to surface albedo feedback at the surface corresponds to the areas of large surface albedo decrease. The shadings in Figure 7.5 shows that the surface albedo decreases the most between 60 and 80 degrees of latitude (up to 0.2) over regions of sea ice, and over regions covered by snows. Compared to the TOA energy flux perturbation (Figure 6.5), the surface shows a very similar pattern, with slightly larger intensity because the reduction in reflected solar radiation at the surface also causes a less absorption of solar energy in the atmosphere.

The vertical and surface profile of the partial temperature change (Figures 7.4b and 7.4d) is calculated by requiring its associated infrared radiation perturbation to balance the perturbation forcing (due to the surface albedo feedback) at each layer using (7.3). The largest temperature change occurs over regions of strong surface energy flux perturbation. At the surface, the albedo feedback generates a warming reaching 8 K, and in the lowest atmospheric levels the warming exceeds 4 K over the southern high latitudes and 3 K over the northern high latitudes. In the lowest troposphere, the warming pattern due to the surface albedo feedback contributes to the large high latitude warming in the GFDL_CM2.0 model $2 \times \text{CO}_2$ simulation (Figure 1.5a). At the surface, the

temperature change over high latitudes resembles strongly the global warming pattern in the GFDL_CM2.0 model $2 \times \text{CO}_2$ simulation (Figure 1.5b), but is slightly stronger. This means that the remaining cloud and dynamical feedbacks discussed in the remaining part of this chapter act to reduce warming in these regions. The globally averaged temperature change at the surface due to the radiative forcing is equal to only 0.47 K, less than half the temperature change due to radiative forcing because it only affects regions where ice and snow melt.

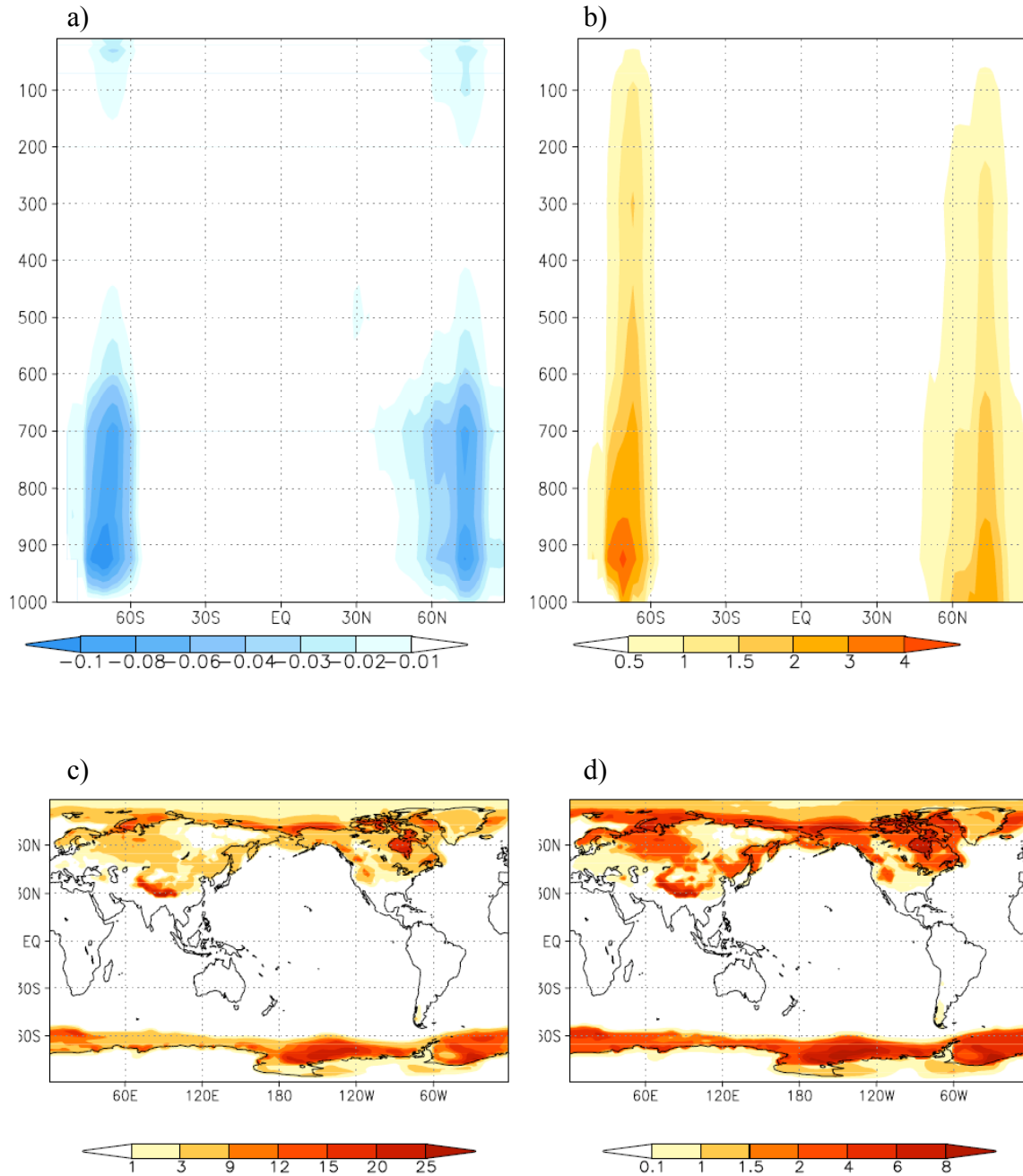


Figure 7.4: Radiative energy flux perturbation (unit: W m^{-2}), and associated partial temperature change (unit: K) due to the surface albedo feedback: zonal and time mean of the vertical profile a) and b), and time mean at the surface c) and d).

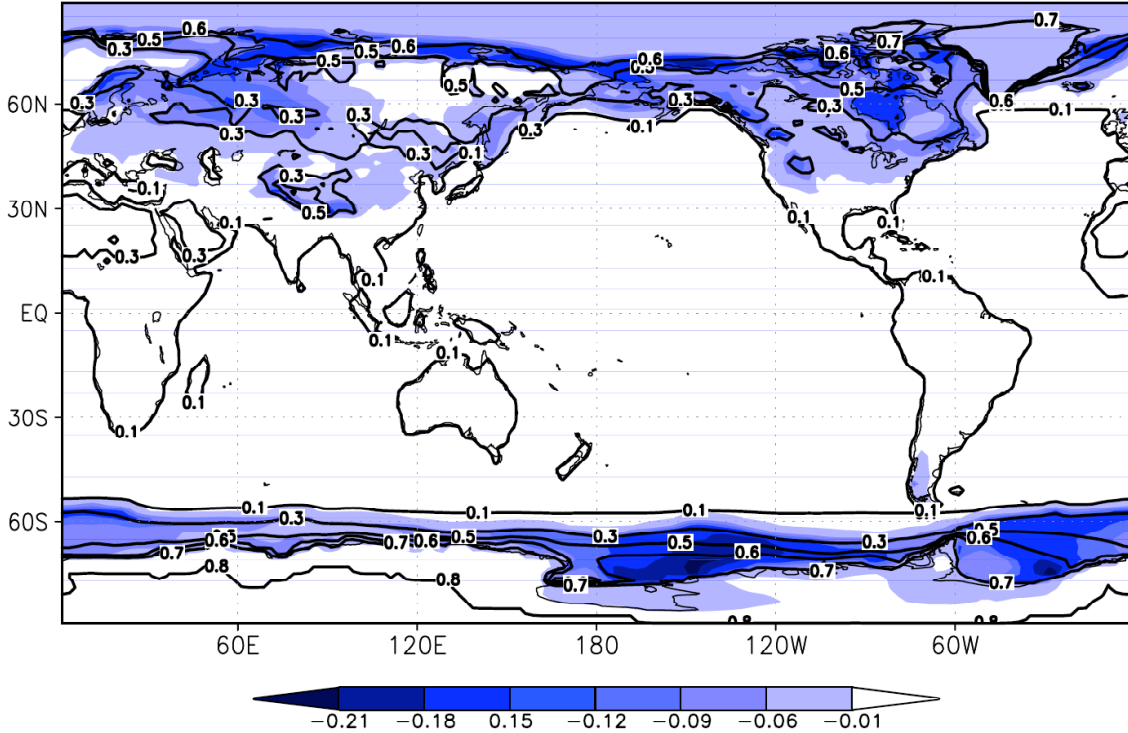


Figure 7.5: Surface albedo (contours), and change in surface albedo in the $2 \times \text{CO}_2$ climate simulation (color shadings).

7.4 Surface turbulent heat flux feedback and its induced temperature change

The surface turbulent heat flux feedback includes the energy flux perturbations due to the change in latent (LH) and sensible (SH) heat fluxes at the surface in response to the doubling of CO_2 . The partial temperature changes associated with the energy flux perturbations due to the surface turbulent heat flux feedback are computed at each atmospheric layer and at the surface as the product of the inverse of the Planck feedback matrix and the energy flux perturbations:

$$\Delta\bar{T}^{(LH)} = \left(\frac{\partial\bar{R}}{\partial\bar{T}} \right)^{-1} \Delta\bar{F}^{(LH)}, \quad \text{and} \quad \Delta\bar{T}^{(SH)} = \left(\frac{\partial\bar{R}}{\partial\bar{T}} \right)^{-1} \Delta\bar{F}^{(SH)} \quad (7.4)$$

where $\Delta\bar{F}^{(LH)}$ and $\Delta\bar{F}^{(SH)}$ are computed using (4.16). The time mean of the surface energy flux perturbations due to the sensible and latent heat flux feedbacks and the sum of both

are displayed in Figures 7.6a, 7.6c, and 7.6e. The associated partial temperature changes at the surface are displayed in Figures 7.6b, 7.6d, and 7.6f.

The surface sensible heat flux results from the exchange of heat between the surface and overlying air when their temperatures are different, and the surface latent heat flux is the exchange of heat due to the phase change of water during evaporation at the interface between air and underlying surface. Both the sensible and latent heat fluxes are in general negative at the surface, meaning that they act to decrease the surface temperature by losing energy to atmosphere, at the exception of the sensible heat flux that is positive over high latitudes. Therefore, a negative energy flux perturbation at the surface acts to dampen the surface warming whereas a positive energy flux perturbation generates an additional surface warming. The energy flux perturbation due to the sensible heat flux feedback is positive over most of the oceans with larger values between 10 and 20 W m⁻² over the Gulf Stream and Kuroshio currents and the Southern Ocean, with the exception of part of the Arctic, and the equatorial pacific oceans (Figure 7.6a). Over land, it is mainly negative with the exception of the equatorial region of Africa and latitudes north of about 50°N. Therefore the sensible heat flux exchange with the atmosphere decreases under external radiative forcing over most of the ocean and increases over land. On the other hand, the energy flux perturbation due to the latent heat flux feedback is negative over most of the ocean, due to the increase in evaporation rate, with the exception of the western equatorial pacific and Arctic Ocean as depicted in Figure 7.6c. Under global warming the evaporation from the ocean is expected to increase thereby increasing the rate of energy loss to the atmosphere by the transfer of latent heat. We refer to the latent heat flux feedback as the evaporation feedback. Maximum negative energy flux perturbation between -10 and -20 W m⁻² is also reached over the Gulf Stream and Kuroshio currents. Over land, the energy flux perturbation shows an opposite pattern to the energy flux perturbation due to the sensible heat flux feedback. It is negative over equatorial Africa and the mid to high latitudes of the northern hemisphere and positive elsewhere. Overall, the energy flux perturbations due to the evaporation and surface sensible flux feedbacks tend to oppose each other (Figure 7.6e). The total energy flux perturbation due to the surface turbulent heat flux is negative over the ocean aside from the Southern Ocean between 45° and 60° S, the equatorial pacific ocean, the Arctic

Ocean and north Atlantic and Pacific oceans. Over land it is mostly negative except over the northeastern part of the Amazon basin, and world deserts. The total energy flux perturbation mostly ranges between -4 and 4 W m⁻², which is of the same order as the energy flux perturbation due to the external radiative forcing and water vapor feedback.

The temperature changes attributable to the surface sensible heat flux feedback (Figure 7.6b) is an increase of warming over most of the latitudes especially over the southern ocean, Gulf Stream and Kuroshio currents up to 3 K. The globally averaged temperature change over the globe is 0.3 K. A reduction of the surface warming occurs over most of the continents as expected from the increase in sensible heat flux over these areas. The temperature response attributable to the evaporation feedback in Figure 7.6d is a reduction of the warming over oceans, except over the western equatorial Pacific Ocean where the evaporation rate decreases. Over the poles, the change in evaporation rate is small and therefore the role of the evaporation feedback is relatively weak over high latitudes. The increase in evaporation rate over equatorial Africa and the mid to high latitudes of the northern hemisphere continents lead to a weakening of the warming, and the decrease in evaporation rate over deserts lead to a stronger surface warming. The effect of this feedback is to decrease the overall surface warming by a global average of -1.2 K, which is stronger than the warming generated by the sensible heat flux feedback. Indeed, Figure 7.6f shows the temperature change induced by the total surface turbulent heat flux feedback reduces the surface warming over most of the ocean and land area. It increases the surface warming over the northern Pacific, Atlantic, and Arctic oceans, the equatorial Pacific and part of the southern ocean. The surface turbulent heat flux feedback therefore helps promote the increased temperature gradient between high and low latitudes seen in Figure 1.5b by damping the surface warming over the tropics with the exception of the western equatorial pacific ocean, and increasing the warming over high latitudes with the exception of the South Pole. The globally averaged temperature change is -0.84 K, which reduces the overall surface warming under external radiative forcing.

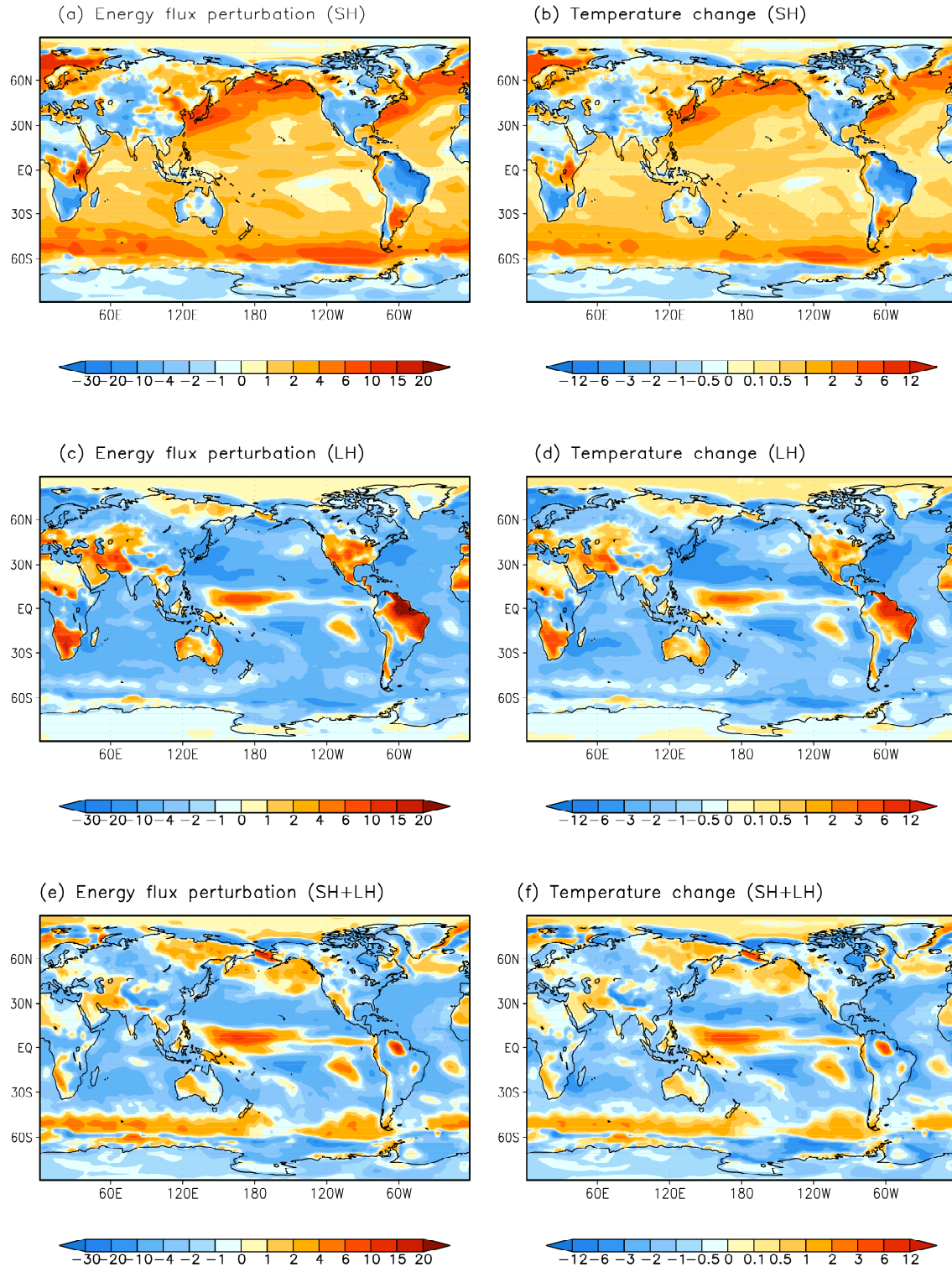


Figure 7.6: (a, c, e) Energy flux perturbations (units W m^{-2}), and (b, d, f) temperature changes (units: Kelvin) at the surface due to surface heat fluxes. Sensible heat flux SH (a-b), latent heat LH (c-d), and sum of both SH+LH (e-f).

7.5 Change in cloud forcing at surface and its induced temperature changes

The partial temperature change associated with the energy flux perturbation due to the surface cloud radiative forcing is computed at each atmospheric layer and at the surface as the product of the inverse of the Planck feedback matrix and the energy flux perturbation:

$$\Delta\bar{T}^{(Cf)} = \left(\frac{\partial\bar{R}}{\partial\bar{T}} \right)^{-1} \Delta\bar{F}^{(Cf)} \quad (7.5)$$

where $\Delta\bar{F}^{(Cf)}$ is computed at the surface as the change in cloud radiative forcing (CRF) directly from the GFDL_CM2.0 climate simulation archive using equation (4.22), and is set to zero in the atmospheric column. The change in surface CRF is plotted in Figure 7.7a, which is identical to Figure 4.3a, and its induced temperature change is plotted in Figure 7.7b. As discussed in chapter 4.3, inferring the change in CRF at the surface from the change in net clear-sky radiation flux and non-radiative energy terms (RHS of equation 4.21) may not agree with the results calculated using (4.22) because of the presence of two types of errors. The first one arises from differences in our clear-sky radiation calculation in comparison with the original GFDL clear-sky radiation calculation (radiation error), and the second one is due to the fact that not all of non-radiative energy terms are included in the GFDL model output archives (missing terms error). Therefore, in addition to calculating the change in surface CRF directly from the GFDL_CM2.0 climate simulation archive (Figure 7.7a), it is important to quantify the errors introduced by using our cloud radiative forcing calculation. The radiation error (Figure 7.7c) is calculated by taking the difference between the inferred change in surface CRF (RHS of 4.21) computed with our clear-sky radiation calculation (Figure 4.3b) and the original GFDL clear-sky radiation calculation (Figure 4.4). The missing terms error (Figure 7.7e) is calculated by taking the difference between the inferred change in surface CRF computed using the original GFDL clear-sky radiation calculation (RHS of 4.21, Figure 4.4) and the change in CRF directly calculated from the GFDL climate simulation archive (Figure 4.3a or Figure 7.7a). The partial temperature changes associated with

these error terms are computed at each atmospheric layer and at the surface as the product of the inverse of the Planck feedback matrix and the energy flux perturbations following the same method as (7.5) with the energy flux perturbations set to zero in the atmospheric column. The time mean of the partial temperature changes associated with the radiation and missing terms errors are plotted in Figure 7.7d and Figure 7.7f respectively.

As discussed in section 4.3, the change in surface CRF (Figure 7.7a) is overall negative with a global average of -1.59 W m^{-2} , therefore acting to decrease the energy flux into the surface layer under radiative forcing. Indeed, because cloud cover increases, incoming solar radiation is more effectively reflected back to space, thus decreasing the amount of solar radiation reaching the surface. The competing greenhouse effect that clouds have on outgoing longwave radiation at the surface is therefore globally weaker. The change in CRF is negative over the equatorial region with a maximum value over 15 W m^{-2} located in the western Pacific Ocean. Positive changes in cloud forcing are encountered around the subtropics in both hemispheres. Maximum values between 9 to 12 W m^{-2} are located over the mid-pacific ocean at 15°S . The Southern Ocean and the Northern hemisphere mid-latitudes display a negative change in cloud forcing along the storm track regions. The location of the energy flux perturbation resembles the distribution of the change in the amount of cloud condensed water (Figure 6.9b). The areas of cloud condensed water increase correspond to a negative change in CRF, owing to the fact that less incoming shortwave radiation is reaching the surface. Over the poles, the changes in CRF and cloud cover are both positive, which means that the increase in cloud cover has a large greenhouse effect and increases the amount of longwave radiation trapped and emitted back to the surface. It dominates over the shortwave effect, which would be small especially in winter when there is no solar radiation reaching the surface. The radiation error introduced in our calculation of the change in surface CRF from the change in net clear-sky radiation flux and non-radiative energy terms together with the clear-sky surface albedo correction term (Figures 7.7c) are mostly within 2 W m^{-2} . Largest errors occur due to missing terms (Figure 7.7e) over high latitudes. These missing non-radiative energy terms include energy loss/gain due to runoff and snow/ice melting.

The temperature change due to the change in surface CRF (Figure 7.7b) follows the distribution of the CRF perturbation. The largest cooling effect occurs where the CRF is the most negative, over the equatorial region, with values reaching -6 K located in the western pacific warm pool. The Southern Ocean and the Northern hemisphere mid-latitudes also display a negative temperature change along the storm track regions. A surface warming is encountered around the subtropics in both hemispheres with a maximum of 5 K located over the mid-pacific at 15°S, and the northern part of South America. Polar regions are also subject to warming of up to 3 K over the North Pole and 2 K over the South Pole, where cloud cover increases. This result is consistent with a study by Holland and Bitz (2003) that found the increases in polar cloud cover to be significantly correlated to amplified Arctic warming. Therefore the change in CRF contributes to the increased temperature gradient between high and low latitudes seen in the total GFDL_CM2.0 temperature change under external radiative forcing (Figure 1.5b) by damping the surface warming over the equatorial region, and increasing the warming over high latitudes. The global average of the surface temperature change is -0.58 K and therefore the change in clouds under radiative forcing acts to decrease the surface warming, along with the change in surface turbulent heat fluxes. The global average is small compared to the temperature change due to external forcing or water vapor feedback, and of the same order as the temperature change due to the surface albedo feedback. Locally, however, it almost cancels out the low latitude warming due to the water vapor feedback or the mid-latitude warming due to the external forcing. Compared to the GFDL original radiation calculations, our offline radiation calculations overestimated the global warming reduction due to surface cloud forcing change by 0.2 K. The global mean temperature changes due to missing terms are small (about -0.01 K), but locally the temperature change due to missing non-radiative energy terms (Figure 7.7f) is large over regions of changes in runoff and snow/ice melting are pronounced.

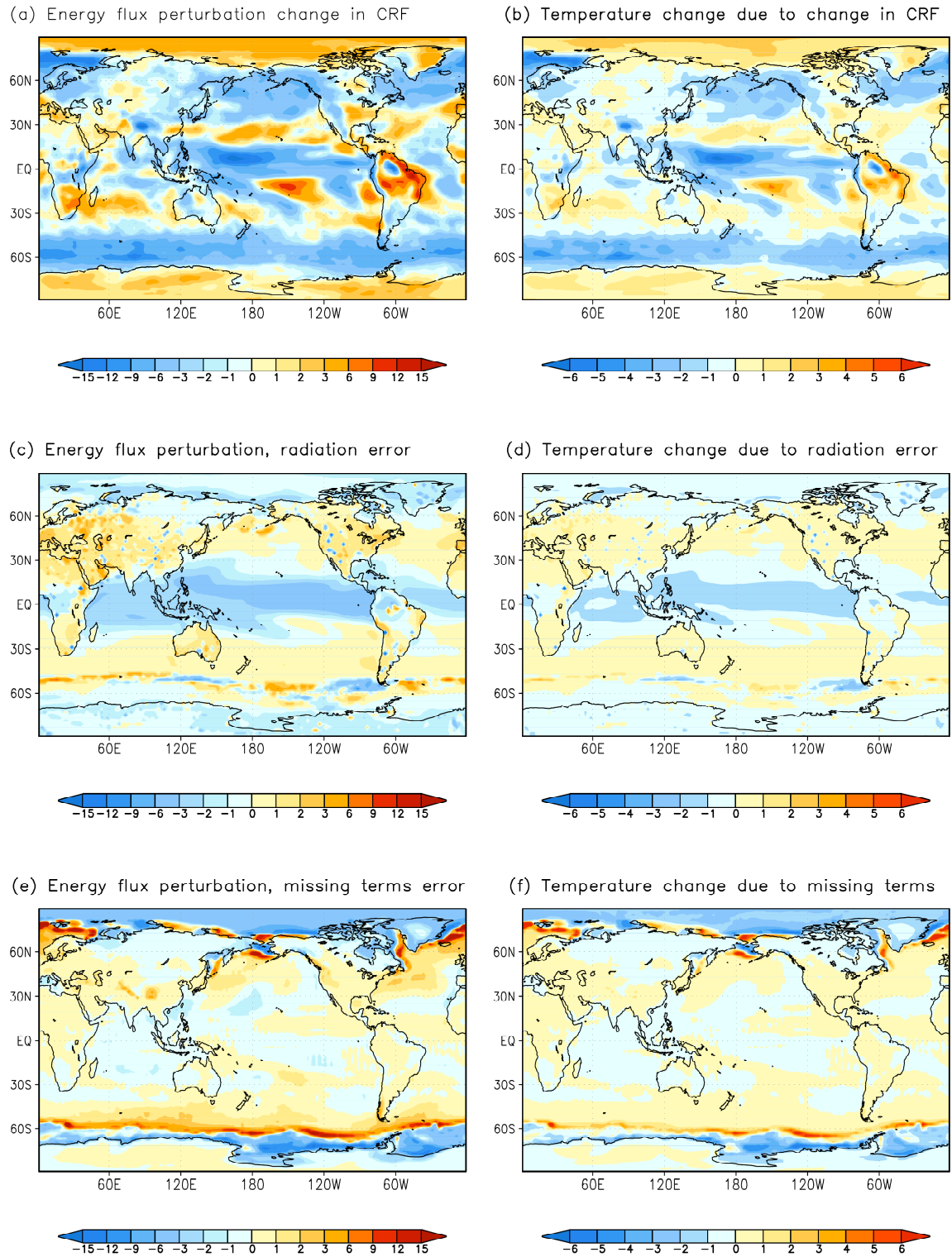


Figure 7.7: (a, c, e) Energy flux perturbation (unit: W m^{-2}), and (b, d, f) temperature change (unit: K) at the surface due to the change in surface CRF (a-b), errors in radiation calculations (c-d), and errors due to missing terms (e-f).

7.6 Sum of cloud forcing change and large scale dynamics, and associated temperature change

The partial temperature change associated with the energy flux perturbation due to the sum of the change in cloud forcing and large-scale dynamics is computed at each atmospheric layer and at the surface as the product of the inverse of the Planck feedback matrix and the energy flux perturbation:

$$\Delta \bar{T}^{(Cf+D)} = \left(\frac{\partial \bar{R}}{\partial \bar{T}} \right)^{-1} \Delta \bar{F}^{(Cf+D)} \quad (7.6)$$

where $\Delta \bar{F}^{(Cf+D)}$ is inferred from the change in net clear-sky radiation flux using (4.15). At the surface, the temperature change associated with the change in surface CRF has been discussed in the previous section, we therefore compute the surface temperature change due to the change in CRF and dynamic feedback in the atmosphere only by setting the energy flux perturbation in (7.6) to zero at the surface. The zonal and time mean of the vertical profile of the radiative energy flux perturbation due to the change in CRF and dynamic feedback and its associated atmospheric temperature change are displayed in Figures 7.8a and 7.8b. The surface temperature change due to the change in CRF and dynamic feedback in the atmosphere only is displayed in Figures 7.8c.

At each atmospheric layer, the dynamic term corresponds to non-radiative energy fluxes that include convective and turbulent energy transport, and poleward energy transport. Although we cannot calculate the feedbacks due to changes in atmospheric circulations and due to changes in CRF separately using the changes in clear-sky radiation, we can still relate the large-scale pattern in Figure 7.8a to the changes in poleward heat transport. In the mid-troposphere, the energy flux perturbation is positive over high latitudes between 700 and 400 hPa reaching 3 W m^{-2} over the northern high latitudes and 2.5 W m^{-2} over the southern high latitudes. In addition, the energy flux perturbation is negative over low latitudes in the lower to mid-troposphere. This pattern suggests an intensification of the poleward transport of energy, leading to an increase in energy flux convergence (divergence) over high (low) latitudes. This corresponds to the large-scale energy flux perturbation pattern discerned at the TOA (Figure 6.6). A study

by Lu and Cai (2009) separated the energy flux perturbation due to local dynamics (sensible heat flux, friction, and vertical convection) from that due to large-scale dynamics (poleward energy transport) in an idealized coupled GCM. They found that the large-scale dynamics are responsible for a dipole pattern over the upper troposphere showing a negative energy flux perturbation over low latitudes and a positive energy flux perturbation over high latitudes. Moreover, a large negative energy flux perturbation in the lower troposphere over the tropics and positive energy flux perturbation above were linked to the intensification of vertical convection. Figure 7.8a also shows a significantly large positive energy flux perturbation (3.5 W m^{-2}) over the equator at 400 hPa and a large area of negative energy flux perturbation reaching 2 W m^{-2} in the atmospheric layers below (from 550 to 800 hPa). This feature is explained by an increase in deep convection over the tropic under external radiative forcing transporting larger amount of energy into the mid to upper-troposphere. Positive energy flux perturbation of 1.5 W m^{-2} is present in the lowest part of the troposphere up to 800 hPa over the equator and up to 900 hPa over higher latitudes. It can be due to the increase in turbulent heat flux removing energy from the surface (Figure 7.6e) and releasing it into the atmosphere. Changes in low-level clouds could also affect the change in the convergence of energy flux into these atmospheric layers by absorbing more shortwave/longwave radiation. Compared to the energy flux perturbation due to the external radiative forcing or water vapor feedback, the energy flux perturbation is of the same order or larger, meaning that the dynamics play an important role redistributing energy in the atmosphere.

The atmospheric temperature change due to the sum of the change in CRF and large-scale dynamics at each atmospheric layer and at the surface is displayed in Figure 7.8b. In the lower part of the troposphere, a large cooling (around -2 K) is found over the equator due to a large enhancement of convection that transports energy in the upper troposphere and effectively cools the lowest part of the troposphere. The energy flux perturbation at the surface due to the change in surface CRF is also largely negative (Figure 7.7a) therefore influencing the cooling pattern in the lower troposphere. Warming occurs over the poles throughout the troposphere with maximum value over 5 K occurring between 500 hPa and 400 hPa, where the atmospheric energy flux perturbation

is the strongest. This pattern is the signature of the strengthening of the poleward transport of energy. Cai and Lu (2009) calculated the atmospheric temperature change due to changes in dynamics in a dry GCM, therefore not including the effect of cloud radiative forcing. They found a dynamic cooling occurring over the low troposphere between 60°S and 60°N, and a dynamic warming over high latitudes with a maximum centered over the equator in the mid-troposphere. The pattern also includes two centers of dynamic cooling in the upper troposphere between 40° and 60° north and south. Our temperature change calculation also shows a 4 K warming over the tropics in the upper troposphere as well as two centers of negative temperature change between 50° and 60° north and south. The temperature change resembles the total GFDL_CM2.0 temperature change pattern under external radiative forcing (Figure 1.5a) with a larger atmospheric warming over high latitudes and a large upper tropospheric warming in the tropics. It also participates in the increase of the atmospheric temperature gradient by reducing the low latitude warming over the tropics. At the surface, the temperature change due to the sum of the change in CRF and large-scale dynamics in the atmosphere only (Figure 7.8c) shows mainly positive values. Even though the energy flux perturbation at the surface (due to change in CRF) is set to zero, the changes in CRF and dynamical feedback in the atmosphere contribute to a surface temperature change. This is because the infrared radiation perturbation associated with the temperature change in the atmospheric column and surface has to balance the atmospheric energy flux perturbation (Figure 7.8a). The impact of the dynamic feedback and change in CRF on the surface temperature is to warm the high latitudes, especially over the South Pole and Greenland, where the warming reaching 2.5 K. Although the dynamic feedback decreases the warming over low latitude in the atmosphere, the surface temperature change is mostly positive there, implying that the change in atmospheric CRF has a competing effect, and warms the surface temperature over low latitudes. Comparing the partial temperature change to the total GFDL_CM2.0 temperature change under external radiative forcing (Figure 1.5b), we notice that the atmospheric CRF and dynamic feedback contribute to the larger high latitude warming. In addition, the regions that show a cooling (over the tropics in the eastern Pacific and Atlantic, and the southern ocean between 120 and 180°E) correspond to locations of weaker warming in Figure 1.5b. The global average of the surface

temperature change is 0.5 K. Even though the role of the change in CRF at the surface is to decrease the surface temperature by -0.58 K the sum of the change in atmospheric CRF and large dynamics have a warming amplification effect.

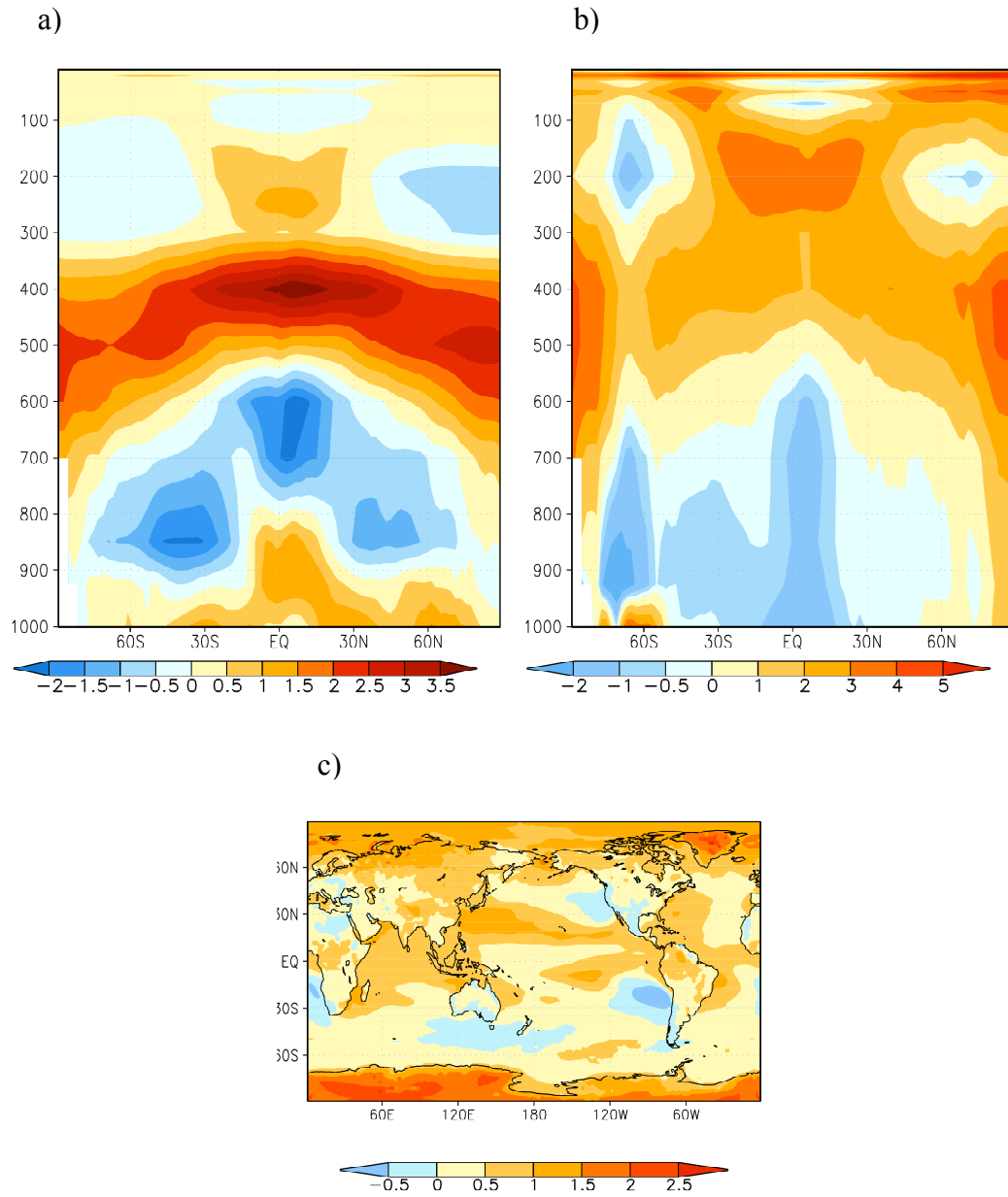


Figure 7.8: Zonal and time mean of energy flux perturbation (a) (unit: W m^{-2}), and associated temperature change (b) (unit: K) due to the sum of the changes in cloud forcing and large-scale dynamics at the surface and atmospheric column. Time mean of the surface temperature change due to the sum of the changes in cloud forcing and large-scale dynamics in the atmosphere only.

7.7 Discussion

We have computed the clear-sky thermodynamic feedbacks and associated partial temperature changes due to the external radiative forcing, changes in water vapor, and surface albedo, as well as the feedbacks and associated partial temperature changes due to changes in surface turbulent heat fluxes, surface cloud feedback, and the sum of the change in cloud forcing and large-scale dynamics. The partial temperature changes calculated at the surface and in the atmosphere add up to the total warming projection due to the doubling of CO₂ following (4.20). Figure 7.9 displays the zonal and time mean average of the temperature change computed from the GFDL_CM2.0 model simulation archive and the sum of the partial temperature changes in the atmospheric column and at the surface. In the atmosphere (Figure 7.9a), the main warming features are respected, with large high latitude warming in the troposphere, and large upper tropospheric warming over the tropics reaching 5 K. The stratospheric cooling is also apparent. At the surface (Figure 7.9b) the difference between the black (GFDL_CM2.0 temperature change) and red line (sum of partial temperature changes) is minimal, reaching a quarter of a degree over high latitudes. Therefore the sum of the partial temperature changes is indeed very close to the GFDL_CM2.0 temperature change, which confirms that the partial temperature changes are indeed addable.

The globally averaged partial temperature changes due to external radiative forcing and subsequent feedbacks (water vapor, surface albedo, surface turbulent heat flux, and surface cloud feedbacks, and the sum of the change in atmospheric cloud forcing and large-scale dynamics) are listed in Table 7.1. Again, the sum of the partial temperature changes (2.94 K) is very close to the global average of temperature change computed from the GFDL_CM2.0 model simulation archive (2.93 K). The water vapor feedback is the largest contributor to the global surface warming (2.53 K) by more than twice the amount of warming due to radiative forcing alone (1.08 K). The surface albedo feedback and change in surface cloud radiative forcing both generate a warming of 0.47 K. On the other hand, the change in atmospheric cloud forcing and large-scale dynamics contribute to damping the surface warming by -0.77 K. Finally, the surface turbulent heat flux feedback also contribute to cooling the surface by -0.84 K.

Table 7.1: Globally averaged partial temperature changes at the surface (units: Kelvin).

$\Delta\bar{T}^{(CO_2)}$	$\Delta\bar{T}^{(h_2o)}$	$\Delta\bar{T}^{(\alpha)}$	$\Delta\bar{T}^{(LH)} + \Delta\bar{T}^{(SH)}$	$\Delta\bar{T}^{(Cf_surface)}$	$\Delta\bar{T}^{(Cf+D)_atmosphere}$
1.08 K	2.53 K	0.47 K	-0.84 K	-0.77 K	0.47 K

We now look separately at the partial temperature change contributions of the clear-sky radiative flux perturbations and the sum of the dynamical energy perturbations and change in CRF to the total temperature change. Figure 7.10 displays on the left panel the zonal and time mean of the sum of the partial temperature changes due to clear-sky radiative flux perturbations (external radiative forcing, water vapor feedback, surface albedo feedback) in the atmospheric column (Figure 7.10a) and at the surface (Figure 7.10c). The right panel represents the zonal and time mean of the partial temperature change due to the sum of dynamical energy perturbations (surface turbulent heat flux feedback, large scale dynamics and convection), and change in CRF in the atmospheric column (Figure 7.10b) and at the surface (Figure 7.10d). A striking feature is the apparent negative correlation between the two temperature change terms in the lower troposphere and at the surface, with the exception of high latitudes. The changes in energy transport therefore helps to redistribute the energy in the atmosphere, which reduces the large warming induced by the radiative flux perturbations in the lower troposphere and at surface in the tropics. Indeed, over low latitudes the warming due to radiative flux perturbations, mainly resulting from the water vapor feedback, reaches 5 K at the surface and atmospheric column. It is partially reduced by the 2.5K cooling in the atmospheric column and 2 K cooling at the surface induced by the dynamical energy perturbations and change in CRF. In addition, regions comprised between 70° and 80° of latitude, which show a large warming at the surface and lower troposphere (Figure 7.10a and c) mainly induced by the surface albedo feedback, display a strong cooling partially due to the surface turbulent heat flux feedback and changes in surface CRF (see Figures 7.6f and 7.7b). Over high latitudes, both the radiative flux perturbations and the sum of the dynamical energy perturbation and change in CRF contribute to the warming. A larger warming is induced bellow 700 hPa by the radiative flux perturbations, and a larger warming is induced from 700 hPa to 300 hPa by the dynamical energy perturbations and change in CRF. At the surface, for latitudes poleward of 80 degrees, the radiative flux

perturbations generate a larger warming over the north pole (5.25 K) than the south pole (2.75 K), whereas the sum of the dynamical energy perturbation and change in CRF generate a larger warming over the south pole (1.25 K) than the north pole (0.75 K). In comparison with Figure 7.9a, in the atmospheric column, we notice that the temperature changes due to both radiative and non-radiative feedbacks contribute to the large upper tropospheric warming over the tropics. Finally, the tropospheric cooling is due to the radiative flux perturbation, specifically the external radiative forcing.

The zonal mean of the partial surface temperature changes and their sum as well as the total temperature change derived from the GFDL_CM2.0 are plotted in Figure 7.11. It is seen that over low latitudes the warming due to radiative flux perturbations described in Figure 7.10 c, results almost entirely from the water vapor feedback (Figure 7.11b), which is responsible for 4.25 K warming out of a total of 5 K. The only other process generating a warming over low latitude is the external forcing (Figure 7.11a), but it is much smaller, around 0.75 K over the equator. In high latitudes, the radiative flux perturbations due to the external forcing, water vapor and surface albedo feedback all participate in increasing the surface warming. Regions comprised between 70° and 80° of latitude, show the largest warming induced by the surface albedo feedback reaching 5 K (Figure 7.11c). The sum of the change in cloud radiative forcing and large-scale dynamics also contribute to the large high latitude warming by 2.5 K and 0.75 K over the South Pole and North Pole respectively. However, the sum of these two processes generates a cooling over most of the globe. Over equatorial regions the large-scale dynamics transport heat poleward, and the surface temperature decreases by 2.5 K. Over 60° to 70° of latitude the cooling reaches 4.5 K due to an increase in cloud cover over this region. The other process leading to a damping of the surface warming is the surface turbulent heat flux feedback. The cooling is the strongest between 10° and 30° of latitude where it almost reaches 0.4 K.

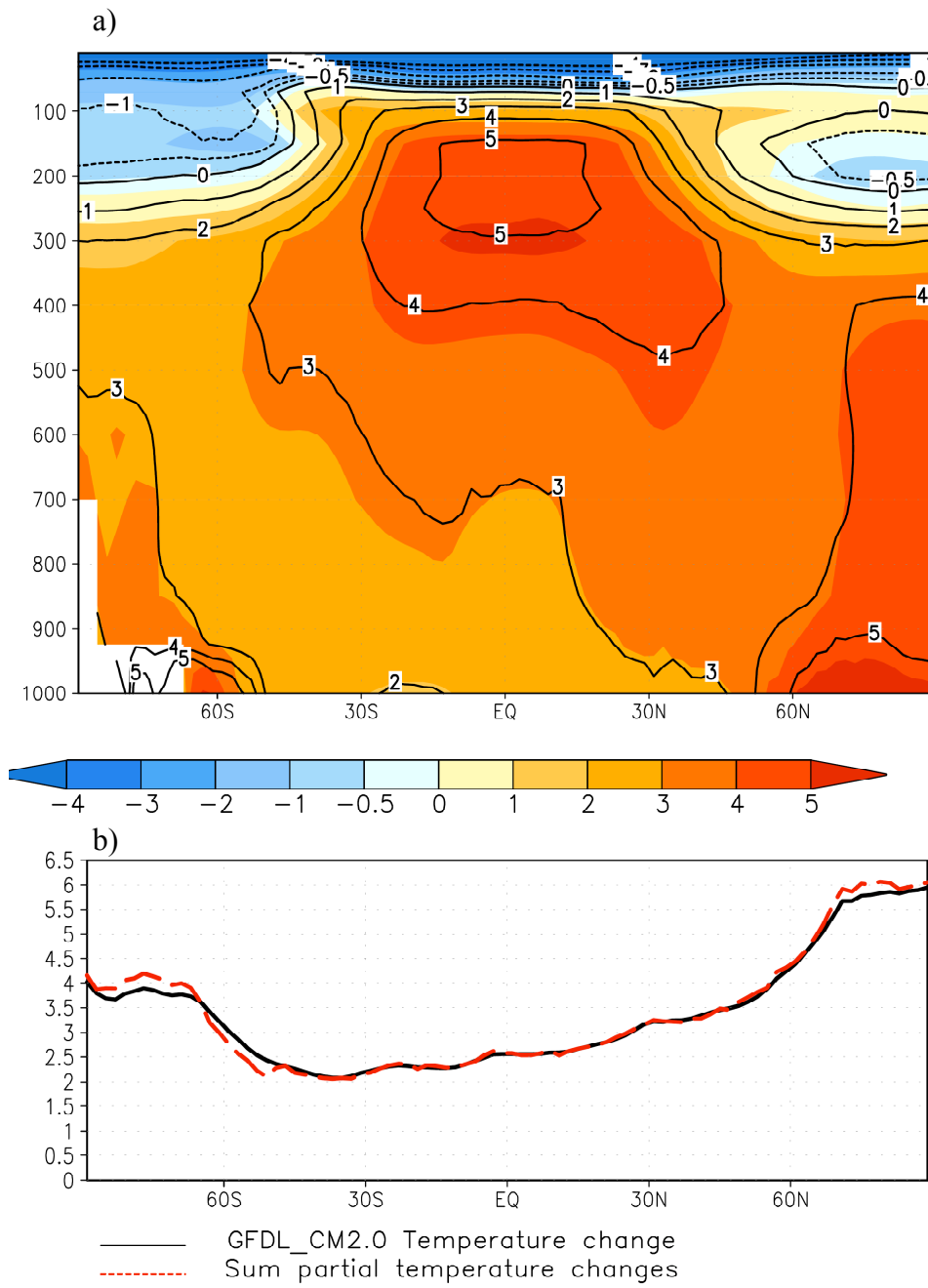


Figure 7.9: Zonal and time mean of the total temperature change from the GFDL_CM2.0 model simulation, and the sum of the partial temperature changes: a) in the atmospheric column and b) at the surface. Color shadings and black line represent the GFDL_CM2.0 temperature change, black contours and red dotted line represent the sum of the partial temperature changes (units: Kelvin).

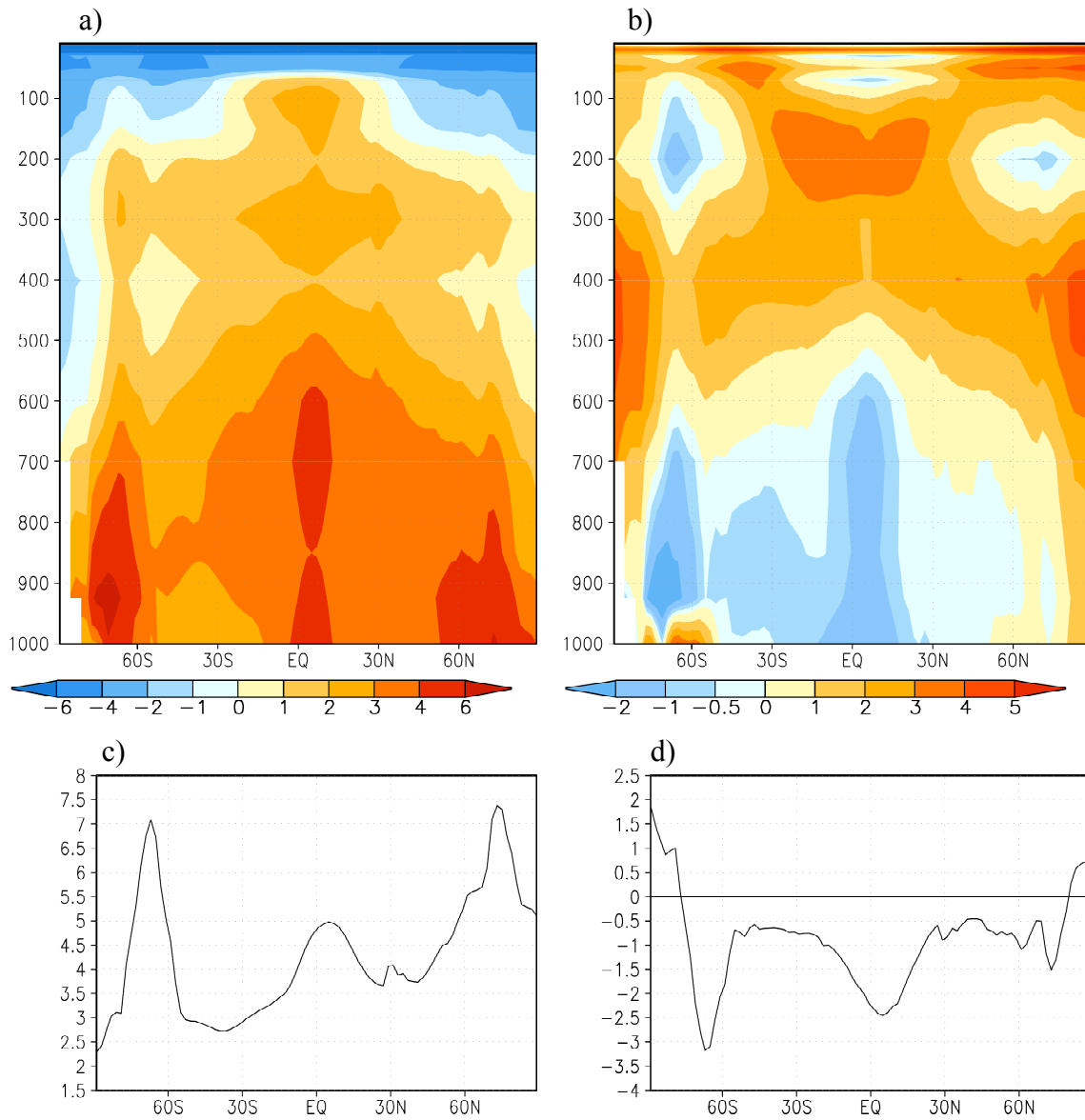


Figure 7.10: Zonal and time mean in the atmospheric column (a-b) and at the surface (c-d). Left panels: sum of the partial temperature changes due to clear-sky radiative flux perturbations (radiative forcing, water vapor feedback, surface albedo feedback). Right panels: partial temperature change due to the sum of dynamical energy perturbations (surface turbulent heat flux feedback, large scale dynamics and convection), and change in CRF in the atmospheric column and at the surface (units: Kelvin).

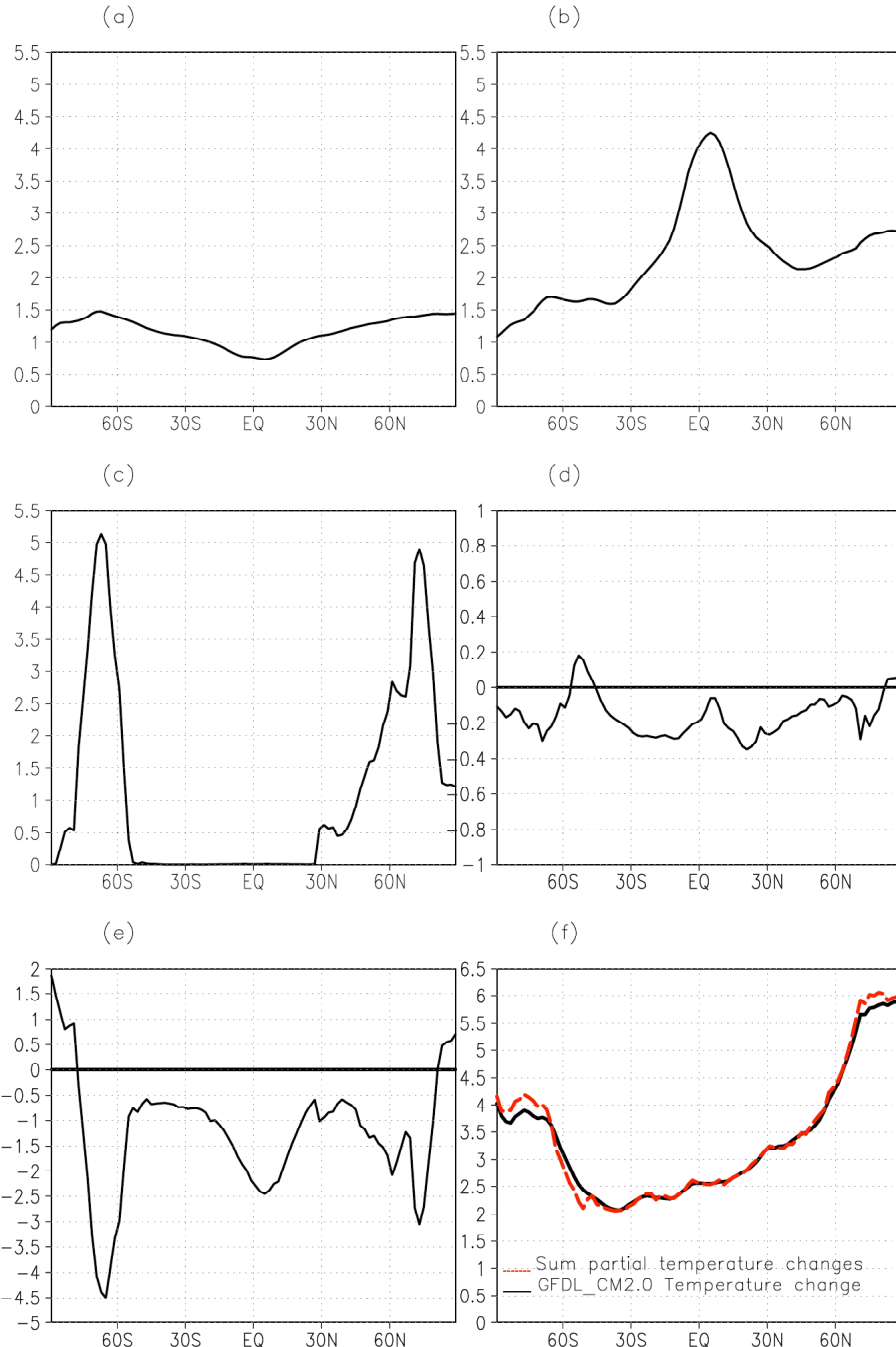


Figure 7.11: Zonal and time mean of the surface partial temperature changes due to a) radiative forcing, b-d) water vapor , surface albedo, and surface turbulent heat flux feedback, and e) sum of the large scale dynamics, convection and change in CRF. f) sum of (a-e) (red dash line), and GFDL_CM2.0 temperature change (black line). (Units: Kelvin).

CHAPTER 8

CONCLUSIONS

The most current version of general circulation models depicts the current observed warming pattern with a good level of accuracy, but uncertainties in modeling the intensity of future climate change remain a concern. Both external radiative forcing and feedbacks play an important role in controlling the atmospheric and surface temperature, and uncertainties in future climate projections stem in part from the lack of understanding of climate feedback processes. In light of the importance of feedback processes in future climate projection, the goal of this dissertation was to improve the physical understanding of feedback processes, and determine the contribution of the external radiative forcing and individual feedback processes to the GFDL_CM2.0 global warming simulation pattern. This was achieved by computing the clear-sky thermodynamic feedbacks due to the external radiative forcing, changes in water vapor, and surface albedo, as well as the feedbacks due to changes in surface turbulent heat fluxes, surface cloud feedback, and the sum of the change in cloud forcing and large-scale dynamics, at the TOA and at each atmospheric layer and the surface. Then the partial temperature changes associated with each of these individual energy flux perturbations were calculated using CFRAM, a new coupled atmosphere-surface climate feedback response-analysis method. These partial temperature changes are additive and their sum similar to the temperature change produced by the original GFDL_CM2.0 global warming simulation, as seen in Figure 7.9.

The net change in energy input to the climate system due the external forcing and individual energy flux perturbation at the TOA was calculated. On a global average, the water vapor feedback is the strongest positive feedback under doubling of CO₂ (Table 6.1). The next important contributor to the positive radiative energy flux perturbation at the TOA is the external radiative forcing, followed by the albedo feedback and the cloud forcing. Each feedback has an overall positive value indicating that the climate system

gains more energy when CO₂ is doubled, reinforcing the initial climate forcing. This requires the climate system to warm further to balance the extra energy entering the system by the extra outgoing radiation emitted by the warmer climate. Geographically, the doubling of CO₂ alone acts to trap more thermal energy in the tropics where the mean temperature is warmer. The water vapor feedback is the strongest over the equator where the change in the atmospheric specific humidity is the largest. The albedo feedback is the strongest feedback above 60° of latitude over regions of sea ice and snow melting. The pattern of the energy flux perturbation due to the sum of the change in cloud forcing and dynamical feedback show an increase in the convergence (divergence) of heat over high (low) latitudes. The geographical distribution of the change in CRF at the TOA is complex, with a positive global average meaning that the change in CRF generates a net increase of energy in the climate system.

The vertical and surface distribution of the energy flux perturbations due to the radiative forcing and subsequent feedbacks gives additional details to the TOA feedback analysis. The radiative forcing in the atmosphere shows two maxima located between 900 and 800 hPa over the extratropics, away from the competing greenhouse effect of water vapor. At the surface the energy flux perturbation is the largest over high latitudes, regions of high elevations, and deserts, corresponding to regions of minimum water vapor concentration in the mean state. The larger values of the energy flux perturbation due to the water vapor feedback are located in the lower part of the troposphere, where the largest change in water vapor occurs, and at the surface. It is negative over a large portion of the atmosphere and positive at the surface. It is also much larger than the energy flux perturbation due to the external radiative forcing over the tropics and also over the northern high latitudes. The radiative energy flux perturbation due to the surface albedo feedback is largely positive at the surface is very small and negative in the lowest part of the atmosphere over regions where snow and ice are melting or the form of precipitation changes from snow to rain. This is because the increase in shortwave radiation absorbed at the surface when snow/ice melts implies a reduction of the upward solar energy flux reflected from the surface. Locally, the surface albedo feedback contributes to a much larger energy flux perturbation than the external radiative forcing or water vapor

feedback. Overall, the energy flux perturbations due to the evaporation and surface sensible flux feedbacks tend to oppose each other and the total energy flux perturbation is negative over large portion of the globe. This translates an overall increase in the transfer of energy from the surface to the atmosphere under external radiative forcing. The change in surface CRF is overall negative, therefore acting to decrease the energy flux into the surface layer under radiative forcing. Because cloud cover generally increases under external radiative forcing, incoming solar radiation is more effectively reflected back to space, thus decreasing the amount of solar radiation reaching the surface. The competing positive greenhouse effect that clouds have on outgoing longwave radiation at the surface is generally weaker except over the poles, where both the changes in CRF and cloud cover are positive. In the atmosphere the positive (negative) energy flux perturbation over high (low) latitudes due to the sum of the change in cloud forcing and large-scale dynamics suggests an intensification of the poleward transport of energy. An increase in deep convection over the tropic under external radiative forcing transporting more energy into the mid to upper-troposphere is found to be responsible for a large vertical dipole over the equator. The dynamics play an important role redistributing energy in the atmosphere.

The study of the partial temperature change contributions due to the external radiative forcing and each feedback explains the global warming pattern present in the GFDL_CM2.0 global warming simulation. The water vapor feedback is the largest contributor to the globally averaged surface warming. It is twice as large as the warming due to the radiative forcing alone. The surface albedo feedback and change in surface cloud radiative forcing increase the surface temperature by the same amount that is smaller than the warming due to the external radiative forcing. On the other hand, the change in atmospheric cloud forcing and large-scale dynamics contribute to an overall damping the surface warming. The surface turbulent heat flux feedback also act to cool the surface temperature. In the atmosphere, it appears that the changes in energy transport and CRF helps redistribute the energy, which reduces the large warming induced by the radiative flux perturbations. Over low latitudes, the warming due to radiative flux perturbations mainly results from the water vapor feedback. It is partially reduced by the

cooling induced by the dynamical energy perturbations and change in CRF. In addition, the large warming at the surface and lower troposphere induced by the surface albedo feedback is also partially counteracted by a strong cooling due to the surface turbulent heat flux feedback and changes in surface CRF. Over high latitudes, both the radiative flux perturbations and the sum of the dynamical energy perturbation and change in CRF contribute to the global warming pattern. The temperature changes due to both radiative and non-radiative feedbacks contribute to the large upper tropospheric warming over the tropics. The tropospheric cooling is due to the external radiative forcing.

APPENDIX A

GFDM_CM2.0 MODEL CHARACTERISTICS

Delworth et al. (2006) in the first part of a four papers series describes the formulation of the model. The model includes atmosphere, land, and sea-ice component models coupled together and with a slab ocean using a flux coupler module that passes fluxes between the component models. The atmosphere and land components are documented in GFDL (2004). In summary, the atmospheric component has 24 vertical levels, uses 3-h time step for atmospheric radiation and a 0.5-h time step for other atmospheric physics, and includes a diurnal cycle of insolation. It also uses a B-grid dynamical core. The well-mixed greenhouse gases, tropospheric and stratospheric ozone, natural and anthropogenic aerosols, and solar irradiance are specified. The indirect effects of aerosols are omitted by having no direct interaction with the cloud scheme. Surface fluxes are computed using Monin-Obukhov similarity theory, given the model's lowest level wind, temperature, and humidity, and the surface roughness lengths, temperature, and humidity. The land model includes three water reservoirs: snowpack, soil water and ground water, and has 18 levels used for heat storage. A river routing scheme where freshwater is injected into the model ocean is incorporated. The land cover consists of 10 different vegetation or land surface types. The sea ice component is a dynamical model with three vertical layers, one snow and two ice, and five ice thickness categories. The ice internal stresses are calculated using an elastic-viscous-plastic technique, and the thermodynamics is a modified Semtner three-layer scheme.

The following paragraph describes the simulations characteristics as taken from the NetCDF data description files. The initial conditions for the control experiment were derived from a multi-step process. First, a restoring run version of the model was spun up (SST, sea ice concentration and thicknesses restored toward observation-based values) and Q -flux adjustments diagnosed. The control experiment was then initialized from the end of the restoring run, and the Q -flux adjustments applied. The control climate was integrated for 100 years, but years 1 to 50 are not analyzed because they may contain

slight drift. Forcing agents generally consistent with year 1990 or late 20th century conditions were applied to the model and include the well-mixed greenhouse gases (CO_2 , CH_4 , N_2O), tropospheric and stratospheric O_3 , tropospheric sulfates, black and organic carbon, dust, sea salt, solar irradiance, and the distribution of land cover types. The direct effect of tropospheric aerosols is calculated by the model, but the indirect effects are not. The initial conditions for the $2 \times \text{CO}_2$ experiment were derived from 1 January year 101 of the control experiment. Atmospheric CO_2 levels were instantaneously doubled at the beginning of this experiment and held constant for the 100-year duration of the experiment.

APPENDIX B

DATA MANIPULATION AND QUALITY CONTROL

Annual average at the lowest standard pressure levels:

The last 13 years of the GFDL_CM2_0 model data sets are averaged over each month. The variables defined on 17 pressure levels (temperature, specific humidity and ozone) include undefined data points between 1000 hPa and 600 hPa where the surface pressure is lower than the pressure level due to high topography (e.g. sea ice elevation). The location of undefined data points varies over the years for each month, so in order to keep the maximum data coverage at the lowest level, the annual average is performed at each grid point in which at least 1 month of data is available at that grid point.

Radiative energy flux calculation:

After the annual cycle is preformed, the location of defined and undefined data at the lowest atmospheric level also varies between the $2 \times \text{CO}_2$ and control simulation due to surface pressure changes. It causes a problem when calculating the atmospheric radiative energy flux using the $2 \times \text{CO}_2$ specific humidity but $1 \times \text{CO}_2$ temperature and ozone profile. In order to palliate this problem, when the $2 \times \text{CO}_2$ specific humidity is undefined but the other ($1 \times \text{CO}_2$) variables are defined, the $2 \times \text{CO}_2$ specific humidity is replaced by its $1 \times \text{CO}_2$ value.

Energy flux perturbation:

Then when calculating energy flux perturbations, if at the lowest pressure level the baseline radiative energy flux is defined but the perturbed radiative energy flux is undefined, then the energy flux change is set to zero. If the baseline radiative energy flux is undefined then the energy flux change set to an undefined value.

Inconsistencies with pressure levels and surface pressure:

The lowest pressure level containing data is expected to have one more layer, the surface layer, underneath it. The annual mean of the surface pressure is sometimes above the

standard pressure at that lowest level. This inconsistency is eliminated by forcing the surface pressure to be 1hPa larger than the standard pressure of the lowest level.

Another issue is encountered where the lowest standard pressure level has a missing data even though the surface layer underneath is bellow this pressure level. In order to retrieve data at that location we use the following interpolation technique between the surface data and the layer above the lowest standard pressure level. The temperature (T) varies logarithmically with height, not the pressure (P):

$$T = T_b \left(\frac{P_b + P_t}{2P_b} \right)^\beta . \beta = \frac{\ln \frac{T_b}{T_t}}{\ln \frac{P_b}{P_t}}$$

b stands for the lowest level which is the surface layer and t is the standard pressure level that is just above the lowest standard pressure level.

We also interpolate the pressure level temperature and specific humidity at every grid point to obtain the temperature and specific humidity inside the atmospheric layers.

REFERENCES

- Alexeev, V. A., P. L. Langen, J.R., Bates, 2005: Polar amplification of surface warming on an aquaplanet in “ghost forcing” experiments without sea ice feedbacks. *Climate Dynamics.* 24, 655-666.
- Allen, R.J., and S. C. Sherwood, 2008: Warming maximum in the tropical upper troposphere deduced from thermal winds. *Nature Geoscience.* 1, 399-403.
- Allison, I., and M. Beland (co-Chairs), 2009: The state of polar research. A Statement from the International Council for Science/World Meteorological Organization Joint Committee for the International Polar Year 2007-2008.
- Bony, S., R. Colman, V.M. Kattsov, R.P. Allan, C.S. Bretherton, J.-L. Dufresne, A. Hall, S. Hallegatte, M.M. Holland, W. Ingram, D.A. Randall, B.J. Soden, G. Tselioudis, and M.J. Webb, 2006: How Well Do We Understand and Evaluate Climate Change Feedback Processes? *J. Climate,* 19, 3445–3482.
- Bony, S., and J.-L. Dufresne, 2005: Marine boundary layer clouds at the heart of tropical cloud feedback uncertainties in climate models. *Geophys. Res. Lett.*, 32, L20806, doi:10.1029/2005GL023851.
- Budyko, 1969: The effect of solar radiation variations on the climate of the earth. *Tellus XXI*, 5, 39-692891.
- Cai, M., 2005: Dynamical amplification of polar warming. *Geophys. Res. Lett.*, 32, L22710, doi: 10.1029/2005GL024481.
- Cai, M., 2006: Dynamical greenhouse-plus feedback and polar warming amplification. Part I: A dry radiative-transportive climate model. *Clim Dyn.*, 19, 661-675.
- Cai, M., J-H. Lu, 2007: Dynamical greenhouse-plus feedback and polar warming amplification. Part II: Meridional and vertical asymmetries of the global warming. *Clim Dyn.*, 29, 375-391.
- Cai, M., J-H. Lu, 2008: A new framework for isolating individual feedback processes in coupled general circulation climate models. Part II: Method demonstrations and comparisons. *Clim. Dyn.*, Doi: 10.1007/s00382-008-0424-4.
- Castet, C., 2005: Footprint of the dynamical amplifier of global warming and attribution of model’s uncertainties. M.S. Thesis, Department of Meteorology, Florida State University, 48.

Castet, C., and M. Cai, 2007: Warming Asymmetries due to Surface Turbulent Heat Flux Feedbacks in IPCC AR4 Climate Simulations. Poster AGU Fall Meeting 2007. GC21A-0161.

Cess, R.D., and G.L. Potter, 1988: A methodology of understanding and intercomparing atmospheric climate feedback processes in general circulation models. *J. Geophys. Res.*, 93, 8305-8314.

Cess, R. D., et al., 1990: Intercomparison and Interpretation of Climate Feedback Processes in 19 Atmospheric General Circulation Models. *J. Geophys. Res.*, 95(D10), 16, 601–16,615.

Cess, R.D., et al., 1996: Cloud feedback in atmospheric general circulation models: An update, *J. Geophys. Res.*, 101(D8), 12,791-12,794.

Chapman, W.L., and I.E. Walsh, 1993: Recent variations of sea ice and air temperature in high latitudes. *Bull. Amer. Meteor. Soc.*, 74, 33-47.

Collins, W. D., et al., 2006: Radiative forcing by well-mixed greenhouse gases: Estimates from climate models in the Intergovernmental Panel on Climate Change (IPCC) Fourth Assessment Report (AR4). *J. Geophys. Res.*, 111, D14317, doi:10.1029/2005JD006713.

Colman, R., 2003: A comparison of climate feedbacks in general circulation models. *Climate Dyn.*, 20, 865-873.

Comiso, J.C., C.L. Parkinson, 2004: Satellite observed changes in the Arctic. *Phys. Today*, 57, 38-44.

Delworth, T.L., A.J. Broccoli, A. Rosati, R.J. Stouffer, V. Balaji, J.A. Beesley, W.F. Cooke, K.W. Dixon, J. Dunne, K.A. Dunne, J.W. Durachta, K.L. Findell, P. Ginoux, A. Gnanadesikan, C.T. Gordon, S.M. Griffies, R. Gudgel, M.J. Harrison, I.M. Held, R.S. Hemler, L.W. Horowitz, S.A. Klein, T.R. Knutson, P.J. Kushner, A.R. Langenhorst, H.C. Lee, S.J. Lin, J. Lu, S.L. Malyshev, P.C.D. Milly, V. Ramaswamy, J. Russell, M.D. Schwarzkopf, E. Shevliakova, J.J. Sirutis, M.J. Spelman, W.F. Stern, M. Winton, A.T. Wittenberg, B. Wyman, F. Zeng, and R. Zhang, 2006: GFDL's CM2 Global Coupled Climate Models. Part I: Formulation and Simulation Characteristics. *J. Climate*, 19, 643–674.

Dufresne J.-L., S. Bony, 2008: An Assessment of the Primary Sources of Spread of Global Warming Estimates from Coupled Atmosphere-Ocean Models. *Journal of Climate* 21(19), 5135.

Forster, P., V. Ramaswamy, P. Artaxo, T. Berntsen, R. Betts, D.W. Fahey, J. Haywood, J. Lean, D.C. Lowe, G. Myhre, J. Nganga, R. Prinn, G. Raga, M. Schulz and R. Van Dorland, 2007: Changes in Atmospheric Constituents and in Radiative Forcing. In: *Climate Change 2007: The Physical Science Basis. Contribution of Working Group I to*

the Fourth Assessment Report of the Intergovernmental Panel on Climate Change [Solomon, S., D. Qin, M. Manning, Z. Chen, M. Marquis, K.B. Averyt, M.Tignor and H.L. Miller (eds.)]. Cambridge University Press, Cambridge, United Kingdom and New York, NY, USA.

Frankignoul, C., E. Kestenare, M. Botzet, A.F. Carril, H. Drange, A. Pardaens, L. Terray, R. Sutton, 2004: An intercomparison between the surface heat flux feedback in five coupled models, COADS and the NCEP reanalysis. *Climate Dyn.*, 22, 373-388.

Fu, Q., P. Yang, and W. B. Sun., 1998: An accurate parameterization of the infrared radiative properties of cirrus clouds for climate models. *J. Clim.*, 11, 2223-2237.

Fu, Q., K.N. Liou, 1993: Parameterization of the radiative properties of cirrus clouds. *J. Atmos. Sci.*, 50, 2008-2025.

GFDL Global Atmospheric Model Development Team, 2004: The new GFDL global atmosphere and land model AM2-LM2: Evaluation with prescribed SST simulations. *J. Climate*, 17, 4641-4673.

Gleckler, P. J., K. E. Taylor, and C. Doutriaux, 2008: Performance metrics for climate models. *J. Geophys. Res.*, 113, D06104, doi:10.1029/2007JD008972.

Graversen R.G., et al., 2008: Vertical structure of recent Arctic warming. *Nature*, 06502, vol 541. Doi 10.1038.

Gregory, J. M., W. J. Ingram, M. A. Palmer, G. S. Jones, P. A. Stott, R. B. Thorpe, J. A. Lowe, T. C. Johns, and K. D. Williams, 2004: A new method for diagnosing radiative forcing and climate sensitivity. *Geophys. Res. Lett.*, 31, L03205, doi:10.1029/2003GL018747.

Hall A., and Manabe S., 1999: The role of water vapor feedback in unperturbed climate variability and global warming. *J. Climate*, 12, 2327-2346.

Hall, A., 2004: The role of surface albedo feedback in climate. *J. Clim.*, 17, 1550-1568.

Hansen, J., et al., 1998: Climate forcings in the Industrial era. *Proc. Natl. Acad. Sci.*, Vol. 95, pp. 12753-12758.

Hansen, J., et al., 2002: Climate forcings in Goddard Institute for Space Studies SI2000 simulations. *J. Geophys. Res.*, 107(D18), 4347, doi:10.1029/2001JD001143.

Hansen, J., Mki. Sato, R. Ruedy, K. Lo, D.W. Lea, and M. Medina-Elizade, 2006: Global temperature change. *Proc. Natl. Acad. Sci.*, 103, 14288-14293, doi:10.1073/pnas.0606291103.

- Hare, W., 2003: Assessment of knowledge on impact of climate change. German Advisory Council on Global Change, Berlin.
- Hartmann, D. L., 1994: Global Physical Climatology. Academic Press, 411 pp.
- Hassol, S.J., 2004: Impact of a warming Arctic: Arctic climate impact assessment. Cambridge University Press. Cambridge, 146pp.
- Hegerl, G.C., F. W. Zwiers, P. Braconnot, N.P. Gillett, Y. Luo, J.A. Marengo Orsini, N. Nicholls, J.E. Penner and P.A. Stott, 2007: Understanding and Attributing Climate Change. In: Climate Change 2007: The Physical Science Basis. Contribution of Working Group I to the Fourth Assessment Report of the Intergovernmental Panel on Climate Change [Solomon, S., D. Qin, M. Manning, Z. Chen, M. Marquis, K.B. Averyt, M. Tignor and H.L. Miller (eds.)]. Cambridge University Press, Cambridge, United Kingdom and New York, NY, USA.
- Held, M., and B. Soden, 2000: Water vapor feedback and global warming. *Annu. Rev. Energy Environ.*, 25, 441-75.
- Holland, M.M., C.M. Bitz, 2003: Polar amplifications of climate change in coupled models. *Clim, Dyn.*, 21, 221-232.
- Intergovernmental Panel on Climate Change (IPCC), 2001: Climate Change 2001: The Scientific Basis. Edited by J. T. Houghton et al., 944 pp, Cambridge Univ. Press, New York.
- Jacob, D.J., et al., 2005: Radiative Forcing of Climate Change: Expanding the Concept and Addressing Uncertainties. The National Academies Press, Washington, DC, 207pp.
- Johannessen, O.M., et al., 2004: Arctic climate change: observed and modelled temperature and sea-ice variability. *Tellus*, 56A, 32-341.
- Jones, P.D., M. New, D.E. Parker, S. Martin, and I.G. Rigor, 1999: Surface air temperature and its changes over the past 150 years. *Rev. Geophys.*, 37, 173.
- Jones P. D., and A. Moberg, 2003: Hemispheric and large-scale surface air temperature variations: an extensive revision and an update to 2001. *J. Climate*, 16, 206-223.
- Kalnay, E., M. Kanamitsu, R. Kistler, W. Collins, D. Deaven, L. Gandin, M. Iredell, S. Saha, G. White, J. Woollen, Y. Zhu, A. Leetmaa, R. Reynolds, M. Chelliah, W. Ebisuzaki, W. Higgins, J. Janowiak, K. Mo, C. Ropelewski, J. Wang, R. Jenne, and D. Joseph, 1996: The NCEP/NCAR 40-Year Reanalysis Project. *Bull. Amer. Meteor. Soc.*, 77, 437-471.
- Karl, T.R., S.J. Hassol, C.D. Miller, and W.L. Murray (eds.), 2006: Temperature Trends in the Lower Atmosphere: Steps for Understanding and Reconciling Differences. A

report by the Climate Change Science Program and Subcommittee on Global Change Research, Washington, DC.

Kiehl, J. T. and V. Ramanathan, 1982: Radiative Heating Due to Increased CO₂: The Role of H₂O Continuum Absorption in the 12-18 mm Region. *J. Atmos. Sci.*, 39, 2923-2926.

Kiehl, J.T., and K.E. Trenberth, 1997: Earth's Annual Global Mean Energy Budget. *Bull. Amer. Meteor. Soc.*, 78, 197–208.

Knutson, T.R., T.L. Delworth, K.W. Dixon, I.M. Held, J. Lu, V. Ramaswamy, M.D. Schwarzkopf. 2006: Assessment of twentieth-century regional surface temperature trends using the GFDL CM2 coupled models. *J. Climate*, 19, 1624-1651.

Lemke, P., J. Ren, R.B. Alley, I. Allison, J. Carrasco, G. Flato, Y. Fujii, G. Kaser, P. Mote, R.H. Thomas and T. Zhang, 2007: Observations: Changes in Snow, Ice and Frozen Ground. In: *Climate Change 2007: The Physical Science Basis. Contribution of Working Group I to the Fourth Assessment Report of the Intergovernmental Panel on Climate Change* [Solomon, S., D. Qin, M. Manning, Z. Chen, M. Marquis, K.B. Averyt, M. Tignor and H.L. Miller (eds.)]. Cambridge University Press, Cambridge, United Kingdom and New York, NY, USA.

Lu, J-H., M. Cai, 2008: A new framework for isolating individual feedback processes in coupled general circulation climate models. Part I: Formuation. *Clim. Dyn.*, Doi: 10.1007/s00382-008-0425-3.

Lu, J-H., M. Cai, 2009: Quantifying contributions to polar warming amplification in a coupled general circulation model.

Manabe S., R. J. Stouffer, 1980: Sensitivity of a global climate model to an increase of CO₂ concentration in the atmosphere. *J. Geophys. Res.*, 85: 5529-5554.

Meehl, G.A., T.F. Stocker, W.D. Collins, P. Friedlingstein, A.T. Gaye, J.M. Gregory, A. Kitoh, R. Knutti, J.M. Murphy, A. Noda, S.C.B. Raper, I.G. Watterson, A.J. Weaver and Z.-C. Zhao, 2007: Global Climate Projections. In: *Climate Change 2007: The Physical Science Basis. Contribution of Working Group I to the Fourth Assessment Report of the Intergovernmental Panel on Climate Change* [Solomon, S., D. Qin, M. Manning, Z. Chen, M. Marquis, K.B. Averyt, M. Tignor and H.L. Miller (eds.)]. Cambridge University Press, Cambridge, United Kingdom and New York, NY, USA.

Moritz, R.E., C.M. Bitz, E. J. Steig, 2002: Dynamics of recent climate change in the Arctic. *Science*, 297, 1497-1502.

Murphy, J. M., D. M. H. Sexton, D. N. Barnett, G. S. Jones, M. J. Webb, M. Collins, D. A. Stainforth, 2004: Quantification of modeling uncertainties in a large ensemble of climate change simulations. *Nature*, 430, 768-772

- National Research Council. 2000: Reconciling observations of global temperature change. Washington, D.C.: National Academies Press.
- National Research Council. 2003: Estimating Climate Sensitivity: Report of a workshop. Washington, D.C.: National Academies Press.
- National Research Council. 2003: Understanding Climate Change Feedbacks. Washington, D.C.: National Academies Press.
- National Research Council. 2008: Understanding and responding to climate change. Highlights of National Academies Reports. Washington, D.C.: National Academies Press.
- Peixoto, J.P., A.H., Oort, 1992: Physics of climate. American Institute of Physics.
- Peterson, B., R. M. Holmes, J. W. McClelland, C. J. Vorosmarty, R. B. Lammers, A. I. Shiklomanov, I. A. Shiklomanov, S. Rahmstorf, 2002: Increasing river discharge to the Arctic Ocean. *Science*, vol. 298, 2171-2173.
- Petty, G. W., 2006: A first course in atmospheric radiation, second edition. Sundog Publishing. pp238-258.
- Pincus, R., C. P. Batstone, R. J. P. Hofmann, K. E. Taylor, and P. J. Glecker, 2008: Evaluating the present-day simulation of clouds, precipitation, and radiation in climate models. *J. Geophys. Res.*, 113, D14209, doi:10.1029/2007JD009334.
- Qu, X., A., Hall, 2005: Surface contribution to planetary albedo variability in cryosphere regions. *J. Clim.*, 18, 5239-5252
- Ramanathan, V., et al., 1989: Cloud-Radiative Forcing and Climate: Results from the Earth Radiation Budget Experiment. *Science*, Vol. 243. no. 4887, pp. 57 – 63.
- Ramaswamy, V., et al., 2001: Radiative forcing of climate change. In: Climate change 2001: The Scientific Basis. Contribution of working group I to the Third Assessment Report of the Intergovernmental Panel on Climate Change [Houghton, J.T., et al., (eds.)]. Cambridge University Press, Cambridge, United Kingdom and New York, NY, USA, pp. 349-416.
- Randall, D. A., et al., 1994: Analysis of Snow Feedbacks In Fourteen General Circulation Models. *J. Geophys. Res.*, 99, 20,757-20,771
- Randall, D.A., R.A. Wood, S. Bony, R. Colman, T. Fichefet, J. Fyfe, V. Kattsov, A. Pitman, J. Shukla, J. Srinivasan, R.J. Stouffer, A. Sumi and K.E. Taylor, 2007: Climate Models and Their Evaluation. In: Climate Change 2007: The Physical Science Basis. Contribution of Working Group I to the Fourth Assessment Report of the Intergovernmental Panel on Climate Change [Solomon, S., D. Qin, M. Manning, Z.

Chen, M. Marquis, K.B. Averyt, M.Tignor and H.L. Miller (eds.)]. Cambridge University Press, Cambridge, United Kingdom and New York, NY, USA.

Rigor, I.G., R.L. Colony, S. Martin, 2000: Variations in surface air temperature observations in the Arctic, 1797-97. *J. Climate*, 13, 896-914.

Schneider, E.K., B.P. Kirtman and R.S. Lindzen, 1999: Tropospheric water vapor and climate sensitivity. *J. Atm. Sci.*, 36, 1649-1658.

Schweiger A. J., R. W. Lindsay, S. Varus, J. A. Francis, 2008: Relationships between Arctic sea ice and clouds during Autumn. *J. Clim.*, 21, 4799- 4810.

Sellers, W. D., 1969: A climate model based on the energy balance of the earth-atmosphere system. *J. Appl. Meteor.*, 8, 392-400.

Serreze, M. C., Walsh, J. E., Chapin, F. S., Osterkamp, T., Dyurgerov, M. et al., 2000: Observational evidence of recent change in the northern high-latitude environment. *Clim. Change*, 46, 159–207.

Serreze, M., and J.A. Francis, 2006: The Arctic amplification debate. *Clim. Change*, 76, 241–264.

Shell, K. M., et al., 2008: Using the Radiative Kernel Technique to Calculate Climate Feedbacks in NCAR's Community Atmospheric Model. *J.Climate*, 21, 2269–2282.

Soden, B. J., R. T. Wetherald, G. L. Stenchikov, and A. Robock, 2002: Global cooling after the eruption of Mount Pinatubo: a test of climate feedback by water vapor. *Science*, 296, 727–730.

Soden, B., A.J. Broccoli, R.S. Hemler, 2004: On the use of cloud forcing to estimate cloud feedback. *J. Climate*, 17, 3661-3665.

Soden, B., and I.M. Held, 2006: An assessment of climate feedbacks in coupled ocean-atmosphere models. *J. Climate*, 19, 3354-3360.

Soden, B.J., et al., 2008: Quantifying climate feedbacks using radiative kernels. *J. Climate*, 21, 3504-3520.

Stainforth, D. A., T. Aina, C. Christensen, M. Collins, N. Faull, D. J. Frame, J. A. Kettleborough, S. Knight, A. Martin, J. M. Murphy, C. Piani, D. Sexton, L. A. Smith, R. A. Spicer, A. J. Thorpe, M. R. Allen, 2005: Uncertainty in predictions of the climate response to rising levels of greenhouse gases. *Nature*, 433, 403-406

Stephens, G.L., 2005: Cloud feedbacks in the climate system: a critical review. *J. Clim.*, 18, 237-273.

Stouffer R. J., A. J. Broccoli, T. L. Delworth, K. W. Dixon, R. Gudgel, I. Held, R. Hemler, T. Knutson, H-C. Lee, M. D. Schwarzkopf, B. Soden, M. J. Spelman, M. Winton, F. Zeng. 2006: GFDL's CM2 Global coupled climate models. Part IV: Idealized climate response. *J. Clim. Spec. Sec.*, 19, 723-740.

Trenberth, K. E., and C. J. Guillemot, 1998: Evaluation of the atmospheric moisture and hydrological cycle in the NCEP/NCAR reanalyses. *Climate Dyn.*, 14, 213-231.

Trenberth, K.E., P.D. Jones, P. Ambenje, R. Bojariu, D. Easterling, A. Klein Tank, D. Parker, F. Rahimzadeh, J.A. Renwick, M. Rusticucci, B. Soden and P. Zhai, 2007: Observations: Surface and Atmospheric Climate Change. In: *Climate Change 2007: The Physical Science Basis. Contribution of Working Group I to the Fourth Assessment Report of the Intergovernmental Panel on Climate Change* [Solomon, S., D. Qin, M. Manning, Z. Chen, M. Marquis, K.B. Averyt, M. Tignor and H.L. Miller (eds.)]. Cambridge University Press, Cambridge, United Kingdom and New York, NY, USA.

Weaver, C. P., 2003: Efficiency of storm tracks an important climate parameter? The role of cloud radiative forcing in poleward heat transport, *J. Geophys. Res.*, 108(D1), 4018, doi:10.1029/2002JD002756

Webb, et al., 2006: On the contribution of local feedback mechanisms to the range in climate sensitivity in two GCM ensembles. *Clim. Dyn.* 27, 17-38.

Wetherald, R. T., and S. Manabe, 1988: Cloud feedback processes in a general circulation model. *J. Atmos. Sci.*, 45, 1397-1415.

Wild, M., C. N. Long, and A. Ohmura, 2006: Evaluation of clear-sky solar fluxes in GCMs participating in AMIP and IPCC-AR4 from a surface perspective. *J. Geophys. Res.*, 111, D01104, doi:10.1029/2005JD006118.

Wild, M., and E. Roeckner, 2006: Radiative Fluxes in the ECHAM5 General Circulation Model. *J. Climate*, 19, 3792–3809.

Winton, M., 2006: Amplified climate change: what does surface albedo feedback have to do with it? *Geophys. Res. Lett.*, 33, L03701, doi: 10.1029/2005GL025244.

Winton, M., 2006: Surface albedo feedback estimates for the AR4 climate models. *J. Climate*, 19, 359-365.

Zhang, M., 2004: Cloud-climate feedback: How much do we know? In "Observation, Theory, and Modeling of Atmospheric Variability", edited by Zhu et al., World Scientific Series on Meteorology of East Asia, Vol. 3, World Scientific Publishing Co., Singapore, 2004, 632pp

BIOGRAPHICAL SKETCH

Christelle was born on August 14th 1981 in Toulouse, France. After graduating high school in 1999 she moved to Sophia Antipolis, France to pursue her studies in Environmental Science at the CERAM for two years. She then chose Florida Institute of Technology to complete her undergraduate education. She graduated with honor from a Bachelor of Science in Meteorology in May of 2003. She was then accepted at Florida State University to pursue a Master degree in Meteorology. During her first year she was a teaching assistant and she then started working with her advisor Dr Cai on the dynamical amplification of high latitudes warming and became very passionate about climate change research. She received her Master degree in August 2005. She was also actively involved with both the Graduate Women In Science and International Student organizations at Florida State University that she cofounded in 2006. She focused her research on climate feedback analysis using IPCC climate change simulations, and successfully defended her dissertation in summer of 2009. She will continue her research on climate feedbacks at the Laboratoire de Météorologie Dynamique.